

DIFFRACTIVE D*-MESONS
PRODUCTION IN DIS
AT HERA

Dissertation

zur Erlangung des Doktorgrades
des Fachbereichs Physik
der Universität Hamburg

vorgelegt von

SVETLANA VINOKUROVA

aus Sergiev Posad (Zagorsk),
Rußland

Hamburg
2007

Abstract

This thesis presents a measurement of the cross sections for the production of the charmed mesons in diffractive deep inelastic positron-proton scattering (DIS) interactions of the type $ep \rightarrow eXY$, where the system X is separated from a low-mass system Y, by a large rapidity gap where no particles are observed. These diffractive processes can be explained as a result of the exchange of a strongly interacting colour singlet object between the final state particles.

In this measurement data taken with the H1 detector in the years 1999-2000, corresponding to an integrated luminosity of $\mathcal{L}_{int} = 46.7 \text{ pb}^{-1}$ are used.

Inclusive DIS events are selected in the kinematic range with the momentum transfer $Q^2 \in [2;100] \text{ GeV}$ and inelasticity $y_{bj} \in [0.05;0.7]$. The charm quark is tagged by requiring a D^* meson decaying into the channel $D^* \rightarrow D^0\pi_{slow} \rightarrow K\pi\pi_{slow}$ inside the central tracking system with transverse momenta $p_t(D^*) > 2 \text{ GeV}$.

The forward components of the H1 detector are used to select genuine diffractive events on the basis of the forward sub-detectors activity and of the presence a large rapidity gap in the final state hadrons.

The visible charm production cross sections are measured in the diffractive kinematic range $M_Y < 1.6 \text{ GeV}$, $|t| < 1 \text{ GeV}^2$ and $x_P < 0.04$ to be

$$\sigma(ep \rightarrow e'(D^*X)Y) = 249 \pm 31(stat.) \pm 30(sys) \text{ pb},$$

where the first uncertainty is statistical and the second systematic.

The shape of the differential distributions for diffractive D^* production are well described by the collinear factorisation model which is implemented in the Monte Carlo simulation RAPGAP.

Zusammenfassung

Die vorliegende Arbeit beschreibt eine Messung des Wirkungsquerschnitts für die Produktion von Charm-Mesonen in diffraktiver tief-inelastischer Positron-Proton Streuung für Ereignisse des Typs $ep \rightarrow eXY$, wobei das System X durch eine große Rapiditätslücke von dem System kleiner Masse Y getrennt ist. Diese diffraktiven Prozesse können als Ergebnis eines Austausches eines stark wechselwirkenden farb neutralen Objektes erklärt werden.

In der Arbeit werden Daten benutzt, die 1999-2000 mit dem H1 Detektor aufgezeichnet wurden und einer integrierten Luminosität von $\mathcal{L}_{int} = 46.7 \text{ pb}^{-1}$ entsprechen. Inklusive tiefinelastische Ereignisse sind in einem kinematischen Bereich selektiert, der durch die DIS-Variablen $Q^2 \in [2;100] \text{ GeV}$ und $y_{bj} \in [0.05;0.7]$ definiert ist. Der Nachweis von Charm-Quarks erfolgt durch die Rekonstruktion von D^* -Mesonen im so genannten goldenen Zerfallskanal $D^* \rightarrow D^0 \pi_{slow} \rightarrow K \pi \pi_{slow}$ im zentralen Spurkammersystem mit einem Transversalimpuls von $p_t(D^*) > 2 \text{ GeV}$. Um diffraktive Ereignisse zu selektieren, werden Vorwärtskomponenten des H1-Detektors verwendet.

Der sichtbare Produktions-Wirkungsquerschnitt wurde im diffraktiven kinematischen Bereich $M_Y < 1.6 \text{ GeV}$, $|t| < 1 \text{ GeV}^2$ und $x_P < 0.04$

$$\sigma(ep \rightarrow e'(D^*X)Y) = 249 \pm 31(stat.) \pm 30(sys) \text{ pb},$$

gemessen, wobei die erste Unsicherheit statistisch und die zweite systematisch ist.

Contents

1	Introduction	1
2	Theoretical Overview	3
2.1	Deep Inelastic ep -Scattering	3
2.2	The Structure of the Proton	5
2.3	Scaling Violation and Quantum Chromodynamics	7
2.4	Charm Production	9
2.5	Diffraction in Soft Hadron Interactions	11
2.6	Diffraction Deep Inelastic ep -Scattering	12
2.7	QCD Hard Scattering Factorisation for Diffractive DIS	15
2.8	Regge Factorisation Approach	15
2.9	Diffractive Charm Production	16
2.9.1	Factorisable Pomeron Approach	16
2.9.2	Perturbative Two-Gluon Exchange Model	16
2.9.3	Soft Colour Interactions	18
2.10	Monte Carlo Generators	20
3	The H1 Experiment at HERA	21
3.1	The HERA Collider	21
3.2	Overview of the H1 Detector	23
3.3	The Tracking System	23
3.4	Calorimetry in the H1 Detector	24
3.5	Forward Detectors	27
3.6	The Time-of-Flight System and Luminosity Measurement	29
3.7	The Trigger System	29
4	RAPGAP Monte Carlo Samples	32
4.1	Monte Carlo Generator RAPGAP	32
4.2	RAPGAP for Elastic Diffractive DIS	32
4.3	RAPGAP for Diffractive Proton Dissociation	33
4.4	RAPGAP for Inclusive DIS	34
5	Data Selection	37
5.1	Run Selection	37
5.1.1	The Analysis Subtrigger	37
5.2	Selection of Deep Inelastic Scattering Events	38
5.2.1	Kinematic Reconstruction of the DIS Variables	40

5.3	Selection of D^* events	41
5.3.1	Reconstruction of the D^* Mesons	41
5.3.2	D^* Meson Selection	42
5.3.3	D^* Meson Fit Method	43
6	Selection of Diffractive Events	44
6.1	Selection of Diffractive Events using Forward Detectors	44
6.1.1	Noise Treatment in the Monte Carlo Simulations	47
6.2	Energy Flow in the Liquid Argon Calorimeter	52
6.3	The Plug Calorimeter	52
6.4	The Forward Muon Detector	53
6.5	The Proton Remnant Tagger	56
6.6	Reconstruction of the Kinematic Variables	60
6.7	Summary of the Selection of Diffractive D^* Mesons	62
7	Cross Section Measurement	66
7.1	Determination of the Cross Section	66
7.1.1	Trigger Efficiency	67
7.1.2	Geometric Acceptance and Efficiency of Detectors	68
7.2	Inclusive D^* Measurements	69
7.3	Diffractive Measurements	72
7.3.1	Correction for proton-dissociative events	72
7.3.2	Uncertainty of the Cross Section	73
7.3.3	Diffractive D^* Cross Section	75
7.4	Data Comparison with Theory	81
8	Summary and Outlook	87
	Appendices	89
A	Detailed Run Selection	89
B	Algorithm for the "Probability" Method	91
C	Δ M Signals for the Differential Distributions	93
D	Unintegrated Gluon Densities	112
	Bibliography	119

Chapter 1

Introduction

Throughout the history of Particle Physics, scattering experiments have played a crucial role in the development of our understanding of the fundamental structure of matter and the forces of nature. The nucleus was discovered by Rutherford's scattering experiment, later scattering experiments led to the observation of proton constituents within the nucleus. The observation of partons within the proton was made by the scattering of leptons in various fixed target experiments. The HERA collider has made possible the study of electron-proton collisions at a centre-of-mass energy of 300 GeV, which is roughly an order of magnitude higher than at fixed target experiments.

Particle Physics studies elementary particles and interactions between them. Within the Standard Model the proton consists of point-like spin-half quarks, that interact with one and another via the strong force. The strong force is mediated by the exchange of massless vector bosons, so-called gluons and is described by the theory of Quantum Chromodynamics (QCD). The value of the coupling constant of QCD, α_s , depends on the energy scale of the interaction. It rises at small energy or, equivalently, at large distance scales. This property of the coupling constant explains the confinement of quarks into colourless hadrons. Perturbative calculations in QCD require the presence of a large scale, e.g. a large virtuality Q^2 , a large transverse momentum p_t or large particle masses m . The mass of the charm quark, $m_c \approx 1.5$, is large enough to provide a hard scale. Due to this fact, the study of the heavy quark production is used for testing the perturbative QCD mechanism.

One of the surprising results of HERA was the observation of a class of DIS events in which a rapidity gap is adjacent to the proton direction in which no hadrons emerge. These events must be due to colour singlet exchange and they are found to contribute significantly to high energy interactions. Such a process has been interpreted as a *diffractive* process with a colourless object, *the pomeron*, which carries vacuum quantum numbers. Diffractive reactions were studied intensively in the sixties and seventies and were described phenomenologically before the advent of the QCD. Nowadays these events provide an interesting area to use perturbative QCD to understand the diffractive phenomena and the pomeron.

This thesis is organised as follows: The second chapter is devoted to the theoretical basis of the analysis. The physics of the deep inelastic scattering is introduced which is needed further in order to understand how the process of diffractive DIS may be interpreted within QCD. The diffractive scattering is discussed. The third chapter gives an

overview of the HERA accelerator and the H1 detector, and then details the components of the H1 detector which are important for the analysis. In the fourth chapter different types of the RAPGAP Monte Carlo simulation program are discussed and an algorithm of event simulation for the purpose of this analysis is explained. Chapter five deals with the inclusive event selection. In this section requirements for the positron candidate are listed, furthermore the selection and fit procedures for the $D^* \rightarrow D^0 \pi_{slow} \rightarrow K \pi \pi_{slow}$ are described. The selection of the diffractive DIS events, using the forward components of the H1 detector is described in detail in the sixth chapter. The seventh chapter presents correction procedures used to determine the cross section measurements. In this chapter the efficiency studies, systematic errors and measured cross sections compared with theoretical predictions are discussed. In the last chapter the results of the analysis are summarised and an outlook is given.

Chapter 2

Theoretical Overview

In this chapter an introduction to the physics of Diffractive Deep Inelastic Scattering D^* -Meson production is given.

A brief review of the physics topics relevant at HERA with special emphasis on the Deep Inelastic Scattering (DIS) is presented. The basic ideas of using the theory of strong interactions, Quantum Chromodynamics (QCD), in the description of DIS processes are introduced. The charm production mechanism is outlined.

Next, the topic of diffraction is discussed and a summary of Regge theory is given. Finally, concepts of several theoretical models of diffraction are described.

2.1 Deep Inelastic ep -Scattering

The process of deep inelastic scattering of electrons off protons is classified as neutral (NC) or charge current (CC), depending on the exchange between the scattering lepton and the proton. In the NC interactions the positron scatters off the proton via the exchange of a neutral electroweak gauge boson (a photon or a Z^0 boson). In the case of the charged current DIS, the interaction proceeds via the exchange of a charged boson, W^\pm . Figure 2.1 shows an example of the NC process in the lowest order QED, including the four-vectors of the interacting particles. X represents the hadronic final state produced by the scattering process.

The kinematic properties of the process $e + p \rightarrow e' + X$ can be described by the quantities specified in the following. The square of the four-momentum transfer (Q^2), i.e. the virtuality of the exchanged boson, and the total center of mass energy (s) of the process are defined as

$$Q^2 \equiv -q^2 = -(k - k')^2, \quad (2.1)$$

$$s = (k + P)^2 \simeq 4E_e E_p, \quad (2.2)$$

where E_e and E_p are the energies of the colliding particles. In the last part of Equation 2.2 masses are neglected. For the beam energies used in this analysis we obtain $\sqrt{s} = 320$ GeV.

The regime $Q^2 > 1 \text{ GeV}^2$ is referred to as *deep inelastic scattering* (DIS). If the exchanged photon is almost real, $Q^2 \rightarrow 0$, the process is usually referred to as *photoproduction*.

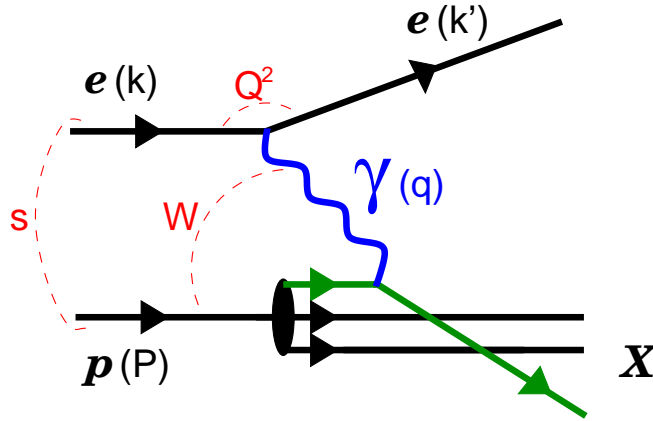


Figure 2.1: Diagram for inclusive deep inelastic scattering process. The four-vectors are shown for the incoming and outgoing positron (k , k'), the exchanged photon (q), the incoming proton (p).

The dimensionless Bjorken scaling variable

$$x = \frac{Q^2}{2P \cdot q} \quad (2.3)$$

can be interpreted as the fraction of the proton momentum carried by the struck quark in the infinite momentum frame of the proton. The second Bjorken scaling variable y is defined by

$$y = \frac{P \cdot q}{P \cdot k}, \quad (2.4)$$

which is the fraction of the electron energy taken by the exchanged photon in the proton rest frame.

The square of the mass of the photon-proton system, which is equivalent to the square of the invariant mass of the hadronic final state X , is defined as

$$W^2 = (q + P)^2. \quad (2.5)$$

Neglecting the positron and the proton rest masses, the quantities, defined in equations 2.1- 2.5, are related by two expressions

$$Q^2 = sxy, \quad (2.6)$$

$$W^2 = sy - Q^2. \quad (2.7)$$

At fixed s , only two of these five quantities are independent and allow to describe the kinematics of the inclusive scattering process.

In comparison to the photon exchange, the Z^0 and W^\pm exchange can be safely neglected (except at high $Q^2 > 1000 \text{ GeV}^2$) because of their large masses.

2.2 The Structure of the Proton

In this thesis only neutral current DIS processes with $Q^2 < 100 \text{ GeV}^2$ are studied. From this point of view the cross section, expressed in terms of the two variables x and Q^2 , can then be written as,

$$\frac{d^2\sigma(ep \rightarrow eX)}{dx dQ^2} = \frac{4\pi\alpha_{em}^2}{xQ^4} \cdot \left[y^2 x F_1(x, Q^2) + (1-y) \cdot F_2(x, Q^2) \right], \quad (2.8)$$

where $F_1(x, Q^2)$ and $F_2(x, Q^2)$ are structure functions which depend on the spatial distribution of charged objects within the proton. Because the cross section has two independent contributions, arising from transversely (σ_T) and longitudinally (σ_L) polarised photons, the longitudinal structure function $F_L(x, Q^2)$ is introduced. $F_2(x, Q^2)$ corresponds to the sum ($\sigma_T + \sigma_L$), whereas $F_L(x, Q^2)$ describes σ_L only. Equation 2.8 can then be rewritten in terms of the introduced structure function

$$\frac{d^2\sigma(ep \rightarrow eX)}{dx dQ^2} = \frac{4\pi\alpha_{em}^2}{xQ^4} \cdot \left[1 - y + \left(\frac{1}{1 + R(x, Q^2)} \right) \frac{y^2}{2} \right] \cdot F_2(x, Q^2), \quad (2.9)$$

where $R(x, Q^2)$ is the ratio of the longitudinal to transverse photon cross sections, which is given by

$$R(x, Q^2) = \frac{\sigma_L}{\sigma_T} = \frac{F_L(x, Q^2)}{F_2(x, Q^2) - F_L(x, Q^2)}. \quad (2.10)$$

The contributions from the longitudinal photon exchange can be neglected in the region of small y , thereby equation 2.9 reduces to

$$\frac{d^2\sigma(ep \rightarrow eX)}{dx dQ^2} = \frac{4\pi\alpha_{em}^2}{xQ^4} \cdot \left[1 - y + \frac{y^2}{2} \right] \cdot F_2(x, Q^2). \quad (2.11)$$

The structure functions cannot be fully calculated in perturbation theory and have to be partially determined from the experimental data.

The Quark Parton Model

The Quark Parton Model (QPM) was developed to explain the observation, that the structure function $F_2(x, Q^2)$ is approximately independent of Q^2 over a wide range of Q^2 values. In QPM, the proton is considered to be composed of free, point-like fermions, namely quarks, the momentum distributions of which are described by the parton density functions $f_i(x)$ (PDFs). The scattering takes place from point-like constituents in the proton, and therefore PDFs should depend only on the dimensionless variable x . If the DIS cross section is considered in terms of the PDFs, the following relationships can be defined:

$$F_1(x) = \frac{1}{2} \sum_i e_i^2 \cdot f_i(x), \quad (2.12)$$

$$F_2(x) = 2xF_1(x) \quad (2.13)$$

where e_i^2 is the charge of the quark of flavour i . The equation 2.13 is known as the Callan-Gross relation, and it follows from the spin-half nature of the quarks.

The universal property of PDFs, namely the independence of the hard scattering, allows PDFs to be constrained from the data in different experiments and combined to form global fits.

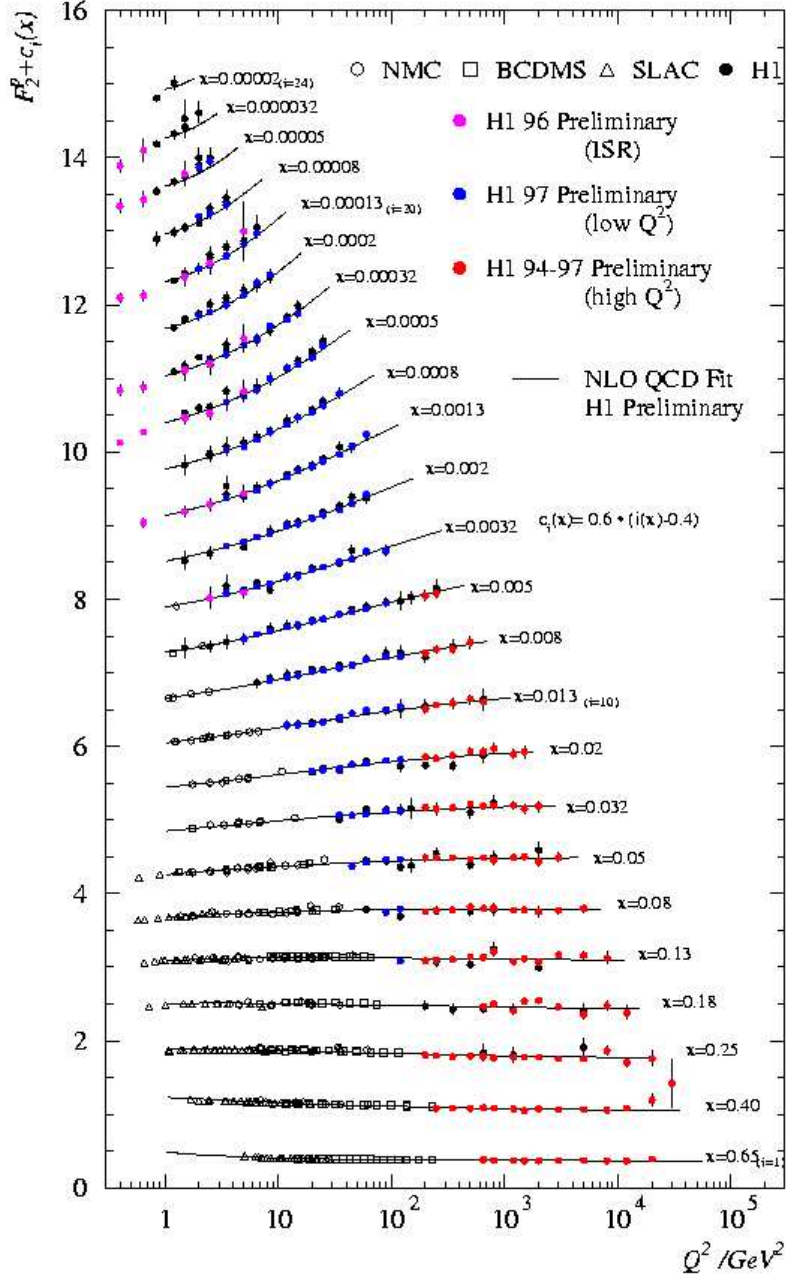


Figure 2.2: Measurements of the proton structure function $F_2(x, Q^2)$ in bins of x compared to a QCD fit using the DGLAP evolution formalism.

2.3 Scaling Violation and Quantum Chromodynamics

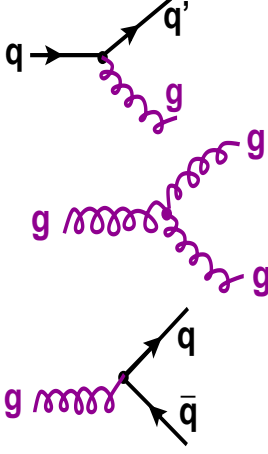


Figure 2.3: *Feynman diagram for the parton splitting processes.*

If the QPM describes correctly the structure of the proton, the sum of the momenta of the quarks and the anti-quarks have to be equal the momentum of the proton. This can be expressed by the sum rule:

$$\sum_i \int_0^1 x [q(x) + \bar{q}(x)] dx = 1. \quad (2.14)$$

However, a value of ~ 0.5 instead of 1 was obtained experimentally, implying that other objects carry a significant fraction of the proton momentum.

Furthermore, it is known that Bjorken scaling is only approximate, there are systematic scaling violations (see Figure 2.2), particularly at low x , where a clear Q^2 dependence is visible.

These violations can be explained in terms of Quantum Chromodynamics (QCD), the theory of the strong interactions. In QCD, the quarks in the proton interact via the exchange of massless bosons, called *gluons*. Quarks have an additional degree of freedom, *colour* (red, green or blue). Colour is exchanged by eight gluons, which carry different combinations of colour charge. In the region of high Q^2 , the exchanged boson probes the proton with increasing spatial resolution. Interacting within the proton, the quarks can radiate gluons ($q \rightarrow q'g$), the gluons themselves can radiate further gluons ($g \rightarrow gg$) or split into quark-antiquark pairs ($g \rightarrow q\bar{q}$). These processes are illustrated in figure 2.3. In this scheme, high momentum quarks lose momentum through such splitting processes.

With increasing Q^2 , the probability of sampling a quark at lower x increases. Thus, at high x , $F_2(x, Q^2)$ decreases with increasing of Q^2 and $F_2(x, Q^2)$ increases correspondingly at low x .

Renormalisation

In order to calculate QCD cross sections, integrations over the real and virtual quarks and gluons have to be done. These integrals are related to divergent integrals. An appropriate regularisation scheme is used to remove the divergent parts of the integrals. This leads to a dependence of the calculated cross sections on the energy scale μ_r^2 used in the regularisation. The regularisation process is reflected in the dependence of the coupling constant α_s on the *renormalisation scale* μ_r^2 .

The term *asymptotic freedom* refers to the concept that quarks become more and more independent of their hadronic environment when the coupling constant is very small, i.e. when Q^2 increases and the time scale becomes shorter. *Asymptotic freedom* and *confinement* (the coupling strength gets larger when Q^2 decreases and quarks are confined strongly in hadrons) are known as consequences of the dependence of the coupling constant on the renormalisation scale.

Factorisation

The QCD hard scattering factorisation theorem allows to separate the short-distance aspects of a physical process, which are calculable, to a particular order in α_s , and measurable, from the universal (partially not calculable) long-distance aspects, so that the structure function $F_2(x, Q^2)$ can be expressed as a convolution of a coefficient function C_i , calculable in perturbative QCD, and the parton distribution function f_i of the proton, with i responsible for the parton flavour.

$$F_2(x, Q^2) = \sum_{i=q,\bar{q},g} \int_x^1 d\xi f_i(d\xi, \mu_r^2, \mu_f^2, \alpha_s) \cdot C_i\left(\frac{x}{\xi}, \frac{Q^2}{\mu_r^2}, \mu_f^2, \alpha_s\right), \quad (2.15)$$

where μ_f^2 is the *factorisation* scale, which defines the energy scale above which the process is calculable within perturbative QCD.

In the region of DIS measurements ($Q^2 > 1 \text{ GeV}^2$) the coupling strength is sufficiently small, such that perturbative QCD (pQCD) may be applied. Within pQCD it is not possible to calculate the parton densities, however it is possible to predict the evolution of the parton distributions (for example as a function of $\ln(Q^2)$) using perturbative calculations.

There are different approaches for the evaluation of the parton density functions, some of them are briefly described in the following.

DGLAP

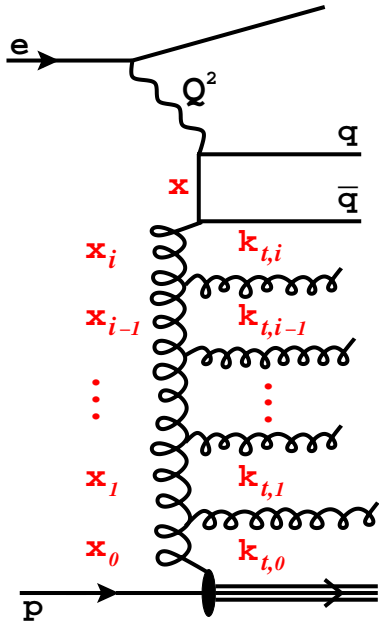


Figure 2.4: *General gluon ladder.*

In the DGLAP¹ approach [1–4], the evolution of parton densities is performed in k_t (the transverse momentum of the emitted gluons). The parton density functions are separated into parts representing the valence quark (flavour non-singlet), sea quark (flavour singlet) and gluon contribution. These functions are determined from existing data at a reasonable starting scale, where a perturbative approach is valid. The evolution proceeds through the splitting processes illustrated in the Figure 2.3. The evolution of proton distributions can be visualised by a *ladder diagram* of parton emissions as shown in the Figure 2.4.

The main approximation is that the transverse momenta $k_{t,i}$ during consecutive gluon radiation are strongly ordered, i.e. $k_{t,i}^2 \ll k_{t,i+1}^2 \ll \dots \ll Q^2$, furthermore ordering of longitudinal momenta is required $x_i > x_{i+1} > \dots > x$.

Factorisation within these approximations is called *collinear factorisation*.

¹The evolution equations of Dokshitzer, Gribov, Lipatov, Altarelli, Parisi.

BFKL

The kinematic region which can be accessed at HERA extends to very low x values. In the region of low x , the BFKL² approximation [5–7] is appropriate. In this regime the assumption is, that the momentum fraction z carried by the parton after the emission is very small, the leading contribution is the $\frac{1}{z}$ term. In the BFKL approximation no ordering of transverse momenta $k_{t,i}$ is needed, however longitudinal momenta have to be strongly ordered $x_i \ll x_{i+1} \ll \dots \ll x$.

This approximation is applicable in the small x region, and therefore only gluons have to be taken into account. The relevant proton momentum fraction x_g corresponds then to the x_i in the Figure 2.4. The gluon density function $\mathcal{F}(x_g, k_t^2)$ in this approach depends on k_t . The factorisation theorem is more complicated and is called k_t – factorisation.

CCFM

The CCFM³ formalism [8–11] was developed by a group of Italian theorists, and in this model both approaches, described above, are unified, aiming for good approximations at small and large x .

The gluon ladder is not ordered in k_t or z , instead of this an angular ordering of the emitted gluons is performed. In the CCFM formalism only gluons are considered in the parton evolution, which corresponds to the BFKL model. Furthermore in this approach the gluon density function $\mathcal{A}(x_g, k_t^2, \mu_f^2)$ depends on x_g , k_t and on the factorisation scale μ_f^2 . The latter dependence defines the maximum allowed angle for any emission. The gluon density in this approach is called *unintegrated gluon density*. CCFM also leads to the k_t -factorised cross section.

The Figure 2.5 presents the CCFM gluon ladder, with the momentum fractions x_i , the virtualities $k_{t,i}^2$ and the emission angles of the gluons θ_i .

All these approaches provide a good description of the structure function F_2 at small x . The DGLAP approach is most commonly used for the parton evolution description, however, for example, in forward jets analyses, the application of BFKL or CCFM formalisms are favoured.

2.4 Charm Production

Charm production at HERA in the final state of a DIS event can be described in different ways:

- The charm quarks may have been generated dynamically via boson-gluon fusion. This production mechanism is referred to as *extrinsic charm* production (*massive approach*).

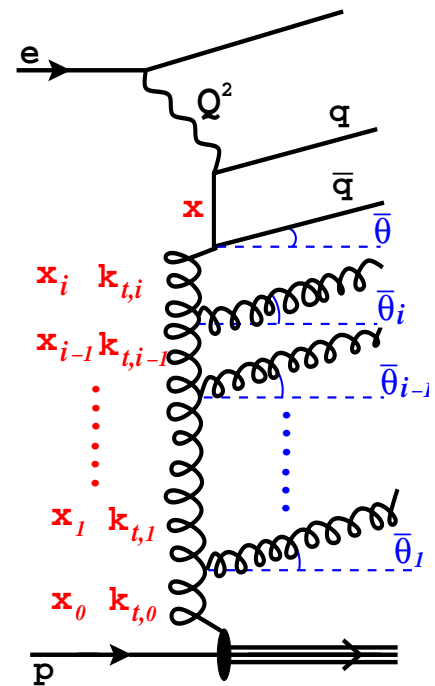


Figure 2.5: The CCFM gluon ladder.

²The evolution equation was developed by Balitsky, Fadin, Kuraev and Lipatov.

³Catani-Ciafaloni-Fiorani-Marchesini equation.

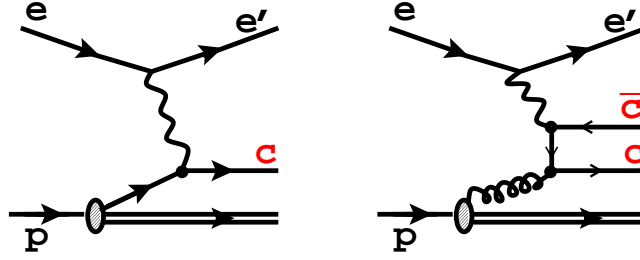


Figure 2.6: *Feynman diagrams for the charm production : (a) via the photon coupling to a charm quark in the sea of the proton; (b) via the boson-gluon fusion process.*

- At high Q^2 charm production can be described by the coupling of the photon to a charm quark in the sea of the proton, so called *intrinsic charm* production. In this *massless* approach the charm masses are neglected.

Leading order diagrams for both processes are sketched in the Figure 2.6. In the relevant measurements published by H1 it is shown, that less than 5 % (at 95 % confidential level) of the total charm production is contributed by the extrinsic charm. In this analysis charm is measured in the kinematical range $2 < Q^2 < 100 \text{ GeV}^2$, and therefore only the contribution of Boson-Gluon Fusion (BGF) is considered.

The rate of the charm quark production by the BGF process is sensible to the gluon content of the proton. Therefore an extraction of the gluon density can be made by the measurement of the charm yield, which is complementary to the inclusive ep measurements.

Fragmentation of the charm quarks

During the *fragmentation* process coloured partons are transferred to the colour neutral hadrons. This process may be subdivided in two parts. In the first, *fragmentation* part, outgoing partons radiate until their virtuality becomes small, - this step is calculable in perturbative QCD. The second part, *hadronisation*, describes the transition of the partons to the hadrons, and this process has to be described by phenomenological models. Two phenomenological models are briefly described below, the *Lund String Model* [12] and *Peterson fragmentation* [13].

In the sophisticated Lund String Model, the colour strings connected quarks and antiquarks move apart from each other, and if the energy stored in the string becomes large enough, the colour field breaks up and produces a quark-antiquark pair. The Figure 2.7 shows graphically the principle of the Lund String Model.

In the Peterson model, which is more simple, the momenta of the final state mesons are obtained as a convolution of the charm quark distributions with the Peterson fragmentation function, defined through

$$D(z) = N \cdot \left[z \left(1 - \frac{1}{z} - \frac{\epsilon_c}{1-z} \right)^2 \right]^{-1}, \quad (2.16)$$

where z denotes the fraction of the charm quark momentum carried by the charmed

hadron, ϵ_c is a parameter which relates the masses of the heavy quark and the light anti-quark picked up from the vacuum by the c quark.

2.5 Diffraction in Soft Hadron Interactions

Soft hadronic interactions are usually understood as interactions of hadrons at relatively small transverse momentum scales, where the transverse momentum p_t refers to the particles involved in the scattering process. The low momentum transfer implies that perturbative QCD is not applicable. The best description of these interactions is given by the phenomenological model of Regge theory [14–16], where interactions are described in terms of the exchange of so called Regge trajectories. Regge trajectories are presented by approximately straight lines, on which exchanged particles are situated if their angular momentum is plotted versus their mass squared (Chew-Frautschi plot).

Regge Theory

Regge theory⁴ was developed before QCD and it was based on very general assumptions about the scattering process. The total cross section for the scattering of two hadrons A and B is obtained by a sum over Regge trajectories $\alpha_i(t)$, which in a simple linear approximation are parametrised as

$$\alpha_i(t) = \alpha_i(0) + \alpha'_i \cdot t, \quad (2.17)$$

where $\alpha_i(0)$ denotes the intercept and α'_i the slope of the trajectory. The total cross section of hadron-hadron scattering can be effectively described by two types of trajectories, the Pomeron and Reggeon trajectories, $\alpha_P(t)$ and $\alpha_R(t)$ respectively. The total cross section is then expressed as

$$\sigma_{tot}(s) = \mathcal{A}_P s^{\alpha_P(0)-1} + \mathcal{A}_R s^{\alpha_R(0)-1}, \quad (2.18)$$

where \mathcal{A}_P , \mathcal{A}_R are normalisation factors. The second part of the equation 2.18 is due to the Reggeon trajectory and it is relevant at low energies. Whereas the first contribution is

⁴After the Italian physicist Tullio Regge.

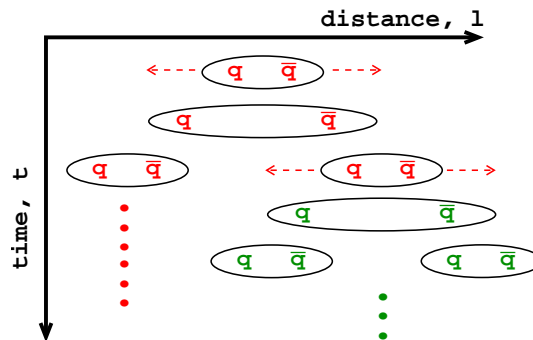


Figure 2.7: The basic idea of the Lund String Model is shown schematically.

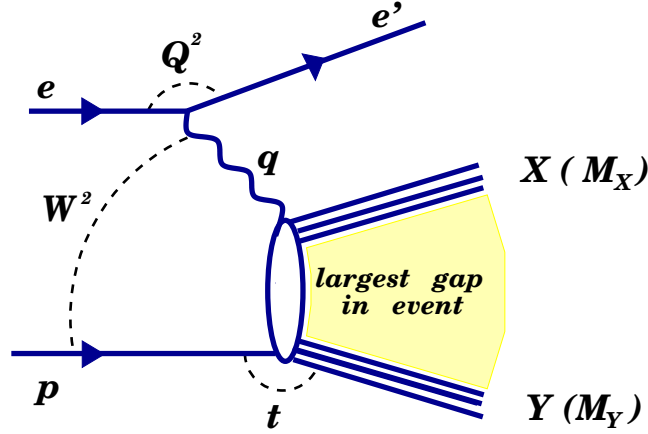


Figure 2.8: The diagram shows the inclusive deep inelastic diffractive scattering process. The four-vectors are shown for the system X (M_X), the system Y (M_Y), the exchanged photon (q), the incoming proton (p) and the squared four-momentum transfer at the proton vertex (t).

dominant at higher energies and it is called Pomeron trajectory. The intercepts α_P , α_R were found to be

$$\alpha_P(0) = 1.08 \quad (2.19)$$

$$\alpha_R(0) = 0.55 \quad (2.20)$$

The observed particles, such as ρ , ω , ϕ , are related to the reggeon trajectory. The processes that involve the pomeron exchange are known as *diffractive*. In these reactions no quantum numbers are exchanged and no physical particle has been observed which corresponds to the pomeron trajectory. Therefore, there is considerable motivation to understand the pomeron in the framework of QCD by investigating its partonic structure.

2.6 Diffractive Deep Inelastic ep -Scattering

Diffractive interactions characterized by a large rapidity gap in the hadronic final state, have been observed and studied in detail at HERA. This class of DIS events can be interpreted as being due to the colourless pomeron exchange between the virtual photon and the proton. For the DIS processes at HERA these events constitute approximately 10% of the cross section.

The Figure 2.8 represents schematically a diagram of these processes. Two systems X and Y are separated by the largest interval in the rapidity without any colour flow between them. If the proton remains intact, the process is called elastic with $M_Y = m_p$. The outgoing proton may also dissociate diffractively into a low-mass state system Y , so that $M_Y > m_p$.

The diffractive processes may be described as the interaction of the virtual photon with a colourless component of the proton, a *pomeron* (P).

In addition to the kinematic variables, which are used for description of DIS, additional

invariants are defined (in terms of the 4-vectors defined in Figure 2.8)

$$M_Y^2 = Y \cdot Y \quad (2.21)$$

$$M_X^2 = X \cdot X \quad (2.22)$$

$$t = (p - Y)^2 \quad (2.23)$$

$$x_{\mathcal{P}} = \frac{q \cdot (p - Y)}{q \cdot Y} \quad (2.24)$$

$$\beta = \frac{Q^2}{2q \cdot (p - Y)} \quad (2.25)$$

$$x = x_{\mathcal{P}} \cdot \beta, \quad (2.26)$$

where M_X and M_Y are the invariant masses of the hadronic systems X and Y , and t is the momentum transfer at the proton vertex. W is the mass of the photon-proton system. The variable $x_{\mathcal{P}}$ is the fraction of the incoming proton momentum carried by the diffractive exchange. Diffractive events are characterised by small values of $x_{\mathcal{P}}$, ($x_{\mathcal{P}} < 0.1$). The quantity β is the longitudinal momentum fraction of the exchange that is carried by a struck constituent of the exchange. $x_{\mathcal{P}}$ and β can be expressed in terms of the other invariants as:

$$x_{\mathcal{P}} = \frac{(Q^2 + M_X^2 - t^2)}{(Q^2 + W^2 - m_p^2)} \sim \frac{(Q^2 + M_X^2)}{(Q^2 + W^2)}, \quad (2.27)$$

$$\beta = \frac{Q^2}{(Q^2 + M_X^2 - t^2)} \sim \frac{Q^2}{(Q^2 + M_X^2)}. \quad (2.28)$$

The proton mass and t are assumed to be small compared to the centre-of-mass-energy and are neglected in the last part of equations 2.27 and 2.28.

Diffractive Structure Function

The cross section for inclusive diffractive DIS is related to the diffractive structure function F_2^D of the proton, which may be generally defined with five degrees of freedom:

$$\frac{d^5\sigma(ep \rightarrow eXY)}{dx_{\mathcal{P}} d\beta dQ^2 dM_Y dt} = \frac{4\pi\alpha_{em}^2}{\beta^4 Q^4} \cdot \left[1 - y + \frac{y^2}{2(1 + R_2^{D(5)})} \right] F_2^{D(5)}(x_{\mathcal{P}}, \beta, Q^2, M_Y, t), \quad (2.29)$$

where $R_2^{D(5)}$ is the ratio of longitudinal to transverse photon cross sections. The variables Q^2 , $x_{\mathcal{P}}$ and β are reconstructed from the scattered electron and the diffractive hadronic final state. The final system Y , however, is not directly measured in the HERA experiments, for this reason the cross section is often integrated over $M_Y < 1.6$ GeV and $|t| < 1$ GeV², leaving a differential cross section and a diffractive structure function with only three degrees of freedom. The reduced diffractive cross section can be related to the diffractive structure functions by

$$\sigma_r^{D(3)}(x_{\mathcal{P}}, \beta, Q^2) = F_2^{D(3)}(x_{\mathcal{P}}, \beta, Q^2) - \left[1 - y + \frac{y^2}{2} \right] F_L^{D(3)}(x_{\mathcal{P}}, \beta, Q^2). \quad (2.30)$$

Figure 2.9 shows the latest measurement of $\sigma_r^{D(3)}$ by H1 [17]. The quantity $x_{\mathcal{P}}\sigma_r^{D(3)}$ is shown for values of β between 0.1 and 0.9 and Q^2 from 1.5 to 150 GeV.

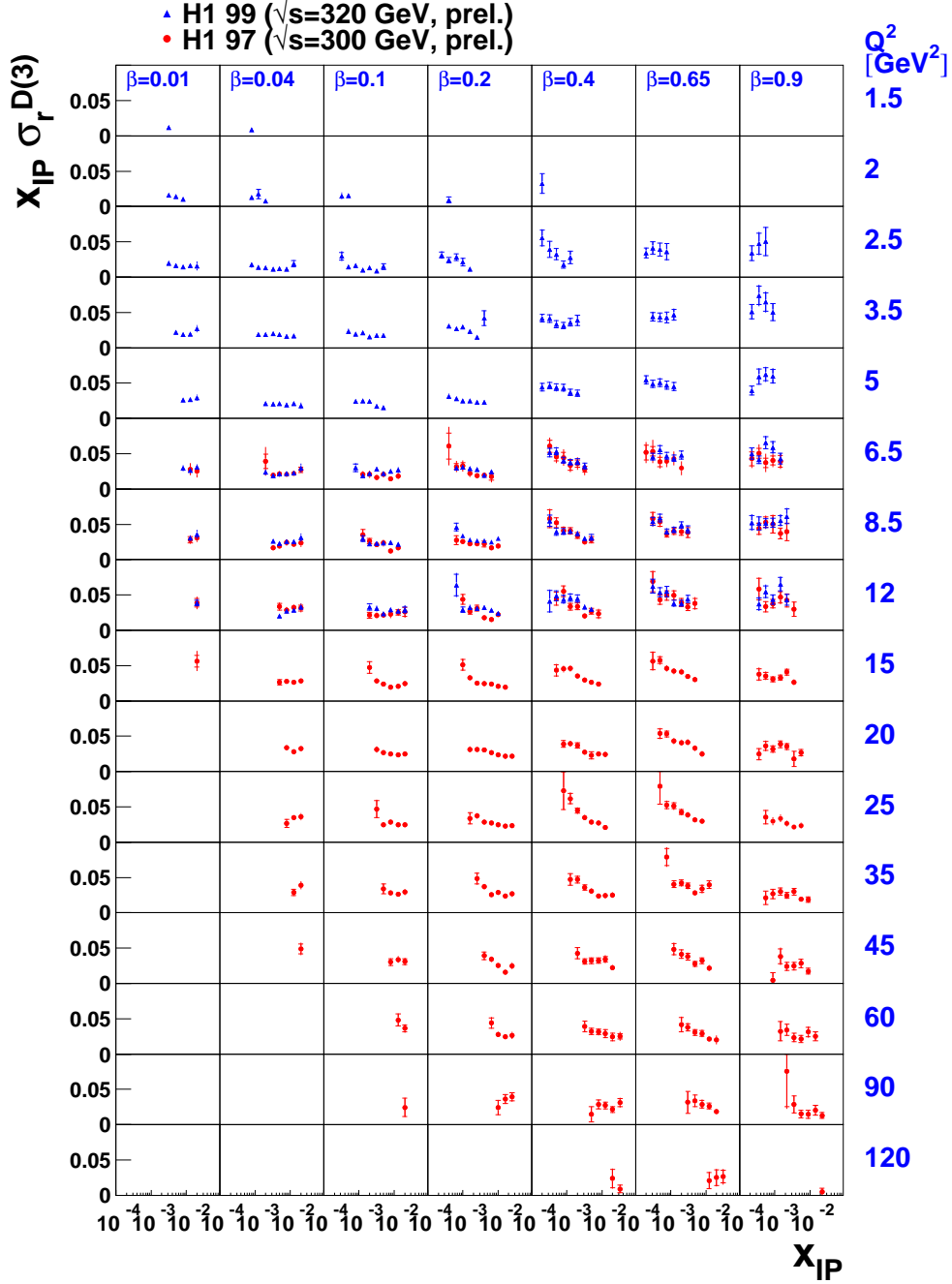


Figure 2.9: The diffractive reduced cross section $\sigma_r^{D(3)}$ as measured by H1 [17], plotted as $x_{IP} \sigma_r^{D(3)}$ in bins of x_{IP} for various β and Q^2 values.

2.7 QCD Hard Scattering Factorisation for Diffractive DIS

It has been proven by Collins [18] that the cross section for the diffractive process $\gamma^* p \rightarrow p' X$ can be written in terms of the universal diffractive parton distributions of the proton, $q^D(x_{\mathcal{P}}, \beta, Q^2, t)$ convoluted with the partonic cross section $\hat{\sigma}_{\gamma^* q}$.

$$\sigma(\gamma^* p \rightarrow p' X) \sim q^D(x_{\mathcal{P}}, \beta, Q^2, t) \otimes \hat{\sigma}_{\gamma^* q}(x, Q^2). \quad (2.31)$$

The factorisation formula is valid for large enough Q^2 and at fixed $x_{\mathcal{P}}$ and t . This ansatz states the independence of the hard subprocess from the soft part of the interaction at the proton vertex. QCD hard scattering factorisation enables to predict hard diffractive final states using diffractive PDFs extracted in inclusive diffractive DIS. The diffractive PDFs, q^D , which are not known from first principles, should obey the DGLAP evolution equations and they can be determined from measurements by a DGLAP QCD fit to the inclusive diffractive DIS cross section.

2.8 Regge Factorisation Approach

The Ingelman-Schlein model [19], assumes a pomeron with partonic structure and therefore applicability of Regge phenomenology of soft hadronic interactions to the concept of diffractive parton distributions. This leads to the factorisation

$$f_i^D(x, Q^2, x_{\mathcal{P}}, t) = f_{\mathcal{P}/p}(x_{\mathcal{P}}, t) \cdot f_i^{\mathcal{P}}(\beta, Q^2), \quad (2.32)$$

where $\beta = x/x_{\mathcal{P}}$ and $f_{\mathcal{P}/p}(x_{\mathcal{P}}, t)$ denotes a pomeron flux factor, describing the probability of emission of a pomeron by the proton. Further, the hypothesis of Regge factorisation allows to split the diffractive structure function into two terms, one of them describing the pomeron-proton vertex, the other the pomeron-photon interaction. The diffractive structure function can then be expressed as

$$F_2^{D(4)}(x_{\mathcal{P}}, t, \beta, Q^2) = f_{\mathcal{P}/p}(x_{\mathcal{P}}, t) \cdot F_2^{\mathcal{P}}(\beta, Q^2), \quad (2.33)$$

where the pomeron structure function, $F_2^{\mathcal{P}}(\beta, Q^2)$, describes the partonic structure of the pomeron. In analogy to $F_2(x, Q^2)$, $F_2^{\mathcal{P}}(\beta, Q^2)$ is related to the pomeron parton distributions by

$$F_2^{\mathcal{P}}(\beta, Q^2) = \sum_{i=1}^{N_f} e_i^2 \beta \left\{ q_i^{\mathcal{P}}(\beta, Q^2) + \bar{q}_i^{\mathcal{P}}(\beta, Q^2) \right\}, \quad (2.34)$$

where i denotes the quark flavour and e_i their electric charge. Additionally to the quark contribution, the gluon parton density $g(\beta, Q^2)$ is also defined.

With the factorisation ansatz presented in 2.33 the H1 F_2^D measurements can be described, if diffraction is considered as a sum of pomeron and reggeon exchanges. Then the diffractive structure function is expressed as

$$F_2^{D(4)}(x_{\mathcal{P}}, t, \beta, Q^2) = f_{\mathcal{P}/p}(x_{\mathcal{P}}, t) \cdot F_2^{\mathcal{P}}(\beta, Q^2) + f_{\mathcal{R}/p}(x_{\mathcal{P}}, t) \cdot F_2^{\mathcal{R}}(\beta, Q^2), \quad (2.35)$$

In Regge theory, the pomeron (reggeon) flux is written as

$$f_{\mathcal{P}(\mathcal{R})/p}(x_{\mathcal{P}}, t) \sim f(t) \cdot \left(\frac{1}{x_{\mathcal{P}}} \right)^{2\alpha_{\mathcal{P}(\mathcal{R})}(t)-1}, \quad (2.36)$$

where $\alpha_{P(R)}(t) = \alpha_{P(R)}(0) + \alpha'_{P(R)} \cdot t$ is the effective Regge trajectory for the pomeron (reggeon). A fit of this form was made to the H1 data. The value of the reggeon intercept, obtained by this fit, is found consistent with the previously measured, whereas the value of the pomeron intercept is significantly larger than the soft pomeron intercept measured in inclusive hadron-hadron collisions.

$$\alpha_P(0) = 1.173 \pm 0.018 \text{ (stat.)} \pm 0.017 \text{ (syst.)} \begin{matrix} +0.063 \\ -0.035 \end{matrix} \text{ (model)} \quad (2.37)$$

The pomeron parton densities are determined in the DGLAP fits to F_2^D . The PDFs are parametrised at a starting scale $Q_0^2 = 3 \text{ GeV}^2$, and then evolved to larger Q^2 . In Figure 2.10 the gluon and singlet distributions (taken from [20]) are shown as a function of the variable z , which is equal to β when the photon interacts with a quark, and it is equal to the momentum fraction carried by the gluon, when the parton entering the hard scattering is a gluon. Figure 2.10 shows, that the parton densities are dominated by gluons, they carry $\approx 80 \%$ of the pomeron momentum.

2.9 Diffractive Charm Production

As already introduced in Section 2.4, charm at HERA is predominantly produced via the boson-gluon fusion. In the following several models of diffractive charm production, which will be later used for comparison with data, are briefly discussed.

2.9.1 Factorisable Pomeron Approach

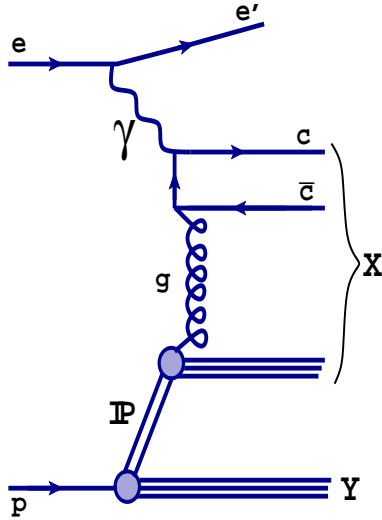


Figure 2.11: *Photon-gluon fusion in the factorisable pomeron approach.*

Parton distributions extracted from the QCD fits to the diffractive structure function $F_2^{D(3)}$, as introduced in Section 2.8, are used for the calculation of charm production in diffractive processes. In the present analysis, the parton distributions are taken from [20].

Figure 2.11 shows a Feynman diagram for charm production in the factorisable pomeron approach. The incoming lepton radiates the photon, which interacts with a gluon of the pomeron. The gluon carries a fraction z_P , of the pomeron momentum. In the case of charm production, z_P may be written as

$$z_P = \beta \left(1 + \frac{\hat{s}}{Q^2} \right) \simeq \frac{Q^2 + M_{c\bar{c}}^2}{Q^2 + M_X^2}, \quad (2.38)$$

In the collinear factorisation approach, diffractive charm production can be simulated using the Monte Carlo event generator RAPGAP [22] (see Section 4).

2.9.2 Perturbative Two-Gluon Exchange Model

At high energy, in the proton rest frame, the photon may fluctuate into partons long before the interaction with the proton takes place. The simplest case is the formation of

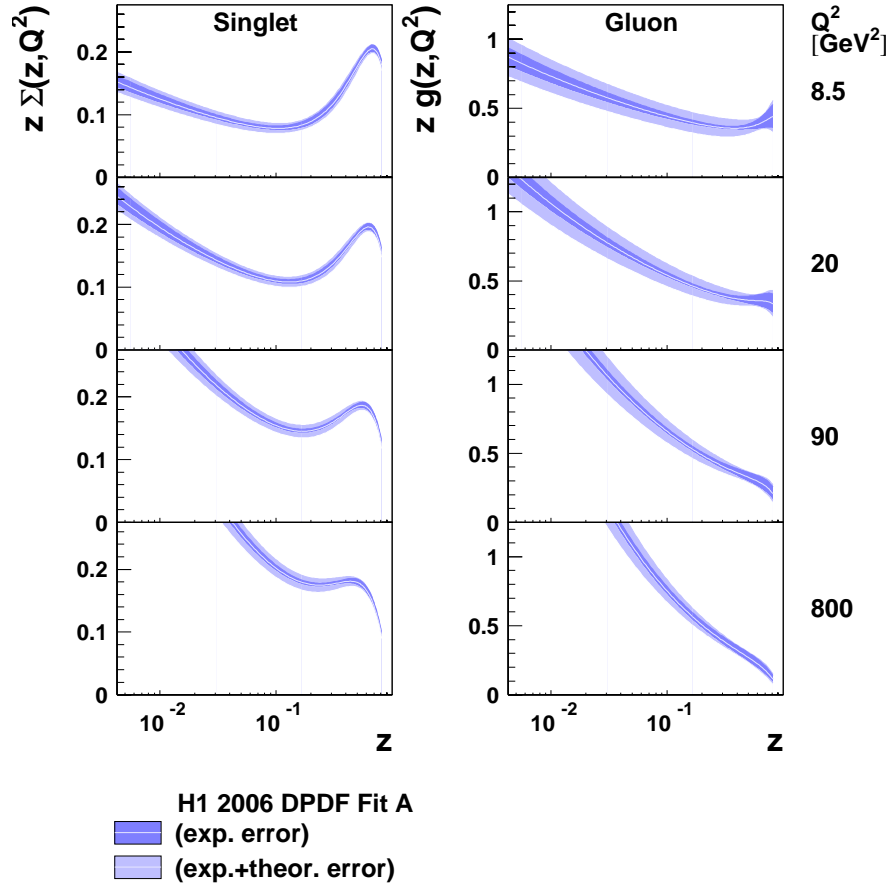


Figure 2.10: Parton distributions of the pomeron (from [21]) at NLO as determined in DGLAP fits to the H1 $F_2^{D(3)}(x_P, \beta, Q^2)$ measurements. The distributions are presented as functions of z for the different Q^2 bins, where $z = \beta$ for quark distributions. On the left the quark distributions, on the right the gluon distributions are shown.

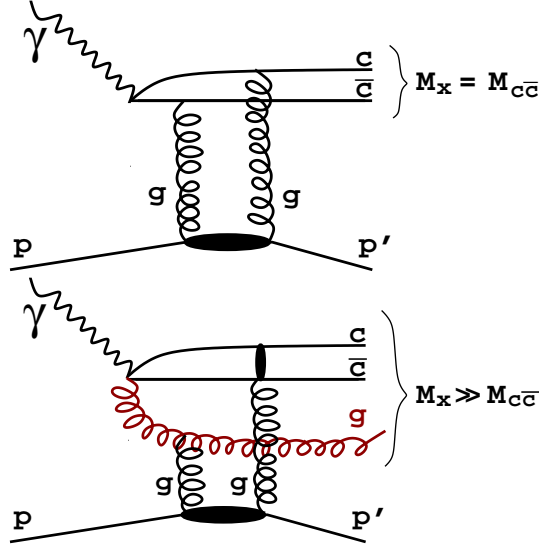


Figure 2.12: *Diffractive charm production in the perturbative two-gluon exchange model. Processes of the type $\gamma^* + p \rightarrow c\bar{c} + p'$ (top) and $\gamma^* + p \rightarrow c\bar{c}g + p'$ (bottom) are shown.*

a $q\bar{q}$ pair, which forms a *colour dipole*. Furthermore, before the photon interacts with the proton, the $q\bar{q}$ pair may radiate additionally gluons and may thereby create a $q\bar{q}g$ state (see Figure 2.12). If the proton stays intact, diffractive elastic events with a large rapidity gap are formed. In that case, the diffractive system is represented by the colour dipole and the pomeron can be modelled by colour singlet gluon exchange between the dipole and the proton. Two is the minimal number of gluons needed to reproduce the pomeron quantum numbers.

The nature of the exchanged gluons can be explained differently, for example in [23] the gluons are treated as non perturbative. In contrast to this, in [24] gluons have a hybrid status and include non perturbative and perturbative components.

Bartels et al investigated the production of charm in diffraction via partonic fluctuations of the photon, using the un-integrated parton distribution functions (uPDFs) obtained from a fit to the inclusive Structure Function $F_2(x, Q^2)$ evolved by the CCFM evolution equations [25, 26]

The cross section has been calculated for the fluctuation of the photon into a $c\bar{c}$ pair. These calculations are implemented in the RAPGAP Monte Carlo program, so that different parametrisations of the gluon density in the proton are available and different $x_{\mathbb{P}}$ dependences of the cross sections are expected.

2.9.3 Soft Colour Interactions

The basic assumption in the soft colour interaction model [27] is that the hard subprocesses in diffractive events are the same as in typical DIS events.

The rapidity gap, the peculiar attribute of a diffractive event, provided by the colour singlet exchange, results within the scope of this model from soft interactions which rearrange the colour state of the partons without affecting their momenta. The Figure 2.13

shows a typical string configuration in the Lund string model and a possible string configuration after the colour rearrangement.

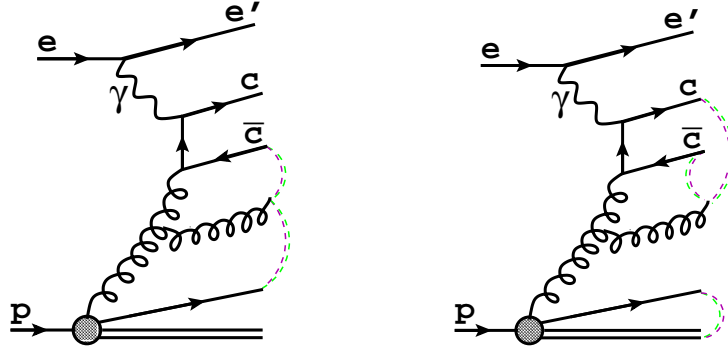


Figure 2.13: Charm production via photon-gluon fusion and soft colour interactions. A rapidity gap (on the right) is produced after rearrangement of strings indicated in the figure between the outgoing partons of the hard sub-process.

2.10 Monte Carlo Generators

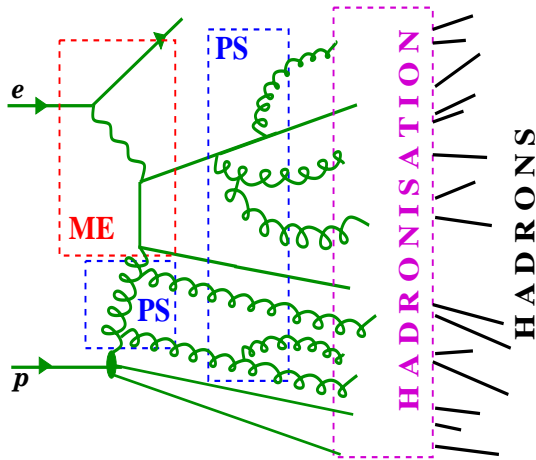


Figure 2.14: *General structure of a Monte Carlo generator.*

The Figure 2.14 shows a sketch of the subsequent steps of a Monte Carlo event generator. The hard matrix element (ME) is calculated in leading order. The struck quark in deep inelastic scattering can emit partons before and after the hard scattering vertex, which lead to the initial or final state parton showers (PS). The gluons and quarks, which are not directly observable due to the confinement mechanism of the QCD, hadronise into colour neutral mesons and baryons. This mechanism being provided by phenomenological methods. After these steps, a generated event consists of particles, represented by four-vectors. Next, in order to use a generated Monte Carlo events for the comparison with experimental data, a program is applied which simulates the detector response (in H1 the program H1SIM). After this, a simulated event is equivalent to an event in the real measured data. The last treatment of simulated events is performed by a program which reconstructs Monte Carlo events in the same way as the experimental data from the H1 detector (H1REC).

In this analysis, the RAPGAP Monte Carlo program is used to produce deep inelastic and diffractive events. In Section 4 will be given a detailed overview of the RAPGAP Monte Carlo program, and details of this simulation program which are used in the analysis are discussed.

For the QCD calculations usually Monte Carlo event generators are used. Monte Carlo programs serve to compare experimental data with theoretical predictions and also to correct the measured data for detector effects.

A Monte Carlo generator produces a quantity of events, whose statistical distributions follows the implemented physical models. Typically, the number of events which are generated by a Monte Carlo program is at least one order of magnitude larger than the number of events in an analysed data sample. In consequence of this, the statistical errors of the Monte Carlo simulations can be neglected.

Chapter 3

The H1 Experiment at HERA

In this chapter the HERA¹ machine, the first storage ring, in which different particles types are brought into collision, is introduced. Afterwards the main subdetectors of the H1 detector at HERA, which were used to measure the data analysed in this thesis, are discussed.

3.1 The HERA Collider

The HERA accelerator is a 6.4 km circumference ring situated at the DESY² laboratory in Hamburg, Germany. It consists of two independent accelerators which produce counter-rotating beams of positrons³ and protons.

The final energy of the positrons is $E_e = 27.5$ GeV and the energy of proton beam is 920 GeV since 1998. The available centre-of-mass energy E_{CM} is

$$E_{CM} = \sqrt{s} \simeq \sqrt{4E_p E_e} \simeq 320 \text{ GeV}. \quad (3.1)$$

It is one order of magnitude larger than the energies achieved in fixed target lepton nucleon scattering experiments.

In HERA, protons and positrons are stored in up to 220 bunches. From these bunches approximately 175 are *colliding bunches*, the others, called *pilot bunches*, are not brought into collision and are used to study the background induced by the interactions of the beam with the residual gas in the beam pipe, or with the wall.

A schematic overview of the HERA accelerator is shown in the Figure 3.1. The positrons and the proton beams are collided at the north and the south interaction points, where, respectively, the H1 and the ZEUS detectors were built to study ep collisions. More information on HERA can be obtained from [28].

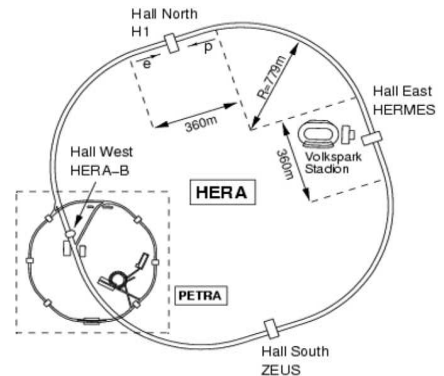


Figure 3.1: Schematic layout of the HERA accelerator .

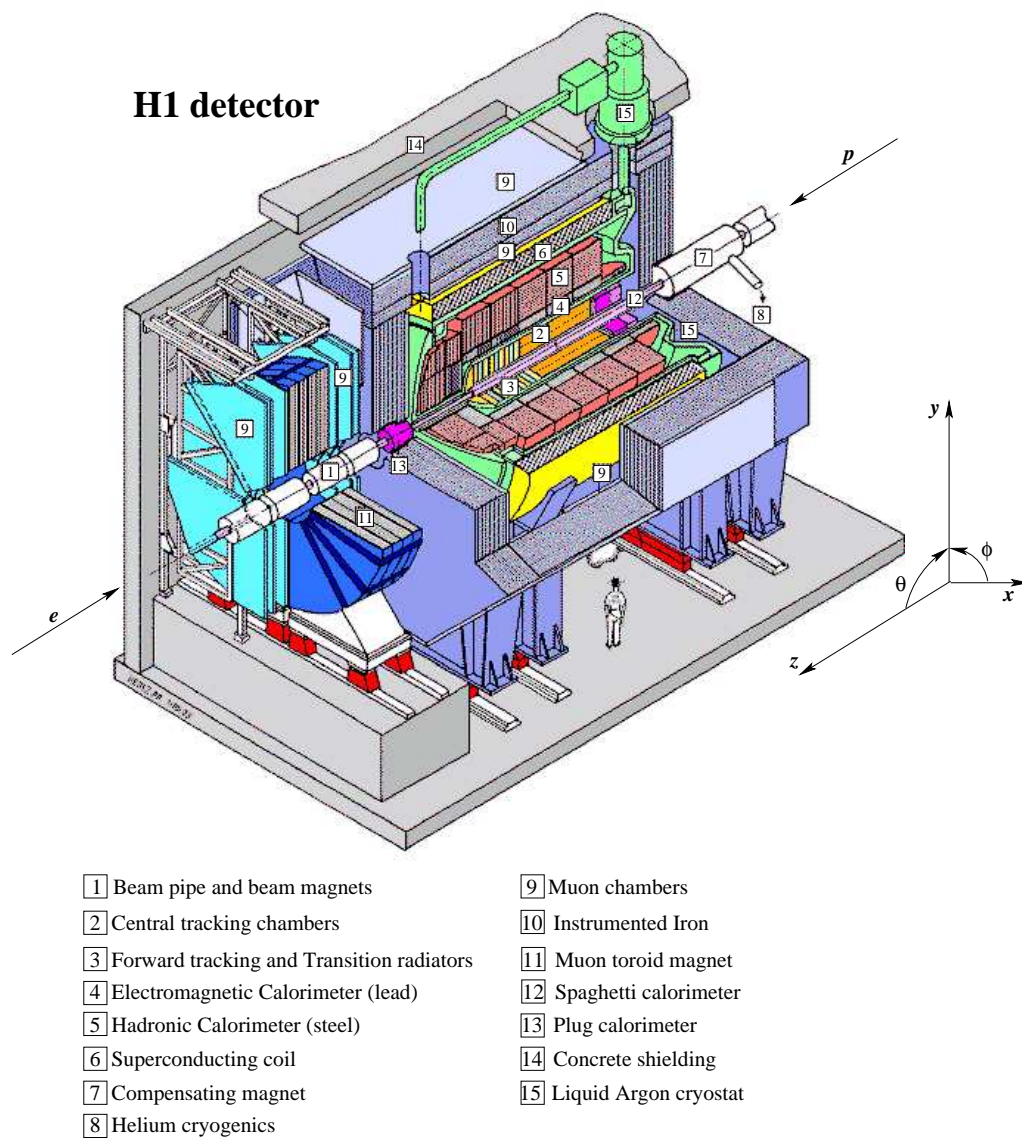


Figure 3.2: Schematic view of the H1-Detector.

3.2 Overview of the H1 Detector

The H1-Detector is a multi-purpose detector, which consists of a number of subsystems. It is designed to measure the structure of the proton, to study the fundamental interactions between particles, and to search for physics beyond the Standard Model of the elementary particles.

Figure 3.2 shows a cut-away view of the H1-Detector, where the positron beam enters at bottom-left and the proton beam at top-right. The H1 coordinate system is defined such that the positive z -axis goes along the proton beam direction. The region of the outgoing proton is often referred to as the *forward* region, to mark the direction of the outgoing positron the term *backward* region is used.

Because of the large difference in energy between the positron and proton beams, the detector is asymmetric with respect to the beam axis and highly segmented in the forward direction in order to provide an effective reconstruction of the hadronic final state.

The H1-Detector is designed to study all aspects of ep scattering, therefore the general design is similar to the standard scheme of collider experiments in high-energy physics. First of all, the interaction point is surrounded by a tracking system, after this by electromagnetic and hadronic calorimeters. The outermost part of the detector is formed by the muon system.

In the following sections the subdetectors relevant for this analysis are presented. A more detailed description of the H1-Detector can be found in [29,30].

3.3 The Tracking System

Figure 3.4 shows the layout of the H1 tracking system longitudinally. The tracking system is subdivided into several parts: The central tracker consists of concentric drift and proportional chambers and covers the angular range $11^\circ < \theta < 169^\circ$. The forward tracking system has similar composition and the angular covering is $5^\circ < \theta < 25^\circ$. The backward region $155^\circ < \theta < 178^\circ$ is covered by the backward drift chamber (BDC).

The central jet chamber (CJC), the central silicon tracker (CST), the central inner and outer z -chambers (CIZ/COZ) and the central inner and outer proportional chambers (CIP/COP), which are shown in a radial view in Figure 3.3, compose the central tracker. The reconstruction of the tracks in the central region is based mainly on the inner (CJC1) and the outer (CJC2) jet chambers, they are presented by two gas-filled coaxial cylinders along the beam axis from $z = -1.1$ m to $z = +1.1$ m. The CJC sense wires run parallel to the beam-pipe to give a measurement of r and ϕ coordinates. A space point resolution of $130 \mu\text{m}$ in the $r - \phi$ plane and 2.2 cm in the z has been measured. CIZ and COZ drift

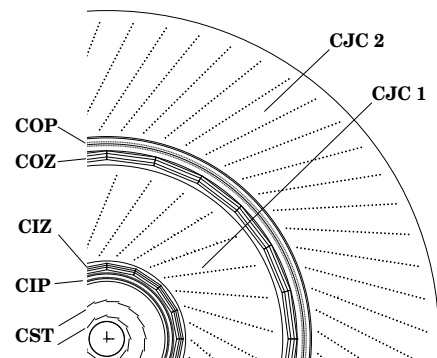


Figure 3.3: The H1 Central Tracking System is shown radially

¹Hadron-Electronen Ring Anlage

²Deutsches Elektronen Synchrotron

³Throughout this thesis, the beam lepton is referred to as a positron

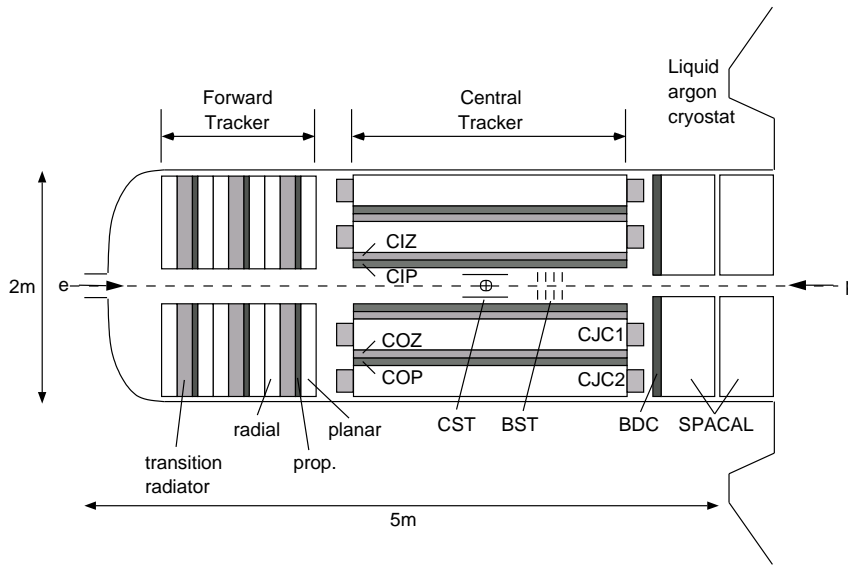


Figure 3.4: *The H1 Tracking System (longitudinal cut).*

chambers enable a better measurement of the z -coordinate of the track position than is possible from the charge division of the CJC signal. The resolution of these z -chambers, located inside and outside of CJC1 is about $260 \mu\text{m}$. With the help of two proportional chambers, CIP and COP, the triggering and timing information for the central trackers is supplied.

The forward tracker consists of three identical supermodules shown in figure 3.4, which contain planar drift chambers, multi-wire proportional chambers, a transition radiator and radial drift chambers.

The backward drift chamber (BDC) is used mainly to measure the direction of the scattered electron. It is designed to determine the polar angle of scattered electron and hence to reconstruct the DIS kinematics of an event.

3.4 Calorimetry in the H1 Detector

For the energy measurements of high-energetic particles and jets, the H1 detector is supplied with a system of calorimeters. The Liquid Argon and the backward spaghetti (SpaCal) calorimeters are placed around the interaction point. The Plug calorimeter is situated around the forward beam pipe. A further outer calorimeter, the so-called Tail Catcher, is not used in this analysis. Figure 3.5 shows schematically the positions of the calorimeters in the H1 detector.

The Liquid Argon Calorimeter

The Liquid Argon Calorimeter (LAr) is the most important detector for measuring the energies of the final state particles from ep interactions. The range of polar angular coverage is $4^\circ < \theta < 154^\circ$. It is a sampling calorimeter which is located in a cryostat. The LAr is segmented along the z -axis into eight wheels. Most wheels consist of an inner

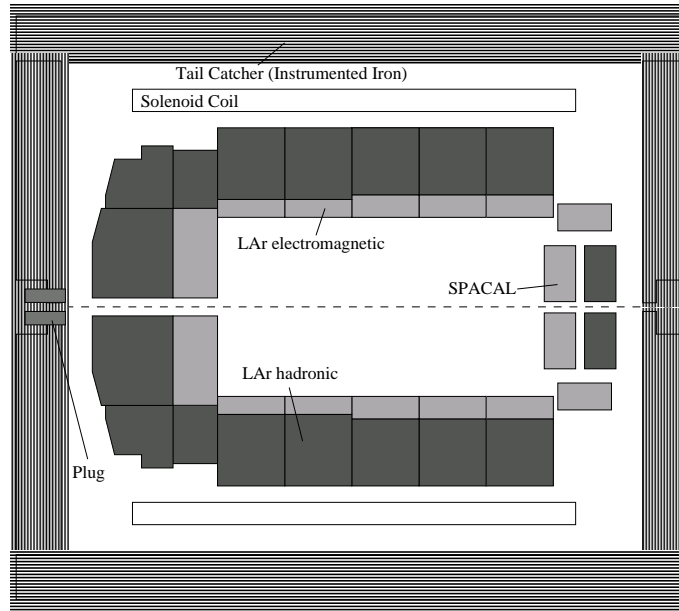


Figure 3.5: Schematic view of the H1 calorimeter. The LAr calorimeter with electromagnetic and hadronic parts, the backward calorimeter SpaCal, the surrounding Tail Catcher and the Plug calorimeter are shown.

electromagnetic and an outer hadronic section⁴. The total number of read-out channels is about 45000.

The energy resolution for the electromagnetic interacting particles was determined to $\sigma(E_{e.m.})/E \sim 12\%/\sqrt{E/\text{GeV}} \oplus 1\%$ [31].

The LAr is a non-compensating calorimeter, that means that the response of hadrons is smaller than that of the electrons of the same energy. In order to correct this effect, a weighting technique based on a shower shape analysis is applied. The energy resolution for hadrons is $\sigma(E_{had.})/E \sim 50\%/\sqrt{E/\text{GeV}} \oplus 2\%$ [32].

The SpaCal Calorimeter

The backward spaghetti calorimeter [33,34] is used for the energy and angle measurements of the scattered positron in DIS events with $1 < Q^2 < 100 \text{ GeV}^2$. The polar angular range of the SpaCal is $151^\circ < \theta < 178^\circ$. The calorimeter consists of scintillating fibres embedded in lead. If a particle reaches this calorimeter, secondary particles are produced due to interactions with lead, whose total energy is then measured in the scintillating fibres. About 1300 channels are read out with a time resolution of 1 ns. This timing information is also used to provide time-of-flight information for the energy deposition in the SpaCal.

The SpaCal has an inner electromagnetic and an outer hadronic part. The electromagnetic energy can be measured with a resolution of $\sigma_E/E = 7.5\%/\sqrt{E/\text{GeV}} \oplus 1\%$. In the hadronic part of the calorimeter, the energies are measured with a resolution of $\sigma_E/E = 30\%/\sqrt{E/\text{GeV}} \oplus 7\%$. Figure 3.6 shows the design of the SpaCal calorimeter.

⁴The wheel located at the most backward point has only electromagnetic section.

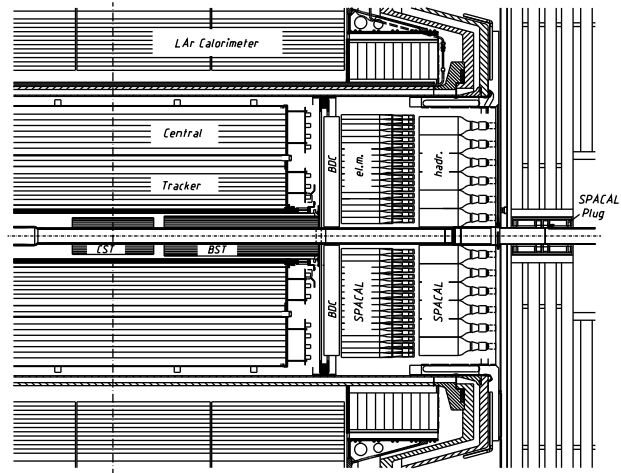


Figure 3.6: *The backward region of the H1 detector. The positions of the electromagnetic and hadronic parts of the SpaCal calorimeter are shown.*

The Plug Calorimeter

The Plug Calorimeter covers the extreme forward angular direction $0.6^\circ < \theta < 3^\circ$. The Plug is designed to close the gap in acceptance for the energy flow measurements between the beam pipe and the most forward part of the LAr calorimeter, and thereby making possible the investigation of the recoiling hadrons in the region close to the proton remnant.

The Plug is a Silicon-Copper sampling calorimeter. It consists of two half cylinders, each half with nine copper absorber plates and eight sampling layers of silicon. In figure 3.7 the structure of the Plug and an expanded view of one detector module is schematically shown.

The hadronic energy resolution of $\sigma_E/E = 150\%/\sqrt{E/\text{GeV}}$ is rather poor, because of the coarse sampling, energy leakage and the large amount of dead material in front of the device [35].

In this analysis the Plug is used in the selection of diffractive events with rapidity gaps.

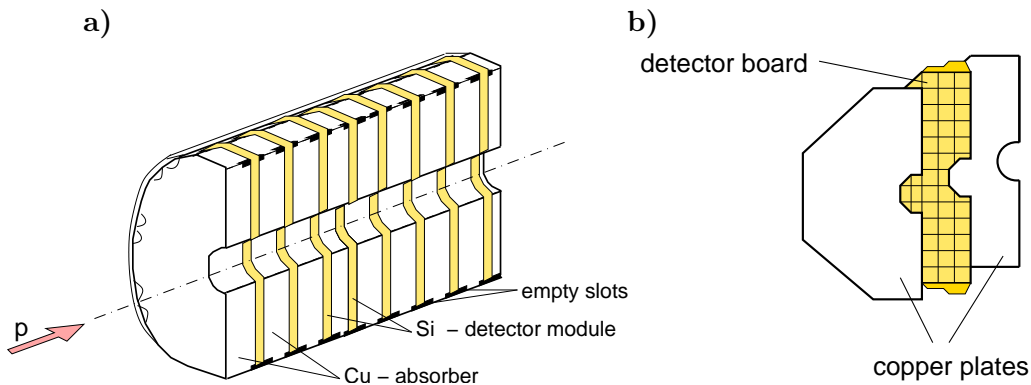


Figure 3.7: *The Plug calorimeter. (a) Half-Plug structure. (b) An exploded view of the Si-detector module with two adjacent Cu-absorber plates.*

3.5 Forward Detectors

In this section the Forward Muon Detector and the Proton Remnant Tagger are shortly described. These detectors are located along the p -direction. In this analysis they are used to tag the proton remnant particles or their secondary particles.

The Forward Muon Detector

The Forward Muon Detector (FMD) (schematically shown in the Figure 3.8) is mounted between 6.4 m and 9.4 m in the forward direction of the interaction point and originally designed for the triggering and reconstruction of muons.

The FMD consists of six double layers of drift chambers and an iron toroidal magnet, where three double layers are situated on either side of the magnet. Four double layers have their wires tangentially to the beam axis and they enable a measurement of the polar angle θ , the other two have wires parallel to the radial direction and measure the azimuthal angle ϕ . The Figure 3.9 shows the cell structure of the θ and ϕ double layers of the FMD. The polar angle coverage of the FMD is $3^\circ < \theta < 18^\circ$.

The FMD is sensitive to particles at smaller angles, thanks to this property, the FMD is used in this analysis to tag the production of hadrons in the forward pseudo-rapidity range, by detecting and reconstructing track segments of the charged particles produced in secondary interactions of these hadrons with material of the beam pipe or the beam pipe gas.

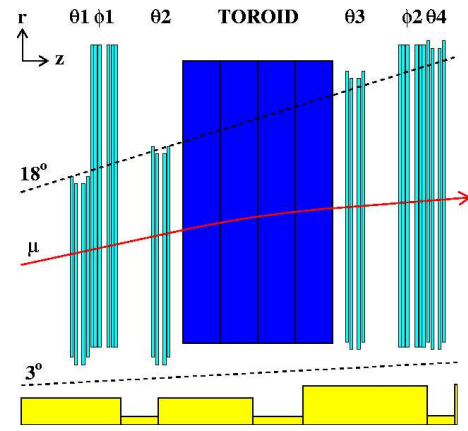


Figure 3.8: *The Forward Muon Detector.*

a)

b)

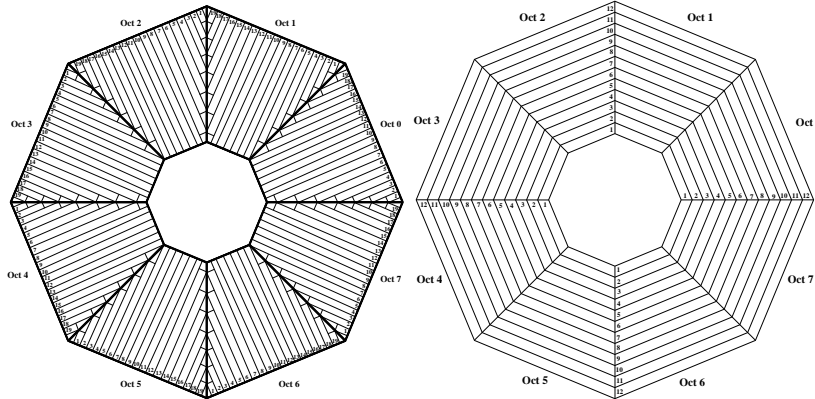


Figure 3.9: *The structure of the FMD layers. (a) The xy -projection showing a ϕ -layer. (b) The xy -projection of the θ_1 -layer.*

The Proton Remnant Tagger

The Proton Remnant Tagger (PRT) is situated 24 m away from the nominal interaction point in the forward direction. This very forward detector is sensitive to particles resulting from the dissociation of the proton into a low mass system in the pseudo-rapidity range $6 < \eta < 8$.

The PRT consists of seven detectors placed around and between the beam pipes. Each detector is made of two scintillators sandwiched between layers of lead shielding and read out by photomultipliers. A signal in the PRT is considered only if both scintillators fire in coincidence within the expected time.

Figure 3.10 shows an overview of the seven PRT scintillators and the location of this detector with respect to the H1 main detector.

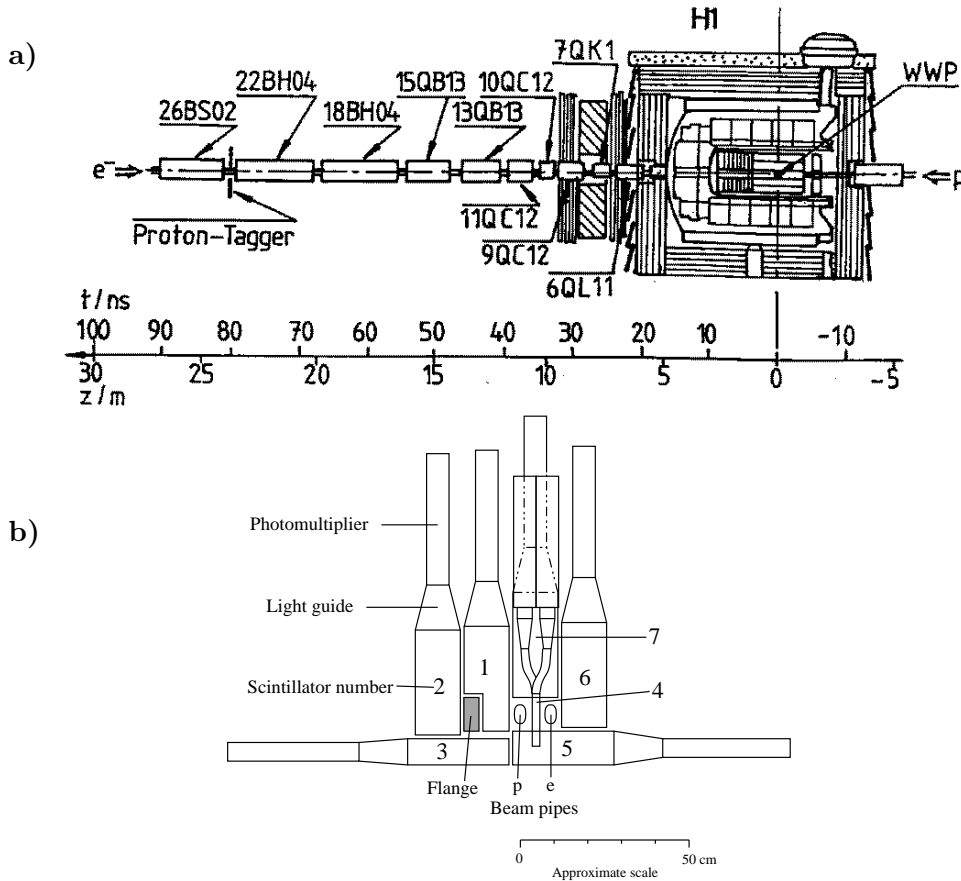


Figure 3.10: (a) The Proton Remnant Tagger is located 24 m away from the nominal interaction point. The H1 detector, the beam-pipe and the focusing magnets are shown. z is the distance from the interaction point, t presents the time of flight of relativistic particles. (b) Schematic diagram of the PRT, showing the seven scintillators.

3.6 The Time-of-Flight System and Luminosity Measurement

The Luminosity Measurement

The luminosity is determined by measuring the rate of the Bethe-Heitler process $ep \rightarrow ep\gamma$, whose cross section can be precisely calculated in QED. The luminosity system [36] is installed in the accelerator tunnel in the direction of the outgoing positron and consists of the Electron Tagger (ET), mounted close to the positron beam pipe at $z = -33.4$ m, and the Photon Detector (PD) at $z = -102.9$ m. Both are Čerenkov calorimeters.

Two different methods are available to determine the luminosity. In the online method, the luminosity calculation is based on the rate of coincident detection in both detectors. In the offline mode, only the photon rate in PD is used. Using the latter method the luminosity can be measured with a precision of 1.5 %.

The Time-of-Flight System

The Time-of-Flight (ToF) system is used to reject the background coming from beam-wall and beam-gas interactions.

The time of arrival of particles from ep -interactions, at a particular point in the H1 detector, is different from the time of particles from interactions outside the vertex region. This property is used by the ToF system.

The ToF counters are installed in the backward region of H1 (BToF), around the beam pipe in the region of FMD (FToF), within the unused space of the Plug absorber (PToF) and they are used to veto events which have a background time signature. As it was already mentioned in section 3.4, ToF information is also provided by the SpaCal calorimeter.

3.7 The Trigger System

A trigger system is needed in order to select interesting physics processes from a large number of background events. The H1 experiment is equipped with a four level triggering system⁵.

L1 is the first level trigger, which decides whether to keep events or not within 2.5 μ s. An event is kept, if one of the 128 L1 subtriggers has fired. These 128 subtriggers are logically combined from 192 trigger elements, which signals are provided by individual detector components.

The second trigger level L2 is used to verify the L1 decision. Neural networks and topological triggers are implemented on L2. On this level, the decision to reject an event or not has to be made within 20 μ s. The L1 subtrigger used in this analysis has no L2 trigger requirement.

On the L4 trigger level, all detector information is available. Up to 30 events can be hold in the buffer and processed independently by a farm of computers. On L4, a fraction of events are reconstructed, the so called *monitor trigger* events are selected, and using *event finders* interesting physics channels are detected. 20 ms are available for the decision on this trigger level.

⁵Only four trigger levels were used, when the data, analysed in this thesis, were recorded.

L5 is presented by an offline treatment. A complete event reconstruction is performed and the information is stored on tapes.

An overview of the L1 trigger elements, which are most relevant for this analysis, is given below.

The z -Vertex Trigger

The z -vertex trigger reconstructs the vertex from signals from the multi-wire proportional chambers (MWPCs) of the CIP and COP and the planar MWPC in the first forward tracker supermodule and sends this information to the L1 trigger.

The coincident MWPC hits that can be connected by a straight line in the rz -plane is defined as a *ray*. The number of these rays fills a histogram. The resulting 16 histograms (one for each ϕ -sector of the chambers) are combined to form the z -vertex histogram, which is shown on Figure 3.11. In this histogram, the bin with the largest number of entries is expected to contain the interaction vertex of the ep collision.

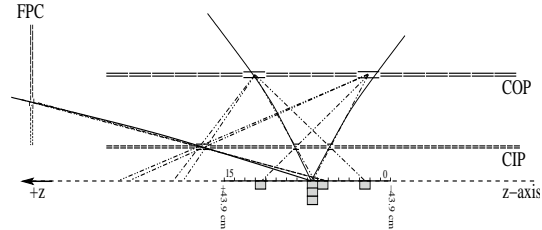


Figure 3.11: The rz -view of the z -vertex histogram for one ϕ -sector is shown.

There is a large variety of conditions in the z -vertex trigger logic. For the purpose of this thesis, the trigger element `zVtx_sig` is interesting. It fires if the z -vertex histogram has a significant peak. More detailed description of the z -vertex design and the working principle can be found in [37].

The SpaCal Trigger

The SpaCal trigger system combines two functions: it provides a DIS positron candidate selection and it also rejects beam-induced background events.

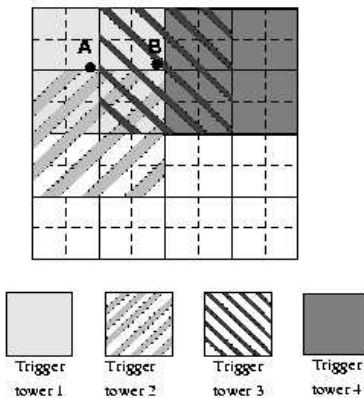


Figure 3.12: Concept of the Inclusive Electron Trigger.

In this analysis, the `SPCLe_IET>2` trigger element for the outer region and `SPCLe_IET_Cen_3` trigger element for the inner region are used, with energy thresholds of 6.5 GeV.

The concept of the ToF system, which vetos the background events, was already shortly introduced in the previous paragraph. For a proper positron selection the Inclusive Electron Trigger (IET) is used.

The IET decision is based only on electromagnetic clusters. The IET is built from arrays of 4x4 neighbouring electromagnetic cells. In order to ensure triggering, the energy sums are performed in overlapping sliding windows, so that each sum overlaps the adjacent windows in both directions. The Figure 3.12 gives a graphical explanation of this overlapping technique.

Three trigger elements are available, each of which has a different cluster energy threshold. In

The DCRPh Trigger

This trigger is responsible for triggering events containing high transverse momentum tracks. It uses information from 10 wire layers of the CJC. The signals of these wires are compared with a predefined track mask, considering drift times, track momentum and position.

A number of trigger elements are available according to multiplicity conditions. In this analysis the `DCRPh_THig` trigger element is used, which fires if at least one track mask above > 800 MeV is found. A detailed description of the DCRPh trigger is presented in [38,39].

Chapter 4

RAPGAP Monte Carlo Samples

Monte Carlo programs generate particles according to a certain physical model. The main steps of the generating, simulating and, finally, reconstructing processes were already introduced in Section 2.10. In this chapter different RAPGAP Monte Carlo generators are discussed.

4.1 Monte Carlo Generator RAPGAP

The RAPGAP Monte Carlo program [40] is used to produce deep inelastic and diffractive events. In this analysis the version 2.8 for the implementation of the deep-inelastic scattering processes and the version 3.10 for the diffractive process is used.

Four samples of simulated Monte Carlo events are used for the correction of the experimental data. One of them provides simulation of standard deep-inelastic scattering events. In the others colour singlet exchange events is simulated. The simulated events are mixed corresponding to the following scheme: diffractive events in the region

$$x_P < 0.1, M_Y < 5 \text{ GeV} \quad (4.1)$$

are accepted, whereas the standard deep-inelastic events are used for

$$x_P > 0.1, M_Y > 5 \text{ GeV} \quad (4.2)$$

4.2 RAPGAP for Elastic Diffractive DIS

This Monte Carlo program uses a perturbative model of diffractive hard scattering in which the pomeron has a partonic substructure. The parametrisation of the pomeron flux factor and parton distribution is taken from the H1 analysis of $F_2^{D(3)}$ [20]. The massive scheme via Boson-Gluon fusion is chosen for the production of charm quarks. Higher order QCD radiative processes are included using an interface to HERACLES and for hadronisation the Lund String model is used.

A part from reggeon exchange is considered separately. Reggeon contribution is simulated using the corresponding reggeon flux parameterisation from the pomeron PDF extraction and parton density functions of the pion.

4.3 RAPGAP for Diffractive Proton Dissociation

This type of the RAPGAP Monte Carlo simulates diffractive processes where the proton dissociates and produces resonance and continuum low mass states Y . The algorithm for the dissociation mechanism is given in analogy to the DIFFVM Monte Carlo generator [41].

In previous diffractive D^* analyses within the H1 collaboration the DIFFVM generator was used to study the kinematical region $M_p < M_Y < 5$ GeV. This was necessary because the programs which are usually used for diffractive phenomena do not contain proton dissociation. The DIFFVM Monte Carlo contains proton dissociation, but is specialised for vector meson production. Although it is possible to use the DIFFVM Monte Carlo program for the description of proton dissociation, a correct description can not be achieved, because of significant differences between vector meson and D^* meson production in diffraction. The RAPGAP generator with proton dissociation is used here which is performed after a variety of adjusting tests. Finally a sample of 20 million events was produced for this D^* analysis.

A parametrisation of the experimental data for the mass spectra of diffractively excited hadrons [42, 43] is used in order to generate the proton-dissociative final state. The dependence of the cross section on t is parametrized according to Regge theory

$$\frac{d\sigma}{dt} \propto e^{-b|t|} \quad (4.3)$$

where b is the slope parameter. Several Monte Carlo samples are generated in order to study the influence of different values of the b parameter on the measured t -slope. Finally $b = 2$ is chosen giving the best agreement with experimental data. For fixed t , in the case of proton dissociation, the inclusive cross section can be written as follows:

$$\frac{d\sigma}{dM_{p-diss}^2} \propto \frac{f(M_{p-diss}^2)}{M_{p-diss}^{2(1+\epsilon)}} \quad (4.4)$$

with M_{p-diss} being the mass of the dissociated system. The function $f(M_{p-diss}^2) = 1$ is assumed in the continuum region, whereas in the resonance region this function results from a fit to the measured cross section for proton dissociation. Within this generator the dissociated system is treated as one of the nucleon resonances $N^+(1520)$, $N(1440)$, $N(1535)$, $N(1650)$, $N(1675)$, $N(1680)$, $N(1700)$ or $N(1710)$.

As long as it is not exactly known, what is the ratio of diffractive events with an elastically scattered proton or a proton in a low-mass state, the mixing of the simulated diffractive events with elastic and dissociated protons is defined in an experimental way. Figures 4.1 and 4.2 present the comparison of the analysed data with Monte Carlo distributions, where the simulated curves represent the sum of all RAPGAP Monte Carlo simulation samples mentioned above. Different ratios for the dissociative and elastic simulation are shown. The Plug Calorimeter and the Forward Muon Detector are chosen for the quantification of the contributions from two different diffractive processes, due to their sensitivity to the dissociated proton. These detectors are able to detect proton remnant particles or their secondaries, produced by interaction with material in the forward region.

In this analysis for the simulated diffractive elastic and dissociated events the following normalisation is used

$$p - dissociation : p - elastic = 1 : 1. \quad (4.5)$$

4.4 RAPGAP for Inclusive DIS

The simulated sample of inclusive DIS events used in this analysis corresponds to an integrated luminosity of 617.44 pb^{-1} .

The parton distributions are convoluted with leading order QCD matrix elements. The renormalisation and factorisation scales are chosen $\mu_f^2 = \mu_r^2 = Q^2 + 4m_c^2 + p_t^2$. The hadronisation effect is implemented according to the Lund String Fragmentation Model for the light and for heavy quarks. With help of the `HERACLES` subprogram radiative QED corrections can be studied.

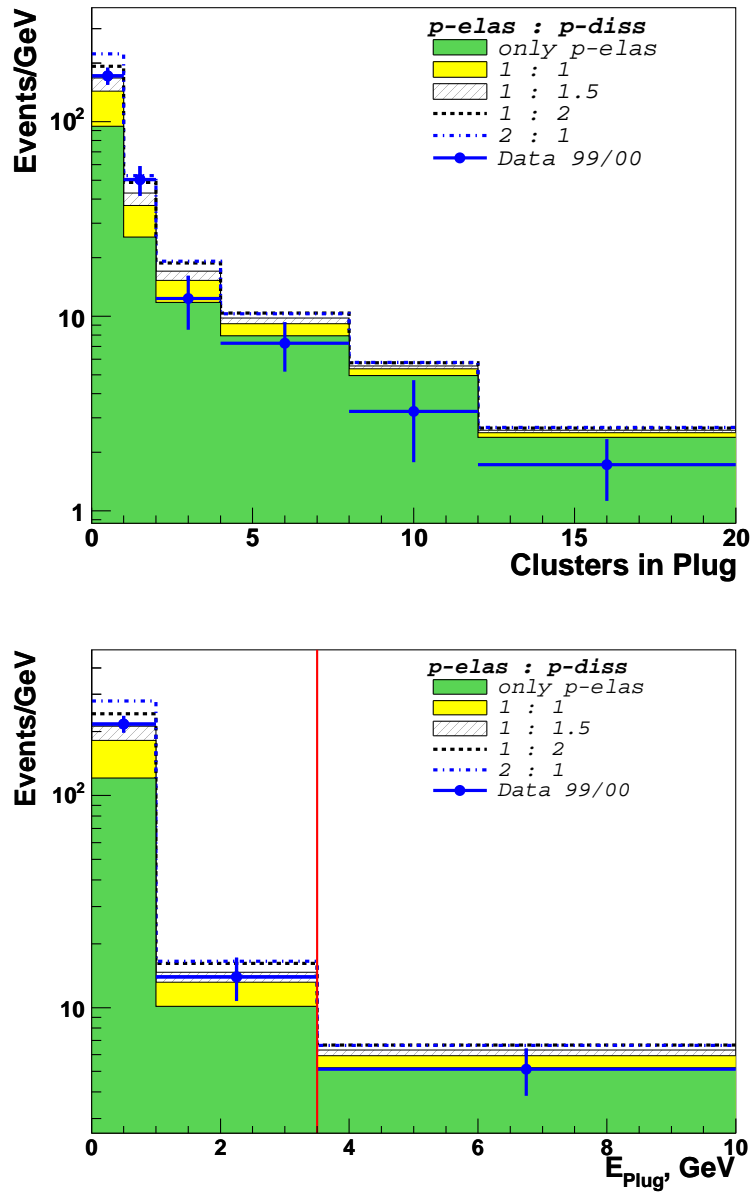


Figure 4.1: Number of clusters and energy deposited in the Plug Calorimeter are shown. The Monte Carlo distributions represent the sum of RAPGAP simulations of inclusive DIS, elastic diffractive DIS (Reggeon and Pomeron contributions) and dissociative events. Different ratios for dissociative and elastic diffractive events are shown. For the final analysis a ratio of 1:1 is chosen.

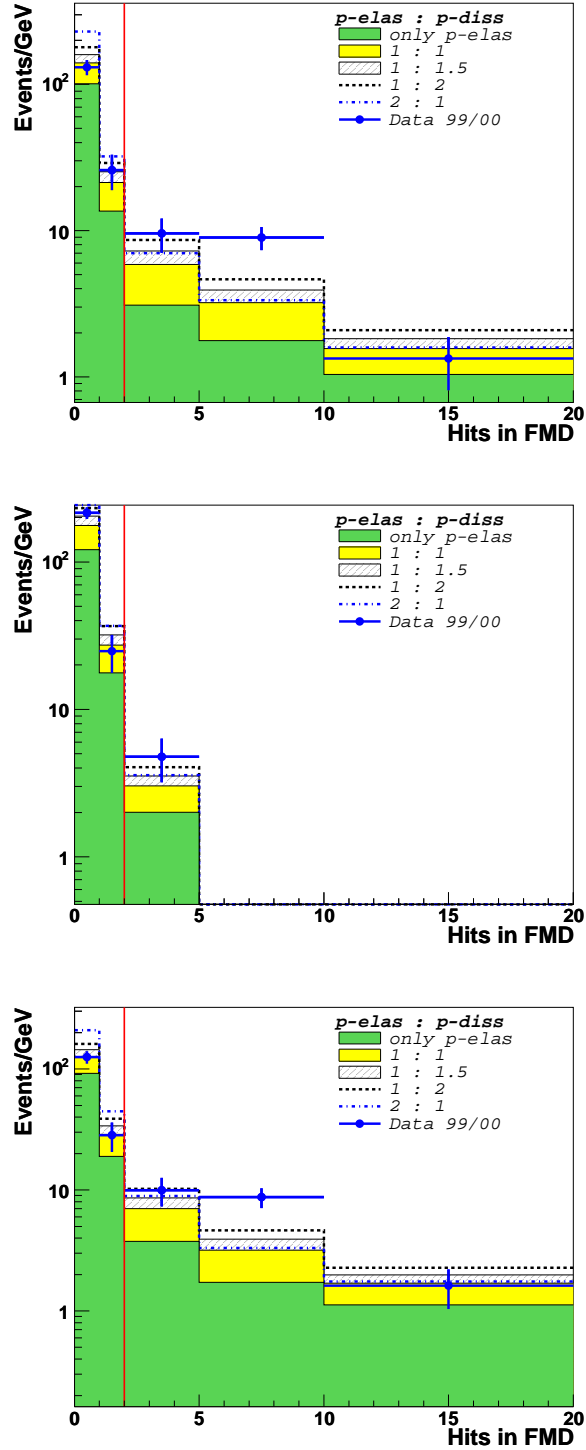


Figure 4.2: *FMD hits distributions are shown for the first two and third layer separately, and as the sum of three pre-toroid layers. Different ratios for dissociative and elastic simulated diffractive events are shown. Monte Carlo distributions are presented by the sum of RAPGAP simulations of inclusive DIS, elastic diffractive DIS (Reggeon and Pomeron contributions) and dissociative events. For the final analysis a ratio of 1:1 is chosen.*

Chapter 5

Data Selection

The selection of data can be subdivided into two parts. The first describes the selection of the deep inelastic scattering events, the second the selection of diffractive events.

5.1 Run Selection

In this analysis data are analysed, recorded with the H1-Detector in the years 1999 and 2000, when the HERA machine collided 27.6 GeV positrons with 920 GeV protons. The data collected in the year 2000, when the interaction region was shifted, are not used in this analysis.

The analysis uses events for which the following detector components were fully operational: the luminosity system, the liquid argon calorimeter (LAr), the central jet chambers (CJC1 and CJC2), the spaghetti calorimeter (SpaCal), the plug calorimeter (Plug), the forward muon detectors (FMD), the proton remnant tagger (PRT) and the time-of-flight scintillators (ToF). In addition, the sub-trigger S61 is used in the analysis, and therefore the central and the forward proportional chambers are also required to be in operation.

Individual runs are classified in H1 as *good*, *medium* and *poor*, according to the operational status of the detector. Only runs classified as *good* or *medium* are used.

In the data taking period, there is a set of runs where the level of noise in the PRT is higher than normal (see section 6.5). These runs are also excluded from the analysis¹.

In order to suppress background events from the so-called satellite bunches, which exist in the positron and proton beams before and after the colliding bunches, a cut on the z -coordinate of the interaction point is applied: $|z| < 35$ cm. Corrections for events which are lost due to this cut are included in calculations of the luminosity.

A summary of the run ranges used in the analysis are given in Table 5.1. The selected runs correspond to a total integrated luminosity of $\mathcal{L}^{int} = 46.8$ pb⁻¹.

5.1.1 The Analysis Subtrigger

The analysed data are triggered by an energy deposition in the SpaCal (sub-trigger S61). This sub-trigger S61 demands a signal from the inclusive electron trigger `SPCLe_IET>2` or `SPCLe_IET_Cen_3` in coincidence with a charged track signal from both the z -vertex trigger `zVtx_sig` and the DCRPh trigger `DCRPh_Thig`. A summary of the definitions of

¹A detailed description of the excluded runs is presented in Appendix A.

Used Run Range \mathcal{L} , [pb ⁻¹]	1999 e ⁺ (244963 - 259486)	2000 nominal (262144 - 279215)
Integrated \mathcal{L} for <i>good</i> and <i>medium</i> runs, after HV selection.	14.22	45.68
Integrated \mathcal{L} after detailed exclusion of <i>bad</i> runs.	13.46	41.11
Average prescale for sub-trigger 61	1.08	1.20
Integrated \mathcal{L} used in the analysis.	12.51	34.24

Table 5.1: *Integrated luminosities for the data-taking periods used in the analysis.*

S61	(SPCLe_IET>2 SPCLe_IET_Cen_3) && DCRPh_THig && zVtx_sig
<i>Trigger elements to detect the scattered electron in the SpaCal</i>	
SPCLe_IET>2	measured electron in the SpaCal, $E \geq 6$ GeV
SPCLe_IET_Cen_3	like SPCLe_IET>2, but for central region in SpaCal
<i>Trigger elements of the central drift chambers CJC1 and CJC2</i>	
DCRPh_THig	at least one fired track mask with $p_t > 800$ MeV
<i>Trigger elements to detect a significant vertex using CIP, COP and FPC</i>	
zVtx_sig	significant maximum in z-vertex-histogram

Table 5.2: *Definitions of the sub-trigger and trigger elements, which are used in this analysis.*

the used subtriggers and the trigger elements are presented in Table 5.2.

5.2 Selection of Deep Inelastic Scattering Events

The Event Vertex

The rate of background events from beam-gas and beam-wall interactions in the detector is relatively high. Such events produce a large number of tracks that do not point to a vertex near the interaction point.

In order to reduce this background, events without a reconstructed vertex within 35 cm along the z -axis are rejected by the cut :

$$-35 < z_{vertex} < 35 \text{ cm.} \quad (5.1)$$

The distribution for z_{vertex} for data and simulation is shown in Figure 5.1a).

The $\Sigma(E - p_z)$ of the Final State

The quantity $\Sigma(E - p_z)$ presents the difference between the energy and z -component of the momentum summed over all final state objects in the event.

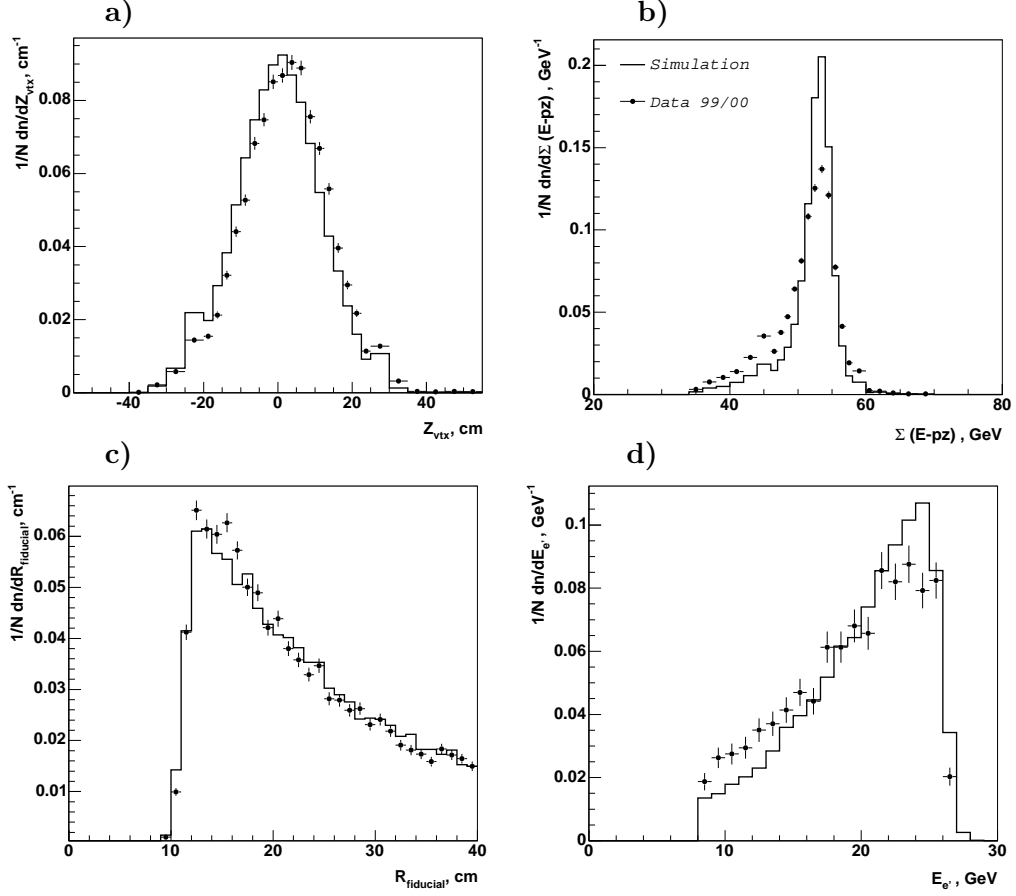


Figure 5.1: Selection of the positron candidates.

If all final state particles were detected and measured in a perfect detector, due to the conservation of energy and momentum, the quantity $\Sigma(E - p_z)$ has to be equal to twice the energy of the positron beam : $\Sigma(E - p_z) = 2E_e \approx 55$ GeV. Any losses of particles in a real detector will lower this value. Therefore a cut

$$35 < \Sigma(E - p_z) < 70 \text{ GeV.} \quad (5.2)$$

is applied. The lower cut is done to reject the photoproduction background, where the scattered positron is lost in the beam pipe. The upper cut rejects poorly reconstructed events. Figure 5.1b) presents the distribution $\Sigma(E - p_z)$ for data and simulation.

The Positron Candidate

The scattered positron in deep inelastic scattering events is identified in the SpaCal by the measured energy deposited in the cells of the calorimeter. The cells are grouped to clusters and the cluster energy is calculated as the sum over all single cell energies.

The scattered positron is defined as the most energetic cluster in the electromagnetic part of the SpaCal. The energy of this cluster is required to be larger than 8 GeV.

$$E_{e'} > 8 \text{ GeV.} \quad (5.3)$$

That is done to reject the background clusters in the SpaCal, which can occur from photoproduction events.

Additionally a cut on $R_{fiducial}$ is applied, where $R_{fiducial}$ is the distance of the center of gravity of the cluster to the beam in the radial direction. This cut ensures that the positrons are detected in the high acceptance area of the SpaCal.

$$R_{fiducial} > 9.1 \text{ cm.} \quad (5.4)$$

In Figure 5.1c), d) $R_{fiducial}$ and $E_{e'}$ distributions are presented.

5.2.1 Kinematic Reconstruction of the DIS Variables

The quantities Q_e^2 , y , and x describe the kinematics of DIS events. These quantities can be reconstructed using various methods which have different sensitivity to QED radiation, to the energy calibration of the calorimeters and to the determination of several variables, required in the analysis. There are different reconstruction methods for these kinematic variables :

- In the **electron method** the kinematics are reconstructed solely from the positron information, namely the energy of the incident and scattered positron and the polar angle of the scattered positron. This method is very sensitive to initial state radiation because it depends directly on the energy of the positron. The electron method has the advantage of being experimentally simple and independent of the sophisticated hadronic final state reconstruction.
- In the **hadron method (Jacquet-Blondel method)** the kinematic variables are reconstructed using the information of the particles in the hadronic final state. Usually, two hadronic quantities are defined: the transverse momentum of the hadrons, p_t^h , and $\Sigma = E^h - p_t^h$, where the Σ quantity is affected by large losses due to the proton remnant. Therefore the hadronic final state variables are less well reconstructed than the quantities used in the electron method.
- The **Σ -method** makes efficient use of information from the electron and hadron methods. This combined method gives a good resolution over a wide kinematic range.
- The **double angle method** uses the angles of the positron and the hadronic final state. It does not rely on any energy measurements, and it is thus very useful for calibration purposes.

A detailed description of the reconstruction methods can be found in [44].

In this analysis the electron method is used. The kinematic variables of the event are reconstructed from the energy of the incident, E_e , and scattered, $E_{e'}$, positron and the angle $\theta_{e'}$ of the scattered positron:

$$Q_e^2 = 4 \cdot E_e \cdot E_{e'} \cdot \cos^2 \left(\frac{\theta_{e'}}{2} \right), \quad (5.5)$$

$$y_e = 1 - \frac{E_{e'}}{E_e} \cdot \sin^2 \left(\frac{\theta_{e'}}{2} \right). \quad (5.6)$$

<i>Decay channel</i>	<i>BR [%]</i>
$D^{*+} \rightarrow D^0 \pi_{slow}^+$	67.7 ± 0.5
$D^0 \rightarrow K^- \pi^+$	3.80 ± 0.09
$D^{*+} \rightarrow K^- \pi^+ \pi_{slow}^+$	2.27 ± 0.06

Table 5.3: Selected decay channels and branching ratios, \mathcal{BR} , of the D^{*+} and of the D^0 meson [46].

The following cuts on Q_e^2 and y_e are applied for the selection of DIS events.

$$2 < Q_e^2 < 100 \text{ GeV}^2, \quad (5.7)$$

$$0.05 < y_e < 0.7. \quad (5.8)$$

The kinematic range in Q^2 is defined by the geometrical acceptance of the SpaCal. At the upper cut, $Q^2 > 100 \text{ GeV}^2$, the positron is scattered into the Liquid Argon calorimeter. The lower cut on Q^2 separates the genuine DIS events from photoproduction events. The upper limit on y corresponds to the cut on the energy $E_{e'}$ of the scattered positron. The lower limit on y is not determined by the acceptance of the DIS selection, but by the requirement that there should be a D^* in the central region of the detector.

5.3 Selection of D^* events

5.3.1 Reconstruction of the D^* Mesons

The average value for the probability that a charm quark fragments into a D^{*+} meson² has been determined to be [45]

$$f(c \rightarrow D^{*+}) = (0.235 \pm 0.007 \pm 0.007). \quad (5.9)$$

The D^{*+} meson consists of c and \bar{d} quarks and has a mass of $m(D^{*+}) = 2010.0 \pm 0.5 \text{ MeV}$. [46]

In this analysis the D^{*+} is reconstructed using the decay channel $D^{*+} \rightarrow D^0 \pi^+$ (see Table 5.3). As can be seen from Table 5.4 the mass difference between the D^{*+} and D^0 is just slightly larger than the pion mass, therefore the latter is produced with the very small momentum of 39 MeV in the rest frame of the D^{*+} . Due to its low momentum, the pion is referred to as *slow* pion π_{slow}^+ .

Many decay channels of the neutral D^0 meson are difficult to reconstruct due to their large particle multiplicity. In this analysis the decay $D^0 \rightarrow K^- \pi^+$ is used. It has a relatively small branching ratio (see table 5.3), however all D^{*+} decay particles are then charged and the multiplicity is with only three hadrons quite small. The whole decay chain which is used for the identification and reconstruction of the D^{*+} is shown below:

$$D^{*+} \rightarrow D^0 \pi_{slow}^+ \rightarrow (K^- \pi^+) \pi_{slow}^+ \quad (5.10)$$

²The charge conjugated state is always implied.

<i>Particle</i>	<i>Mass [MeV]</i>
D^{*+}	2010.0 ± 0.5
D^0	1864.6 ± 0.5
π^+	139.57018 ± 0.00035
$m(D^{*+}) - m(D^0)$	145.421 ± 0.010

Table 5.4: *The masses of the decay particles, used for the D^{*+} reconstruction in this thesis [46].*

<i>D* candidate selection</i>	
primary vertex track	
D^*	$p_t(D^*) \geq 2.0 \text{ GeV}$ $ \eta(D^*) < 1.5$ $\Delta m = m(K\pi\pi_s) - m(K\pi) < 167.5 \text{ MeV}$
D^0	$ m(K\pi) - m(D^0) < 80 \text{ MeV}$
K	$p_t > 500 \text{ MeV}$
π	$p_t > 300 \text{ MeV}$
π_s	$p_t > 120 \text{ MeV}$

Table 5.5: *Summary of the selection for the decay products of the D^* meson and for the D^* candidate.*

5.3.2 D^* Meson Selection

Tracks of the decay particles K , π and π_{slow} are reconstructed in the *Central Tracking Detector*, namely in the *CJC*, *CIZ/COZ* and *CST* devices (see section 3.3). First of all, only tracks fitted to the primary vertex are accepted. Further, these tracks are combined in pairs, so that each pair has opposite charged components, where one track is assigned the pion and other the kaon mass. The mass of such $K\pi$ pairs should be consistent with the D^0 mass within the detector resolution. To form a D^* candidate one track oppositely charged to the kaon candidate is added, assuming the pion mass.

To be accepted, a D^* candidate has to have a transverse momentum $p_t(D^*) > 2 \text{ GeV}$ and has to lie within the interval $|\eta(D^*)| < 1.5$, where $\eta = -\ln \tan(\Theta/2)$ denotes the pseudo-rapidity. Additionally the mass difference $\Delta m = m(K\pi\pi_{slow}) - m(K\pi)$ cut is applied. The nominal mass difference Δm is equal to $145.421 \pm 0.010 \text{ MeV}$ [46].

To reject combinatorial background from low momentum tracks, additional cuts on the decay particles of the D^* are applied, which are given in the table 5.5, together with the other cuts.

A data sample, which is selected after applying all cuts, discussed in Section 5.2, and the cuts for the D^* candidate, is called *the inclusive DIS sample*. The Figure 5.2 shows the resulting mass difference $\Delta m = m(K\pi\pi_s) - m(K\pi)$ for the inclusive sample.

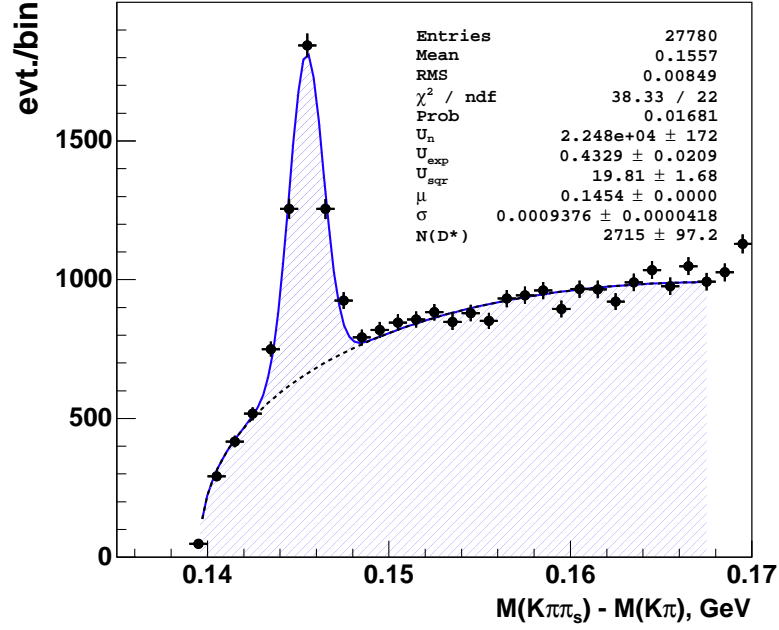


Figure 5.2: The mass difference Δm between the invariant masses of the D^* and D^0 candidates for the inclusive DIS sample after applying all cuts. Fit results are shown.

5.3.3 D^* Meson Fit Method

The number of D^* mesons in the inclusive DIS sample is extracted from a fit to the mass difference distribution, given in Figure 5.2. The following function is fitted to the data:

$$f(\Delta m) = \frac{N(D^*)}{\sqrt{2\pi} \sigma} \exp\left(-\frac{(\Delta m - \mu)^2}{2\sigma^2}\right) + \frac{u_n}{N_{\text{norm}}} \cdot (\Delta m - m_\pi)^{u_e} \cdot \left(1 - u_s \cdot (\Delta m)^2\right) \quad (5.11)$$

The function is the sum of a Gaussian for the signal and a background term, where

- $N(D^*)$ represents the number of D^* mesons,
- σ^2 is the variance of the signal,
- μ is the mean of the signal,
- u_n gives the normalisation factor,
- u_s is used in a quadratic correction term,
- u_e is a free parameter of the fit.

The fit is performed as a Likelihood-fit in the range $m_\pi < \Delta m < 167.5$ MeV. The fit method which is used in this analysis is originally described in [47], where more precise information concerning the fit parameters can be found.

After the selection cuts for diffractive events (discussed in section 6) difficulties in the fitting procedure due to low statistics appeared. In order to still get a reasonable fit results for low statistic data sets, the width and the mean of the signal are fixed to the values obtained for *the reference distribution* given in the Figure 5.2.

Chapter 6

Selection of Diffractive Events

In the H1 experiment, two methods are available for the selection of diffractive events.

The first method uses the Forward Proton Spectrometer (FPS) to detect the elastically scattered proton. The second one makes use of the observation, that events produced diffractively have two distinct systems X and Y in the hadronic final state, see Figure 6.1. System Y is produced by the elastic or dissociated proton and system X is produced by photon dissociation. These two systems are separated by a region in pseudo-rapidity in which no hadronic activity is detected. This is the result of the absence of any color connections between the photon and the proton fragmentation regions. This property can be used to select diffractive events experimentally. Because of its characteristic this method is called *rapidity gap method*. The latter method is used in this analysis.

Figure 6.2 shows a typical example of diffractive and non-diffractive events in the H1 detector. In the forward direction there are several detectors (see Section 3.5) which can be used to detect energy flow from particles originating from the proton remnant, which are produced in secondary interactions with the beam pipe and collimators.

As the outgoing proton is not detected, the cross sections presented in the following chapter are determined for the kinematic region $M_Y < 1.6 \text{ GeV}$ and $|t| < 1 \text{ GeV}^2$.

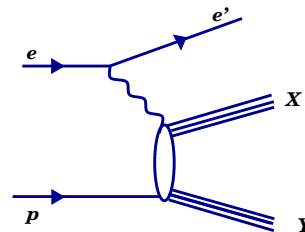


Figure 6.1: Diagram of the photon system X and the proton system Y in a diffractive event

6.1 Selection of Diffractive Events using Forward Detectors

The Liquid Argon Calorimeter, the Plug Calorimeter, the Forward Muon Detector and the Proton Remnant Tagger (see Sections 3.4 and 3.5) are sensitive to secondary particles resulting from proton dissociation decay products interacting with the beampipe. These forward sub-detectors are used for the selection of diffractive events in this analysis. The absence of signals in the detector components is required. Cuts in the LAr and in the Plug calorimeters, in the FMD and the PRT detectors are applied in order to eliminate non-diffractive events. After applying all cuts, which are presented below, the diffractive sample includes about 900 events.

However, it is possible that genuine diffractive events are rejected, because signals are produced in these detectors by electronic noise or beam backgrounds. It is important

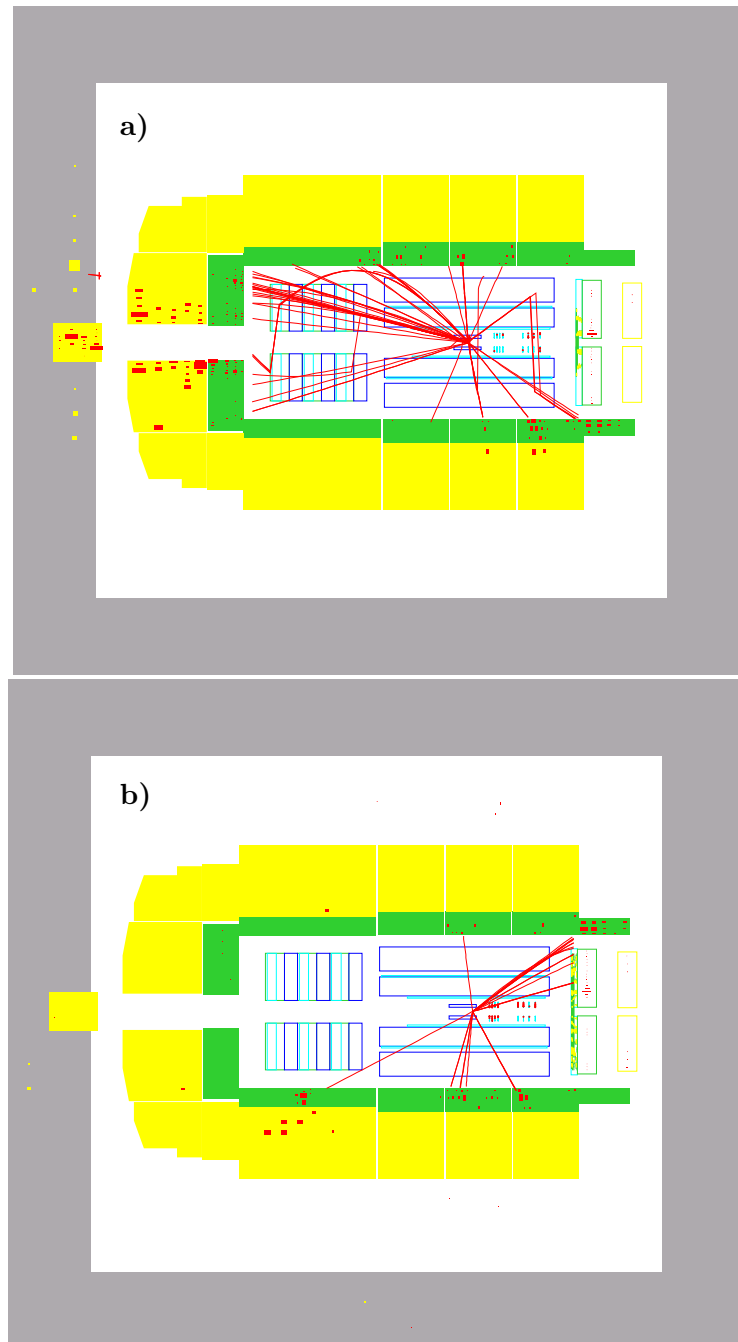


Figure 6.2: *The event-display of H1 detector with a non-diffractive (a) and diffractive (b) events. In the diffractive case very little activity in the forward region can be seen, there is a large rapidity gap in the outgoing proton direction. In contrast, (a) shows significant activity in the forward direction.*

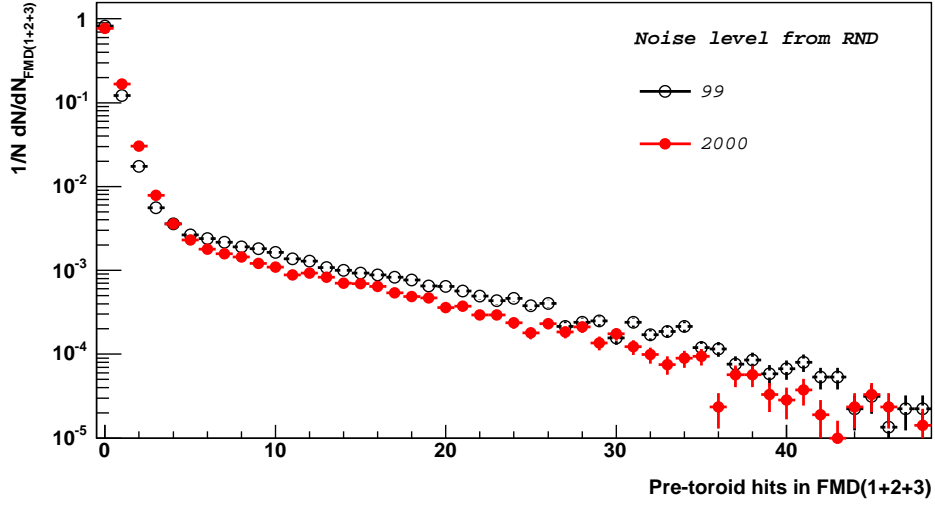


Figure 6.3: The noise level in the pre-toroid layers of the Forward Muon Detector for the data samples 1999 (open circles) and 2000 (closed circles), determined using random trigger events. The distributions are normalised to the number of events in the noise sample.

to correct for these losses. For investigation of background effects, the *Random Trigger events* (RND) are used. These events are taken without a physics trigger during data taking and provide information about the electronic noise level in the detectors. In this analysis variations of the noise level are studied run by run. The uncertainty for these corrections have to be estimated and included in the final measurement. For this purpose the Monte Carlo simulations should describe noise effects in the data correctly.

In the LAr calorimeter the noise effects are taken into account by implementing measured random events directly into the detector simulations.

The noise in the Plug and the Forward Muon Detector is not included in the standard detector simulation. Figure 6.4 presents the comparison of the data and the Monte Carlo simulation distributions for the energy deposited in the Plug calorimeter and the hits registered in the pre-toroid FMD layers. The detector simulations are shown without any noise corrections.

In the following, details of a study of noise effects in these sub-detectors and the procedure of the Monte Carlo correction are presented.

In the PRT two of seven scintillators are excluded from the usage in the diffractive selection due to the high noise level (see Section 6.5), in the other five scintillators of the Proton Remnant Tagger the noise level is found to be insignificant.

Figure 6.3 shows the residual noise level for hit pairs in the pre-toroid layers of the FMD, obtained from random trigger files. The noise level has a very similar shape in the two years, therefore the two years will not be distinguished later.

6.1.1 Noise Treatment in the Monte Carlo Simulations

Owing to the absence of the electronic noise implementation in the standard Monte Carlo simulations, the noise effects, which are present in the Plug and FMD, have to be treated manually. At first, the noise in these sub-detectors has to be determined separately and then added to the simulated value in the Plug or the FMD. Finally, the corrected value of the deposited energy or registered hits in the case of Monte Carlo is :

$$N_{MC_{corr}} = N_{MC} + N_{NOISE}, \quad (6.1)$$

where N denotes the energy in the Plug or the number of the hits in the FMD. In this analysis, two different methods for the determination of the noise value, N_{NOISE} , were studied.

- **the "probability" method** is based on the information concerning the probability to find a noise event. This probability information about the hits in the pre-toroid FMD layer, or, the deposited cluster energy in the Plug, is extracted from a random trigger sample. According to this probability distribution, the potential noise value, N_{NOISE} of hits (or energy) is then determined and added to the hits (energy) in the MC simulation. In the Figure 6.5 the data are compared to the MC simulation, where the latter is corrected for the noise effects according to the "probability" method. Appendix B provides a more detailed description of this method.

This method was used in the analysis at first, when only noise effects in the FMD had to be corrected in the Monte Carlo simulations. However in the following the strategy to select diffractive events was changed and the Plug calorimeter was included in the selection for reasons of stability.

The above noise simulation scheme is not fully correct, because correlations of the Plug and the FMD are not taken into account. Also the correlations between the FMD layers are not properly simulated.

- **In the "event by event" method**, the noise is determined by the so called *event by event* scheme. In this case, the complete information of a noise event, taken from random trigger event files, is stored in a *noisebank*. An example of the possible structure of such a bank is shown in Table 6.1. The explicit statement of the stored information allows to consider correlations inside the Forward Muon Detector or between the Plug and the FMD detectors. Thus, for a noise event all useful parameters are stored in parallel. Since noise in the Liquid Argon Calorimeter is automatically implemented in the Monte Carlo simulation all information in the *noisebank* is stored after applying a selection cut in the Liquid Argon Calorimeter (see Section 6.2), in order to avoid double counting. The MC simulations which are shown in the Figure 6.6 are corrected for the electronic noise effects using the "event by event" method.

The *event by event* method is used in the following, and the Monte Carlo simulation of the Plug or the FMD detectors are corrected according to this method.

#	Run	Event	NPlug all clusters	NPlug 100+ clusters	NPlug 200+ clusters	NPlug 300+ clusters	NPlug 400+ clusters	NPlug 500+ clusters	EPlug all GeV	EPlug 100+ GeV	EPlug 200+ GeV	EPlug 300+ GeV	EPlug 400+ GeV	EPlug 500+ GeV	FMD [1] hits	FMD [2] hits	FMD [3] hits
1	259488	7	74	74	61	31	14	5	22.07	22.07	19.68	12.22	6.63	2.74	0	0	0
2	259488	14	27	27	21	3	1	0	6.58	6.58	5.49	1.11	0.47	0.	0	0	0
3	259488	63	37	37	27	3	0	0	8.76	8.76	6.96	1.02	0.	0.	0	0	0
4	259488	96	34	34	25	7	0	0	8.53	8.53	6.85	2.35	0.	0.	0	0	0
5	259488	158	15	15	9	2	0	0	3.35	3.35	2.31	0.62	0.	0.	0	0	0
.
.
.
528	259884	7459	0	0	0	0	0	0	0.	0.	0.	0.	0.	0.	0	0	0
529	259884	7695	1	1	1	0	0	0	0.23	0.23	0.23	0.	0.	0.	0	2	0
530	259884	7697	2	2	0	0	0	0	0.35	0.35	0.	0.	0.	0.	0	0	0
531	259884	7759	1	1	0	0	0	0	0.16	0.16	0.	0.	0.	0.	0	0	1
.
.
.
20042	277695	42448	1	1	0	0	0	0	0.17	0.17	0.	0.	0.	0.	0	0	0
20043	277695	42491	3	3	2	0	0	0	0.69	0.69	0.51	0.	0.	0.	0	0	0
20044	277695	42503	4	4	1	0	0	0	0.77	0.77	0.24	0.	0.	0.	0	0	0
20045	277695	42702	1	1	0	0	0	0	0.17	0.17	0.	0.	0.	0.	0	0	0
20046	277695	42819	1	1	0	0	0	0	0.2	0.2	0.	0.	0.	0.	0	0	0
20047	277695	43190	1	1	0	0	0	0	0.13	0.13	0.	0.	0.	0.	0	0	0
20048	277695	43257	1	1	0	0	0	0	0.17	0.17	0.	0.	0.	0.	0	0	0
20049	277695	43500	2	2	1	0	0	0	0.33	0.33	0.2	0.	0.	0.	0	0	0

Table 6.1: The table shows the organisation of the noise information in the random trigger file used for correction of Monte Carlo simulations in the “event per event” method. In such a kind of the storage the noise correlations existing between the Plug and the FMD can be easily taken into account; e.g. the information in the line number one has following meaning: in the 7th random trigger event of the run 259488 74 clusters in the Plug are registered; and only 5 clusters will be accepted, if the minimal energy of the clusters in the Plug has to be larger than 500 MeV. Then follow energies deposited in the Plug for different cluster energy cuts. The last three columns contain the number of hits in the pre-toroid FMD layers.

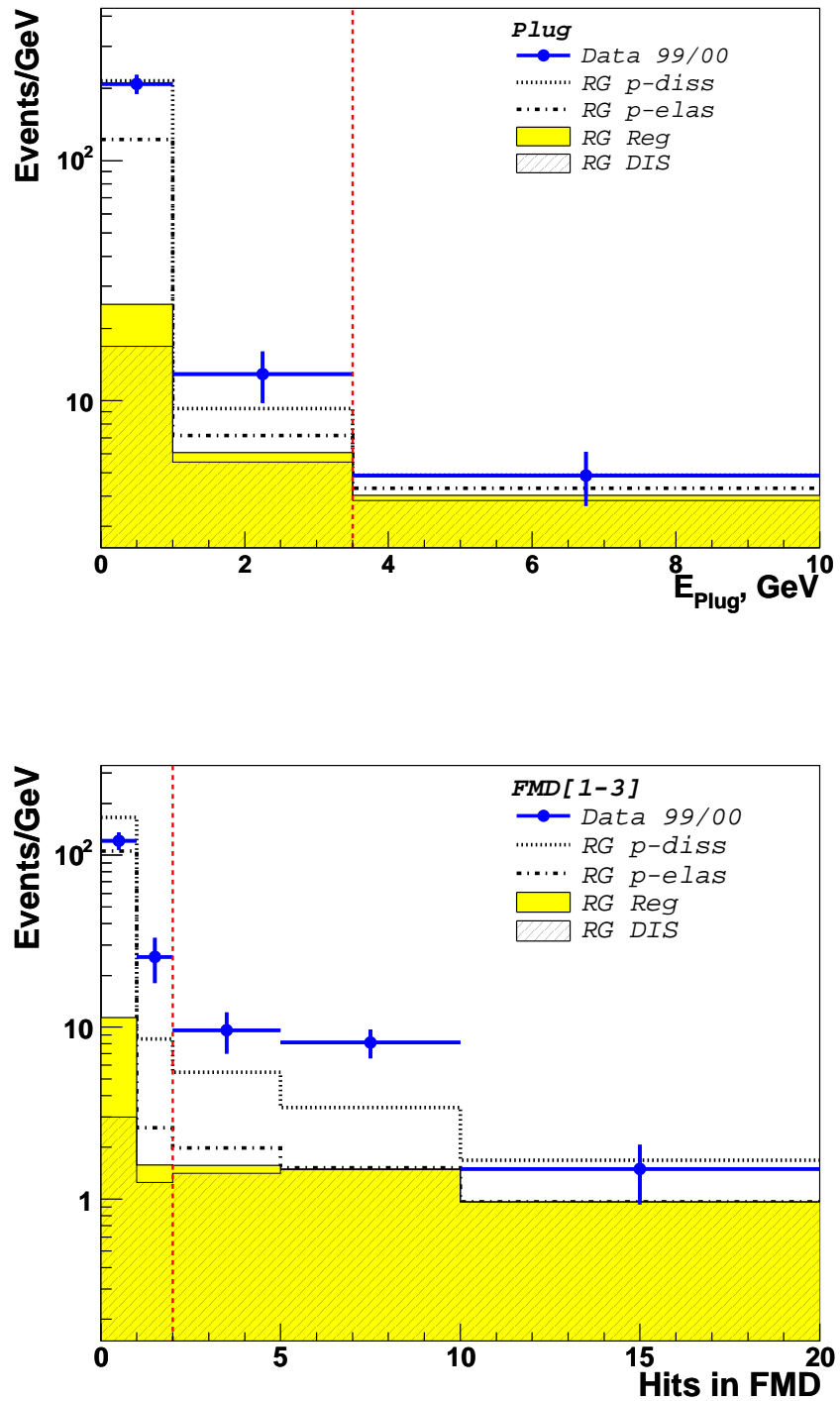


Figure 6.4: Data and simulation for the energy deposited in the Plug Calorimeter (on top) and number of hits in the pre-toroid FMD layers (bottom). The distributions for the simulated events are shown without any corrections.

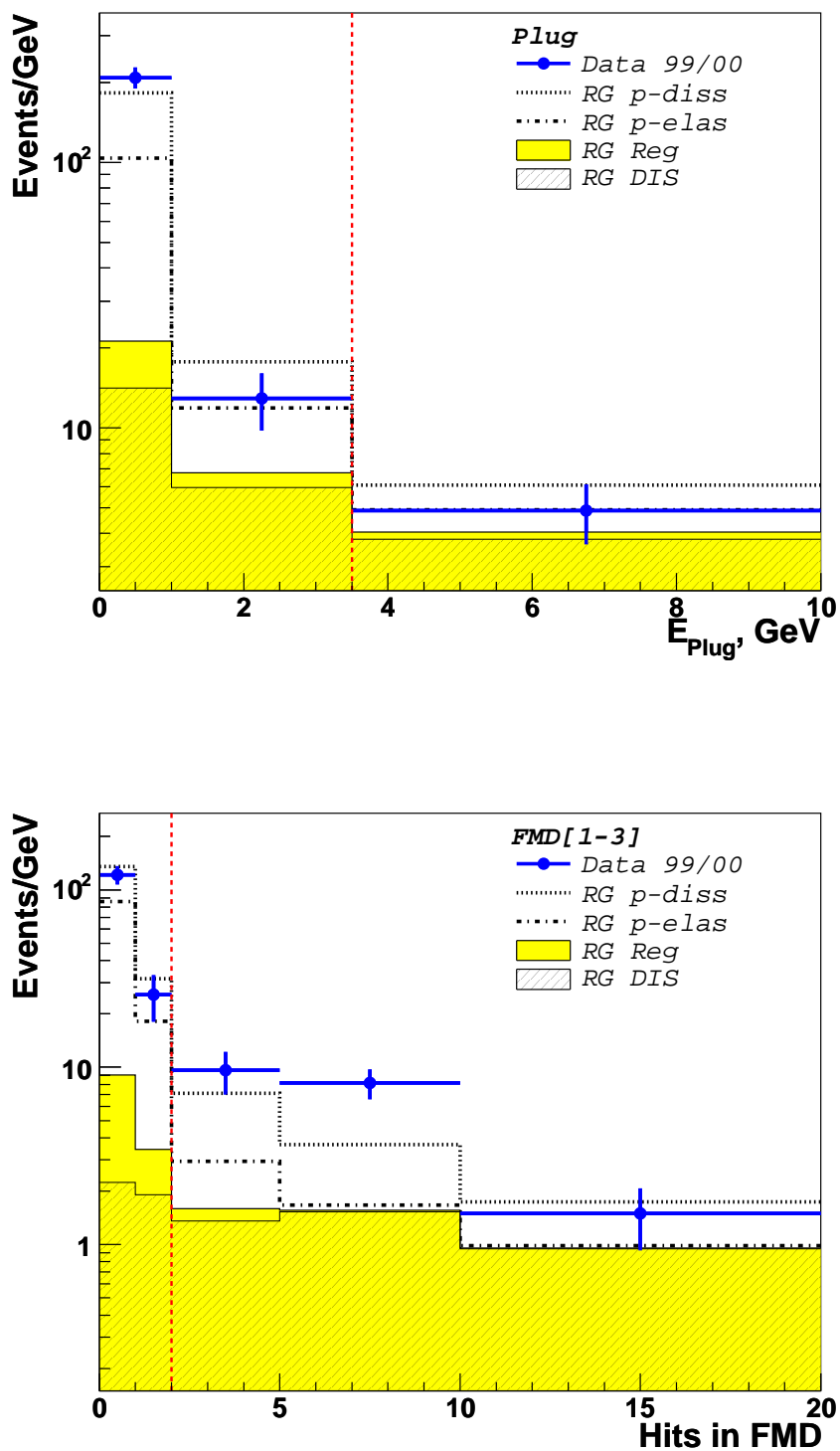


Figure 6.5: Data and simulation for the energy deposited in the Plug Calorimeter (on top) and number of hits in the pre-toroid FMD layers (bottom). Electronic noise is added to the Monte Carlo simulation according to the "probability" algorithm.

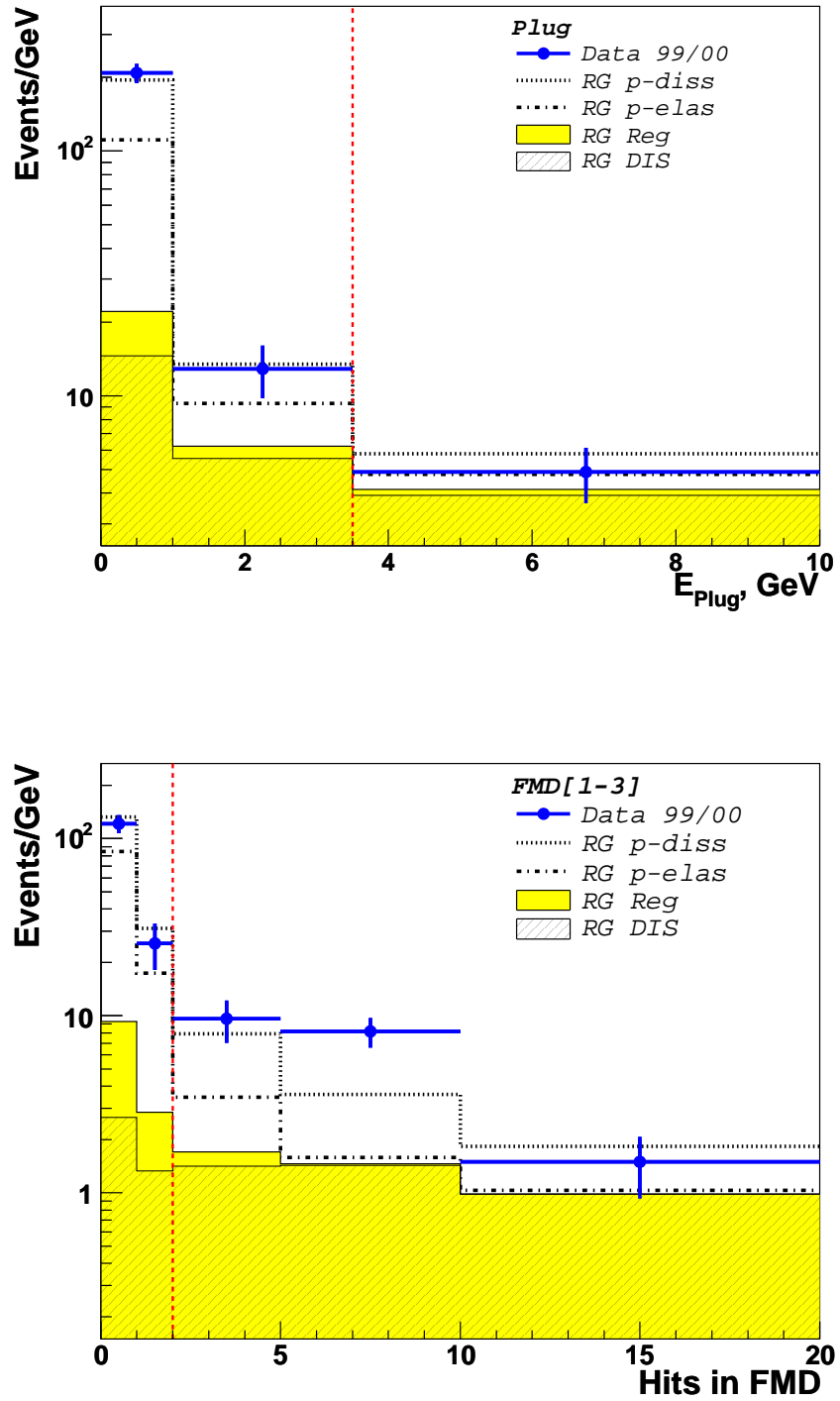


Figure 6.6: Data and simulation for the energy deposited in the Plug Calorimeter (on top) and number of hits in the pre-toroid FMD layers (bottom). Noise effects are taken into account in the Monte Carlo simulation according to the "event by event" method.

6.2 Energy Flow in the Liquid Argon Calorimeter

The LAr calorimeter covers the pseudorapidity range up to $\eta = 3.4$. The η_{max} quantity is defined as the pseudorapidity of the most forward energy cluster in the LAr above a specified noise threshold of 400 MeV. Clusters with smaller energy are considered as electronic noise.

Figure 6.7 shows the η_{max} distribution for the inclusive DIS D* data sample at detector level, which is compared to a simulation, performed by the Monte Carlo generator RAPGAP (RG). The simulation includes four components, which are added to each other in sequence of their application. The distributions for the following RAPGAP Monte Carlo models (see Section 4) are shown:

- 1st - inclusive deep inelastic scattering (RG DIS),
- 2nd - reggeon exchange (RG Reg),
- 3th - elastic proton (RG p-elas),
- 4th - dissociative proton (RG p-diss).

As shown in Figure 6.7 standard DIS events lie predominantly at larger values of η_{max} . The selection of diffractive events in this sub-detector is based on this fact. To select diffractive events the cut

$$(6.2)$$

$$\eta_{max} < 3.2 \quad (6.3)$$

in the LAr calorimeter is chosen, in order to reject the inclusive events effectively and at the same time to avoid the rejection of genuine diffractive events.

Inclusive DIS RG MC describes very well the right part of the data distribution (see Figure 6.7), but falls exponentially to the left of the η_{max} cut, and does not describe the full η_{max} spectrum. By adding the reggeon and the proton elastic component the discrepancy between the data and the simulation gets smaller, but also the combined MC sample underestimates the data distribution. Only by adding proton dissociation, one can get a reasonable description of the data.

6.3 The Plug Calorimeter

The Plug calorimeter extends the acceptance of the calorimetry system in the forward region beyond the end of the LAr calorimeter from pseudo-rapidity $\eta = 3.5$ to $\eta = 5$. In this analysis, the Plug is used to reject non-diffractive events with significant energy in the forward region.

The total energy deposited in the Plug is calculated by the sum of the cluster energies in this detector:

$$E_{Plug} = \sum_{clusters} E_{cluster} \quad (6.4)$$

Due to significant electronic noise, a cut on the energy for each cluster has to be applied. Figures 6.8 and 6.9 show distributions of the number of clusters in the Plug, $N_{cluster}$, and the total energy deposited in the Plug, E_{Plug} , after applying different $E_{cluster}$ cuts. One

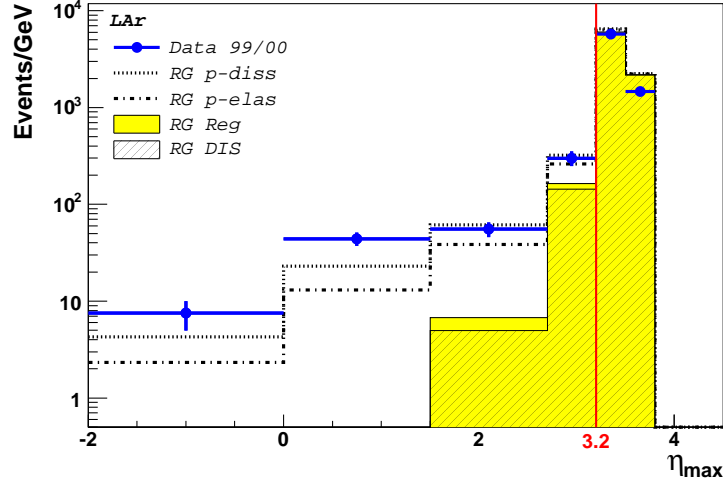


Figure 6.7: Energy flow distribution in the Liquid Argon calorimeter for the inclusive DIS D^* sample. The cut value for η_{max} is shown.

can see, that a better description of the data is reached by the simulation, if $E_{cluster}$ cuts of 400 or 500 MeV are applied.

Finally $E_{cluster} > 400$ MeV and $E_{Plug} < 3.5$ GeV are used for the selection of the diffractive events.

$$E_{Plug} < 3.5 \text{ GeV} \quad (E_{cluster} > 400 \text{ MeV}) \quad (6.5)$$

These cuts are chosen as a compromise between a good efficiency of this sub-detector for background and low rejection of diffractive events.

6.4 The Forward Muon Detector

The FMD covers the pseudorapidity range $1.9 < \eta < 3.7$. The FMD is designed to detect high-energy muons in the forward direction, but it is also sensitive to particle production with high pseudorapidities, for example particles produced due to secondary interactions from the proton remnant.

Only the three first FMD layers in front of the toroid magnet are used, the three post-toroid layers are located in the region of high synchrotron radiation coming from the positron direction, and are therefore not used.

A diffractive event candidate is selected in the FMD, if no more than two hit pairs in its first two layers and no more than two hit pairs in the third layer are found.

$$N_{FMD1} + N_{FMD2} < 2 \quad (6.6)$$

$$N_{FMD3} < 2 \quad (6.7)$$

Figure 6.10 shows the hit distributions in the pre-toroid FMD layers after applying the cuts on the LAr and Plug detectors (see Equations 6.2, 6.5).

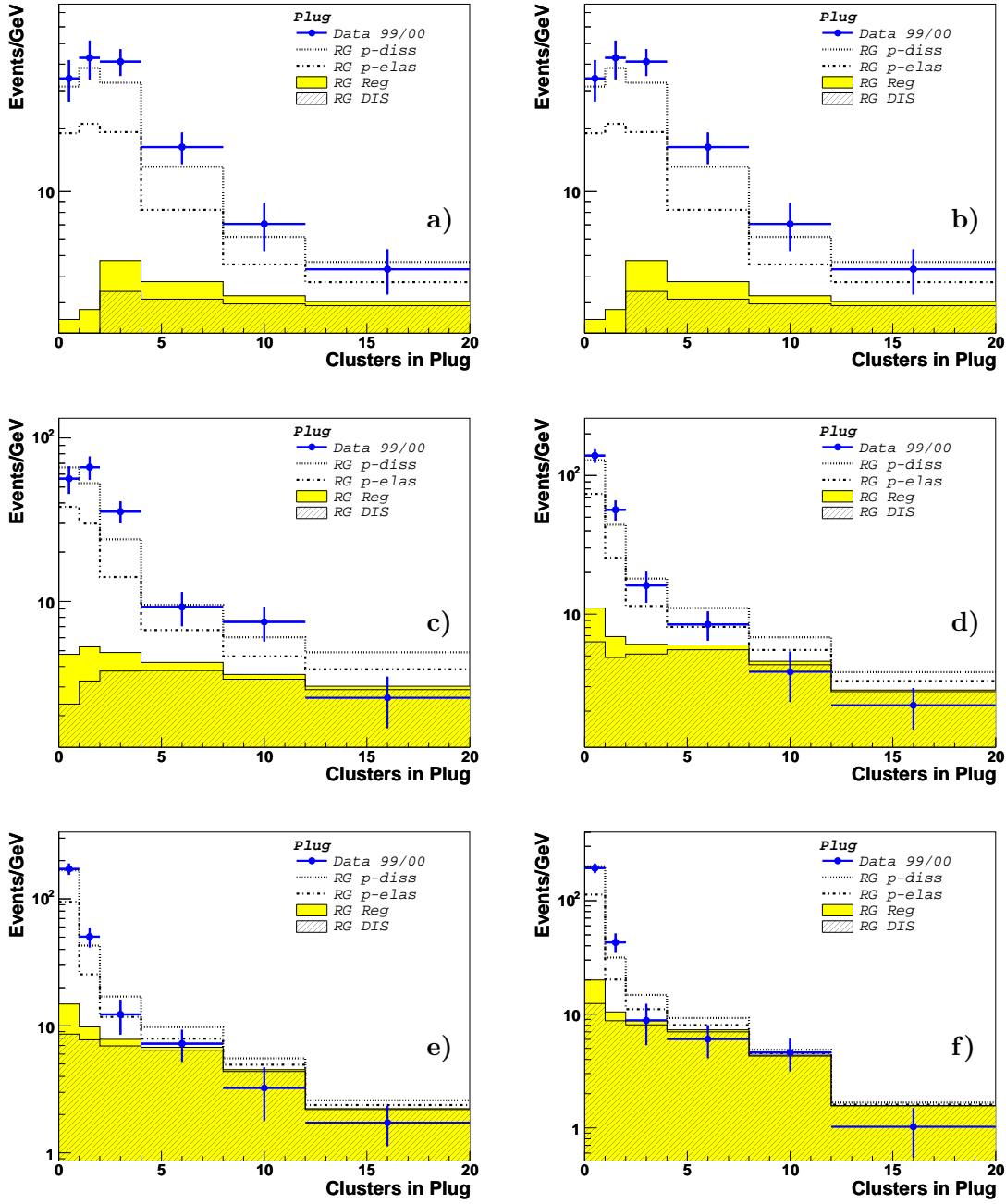


Figure 6.8: Number of clusters in the Plug calorimeter. Cut value of 400 MeV is used for the Ecluster in the final analysis.

- (a) without a cut on Ecluster
- (b) $E_{cluster} > 100$ MeV,
- (c) $E_{cluster} > 200$ MeV,
- (d) $E_{cluster} > 300$ MeV,
- (e) $E_{cluster} > 400$ MeV,
- (f) $E_{cluster} > 500$ MeV.

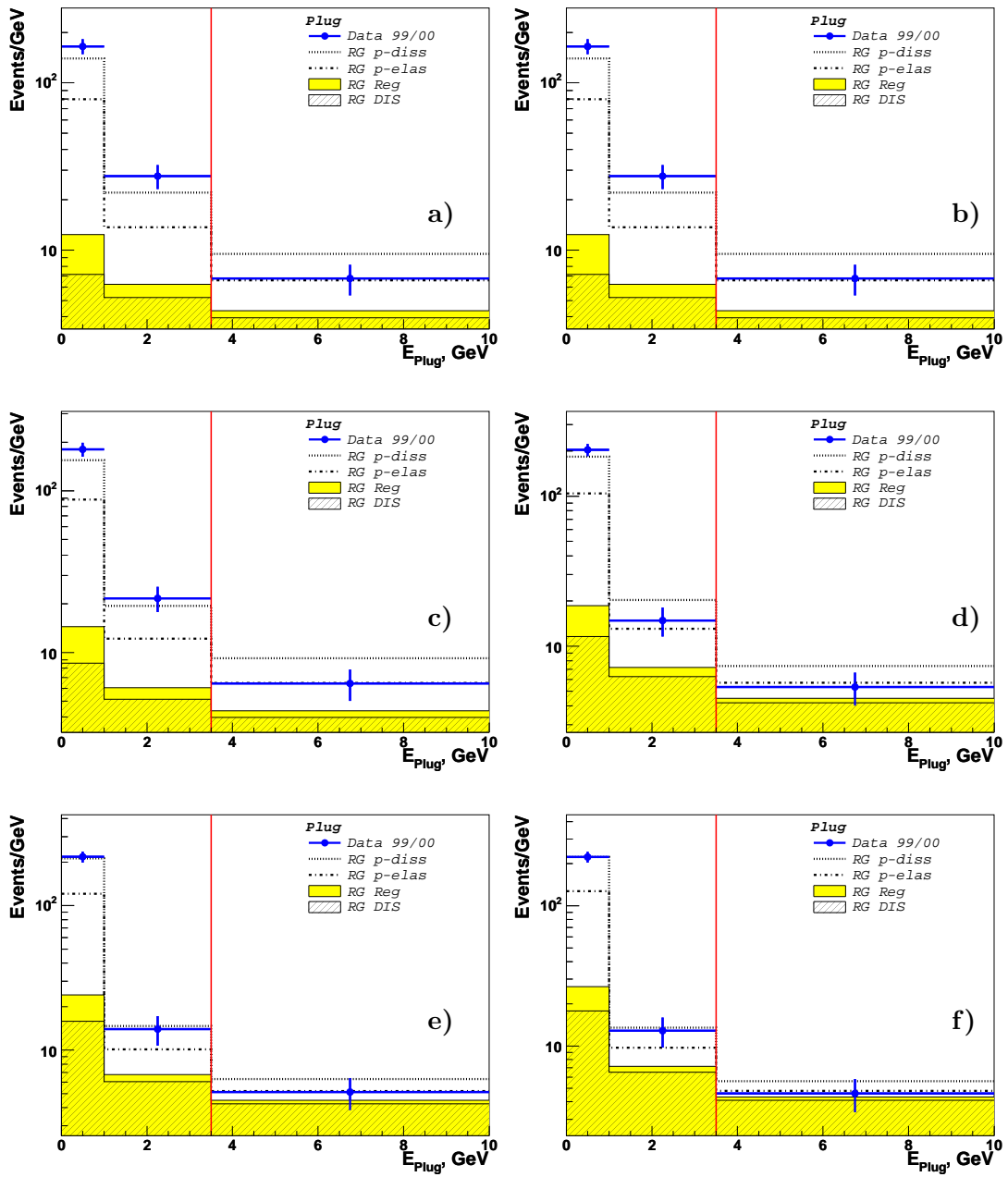


Figure 6.9: Energy deposited in the Plug. The final cut $E_{\text{plug}} < 3.5$ GeV is also shown as a straight line.

- (a) without a cut on E_{cluster}
- (b) $E_{\text{cluster}} > 100$ MeV,
- (c) $E_{\text{cluster}} > 200$ MeV,
- (d) $E_{\text{cluster}} > 300$ MeV,
- (e) $E_{\text{cluster}} > 400$ MeV,
- (f) $E_{\text{cluster}} > 500$ MeV.

Year	PRT scintillator				
	1	2	3	4	5
1999	0.53	0.61	0.74	0.36	0.54
2000	0.59	0.75	0.78	0.38	0.49
Combined for 1999/2000	0.56	0.70	0.75	0.37	0.50

Table 6.2: *The correction factors for the PRT detector.*

Time dependence of Random Noise

As was already mentioned in Section 6.1.1 the electronic noise in the Plug and FMD detectors is not implemented in the standard Monte Carlo simulations. The *event-by-event* method (see Section 6.1.1) is used in this analysis for the Monte Carlo correction. Here the time dependence of the random noise events used for this correction is studied. Figure 6.11 show a ratio R as a function of the run periods during 1999 and 2000. This value R represents the ratio of the selected simulated events, which are corrected for the noise effects to the pure simulated events without any correction. In both cases only events which fulfill the cut requirements are accepted.

In the right part of Figure 6.11 these ratios for the different run periods are presented in the x-projection.

6.5 The Proton Remnant Tagger

The Proton Remnant Tagger (PRT) (see Section 3.5) covers approximately the pseudo-rapidity interval $6.0 < \eta < 7.5$. The PRT was designed to veto events close to the outgoing proton beam. An event is rejected if any of the first five PRT scintillators shows a signal above the noise level.

$$N_{PRT[1-5]} = 0. \quad (6.8)$$

The noise in the PRT scintillators is studied, using information from the random trigger files. As can be seen in Figure 6.12, the sixth and the seventh scintillators are very noisy in the data taking period and are therefore not considered in this analysis. The first five PRT layers are also noisy in a few of runs. These runs are excluded individually. The noise level in the remaining PRT scintillators (see Section 3.5) is found to be acceptable.

The efficiencies of the PRT scintillators are vastly overestimated in the Monte Carlo simulations. This can be due to several reasons:

1. Aging effects of the scintillators, because they are situated close to the proton beam.
2. Possible incorrect predictions of the Monte Carlo models for the energy flow in the forward direction.
3. Incorrect description of the PRT in the H1 simulation.

Therefore corrections are applied to bring the simulations into agreement with the experimentally observed efficiencies of the PRT. At first, it is necessary to determine the actual

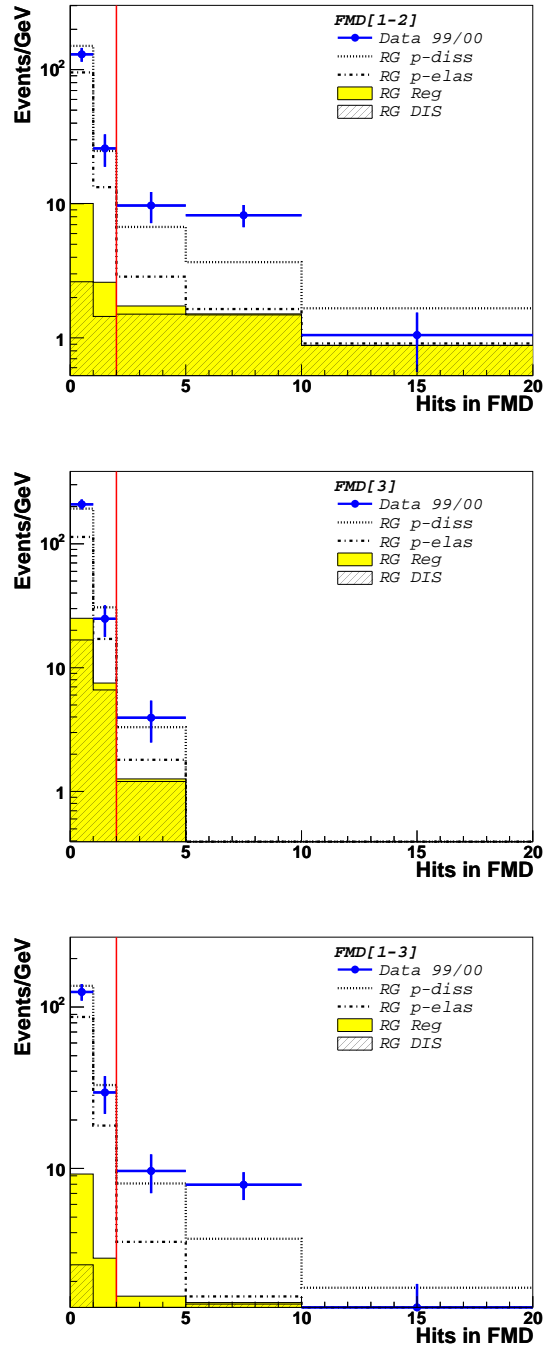


Figure 6.10: Hit distributions in the FMD after applying the cuts on the LAr and Plug detectors. Hits in the first two FMD layers, in the third layer and the sum of them is shown.

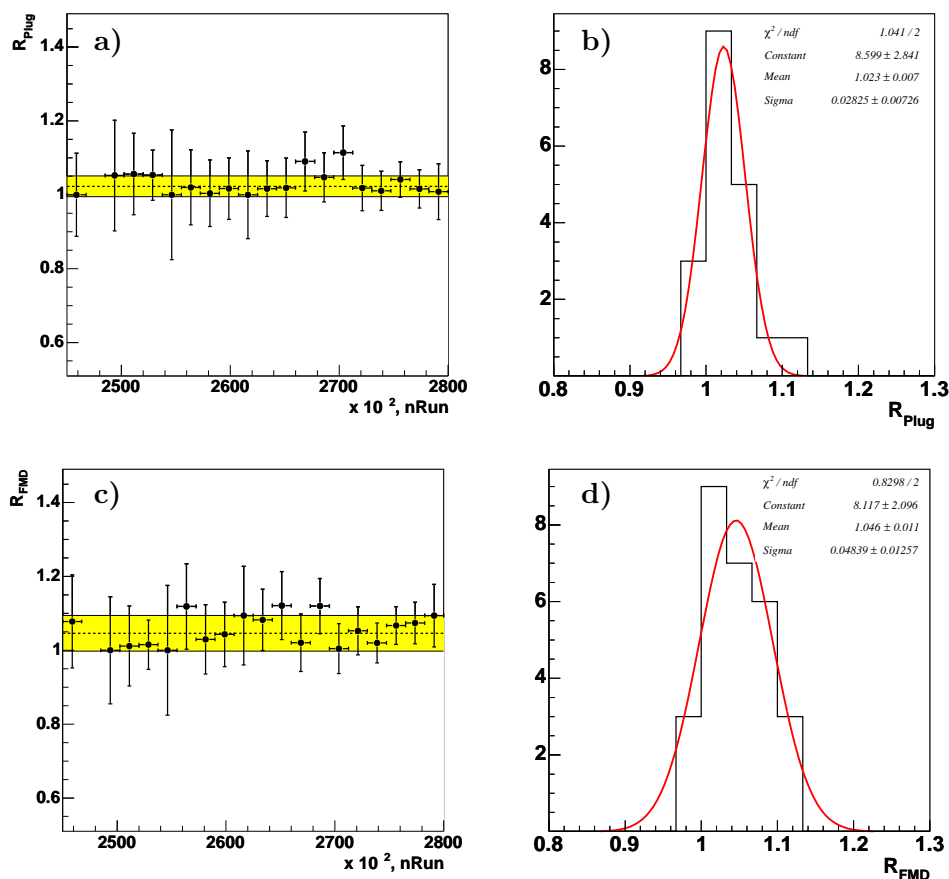


Figure 6.11: *a(c)* Ratio R of the simulated diffractive events in the Plug (FMD) detector corrected for noise effects to the simulated events without any corrections is shown as a function of run ranges. Only events selected after applying the η_{max} (and E_{Plug}) cuts are accepted for the determination of this ratio. The central lines (dashed) indicate the mean values of the ratio R extracted from the fits to the distribution of R , which are shown on the right hand side, see *b(d)*.

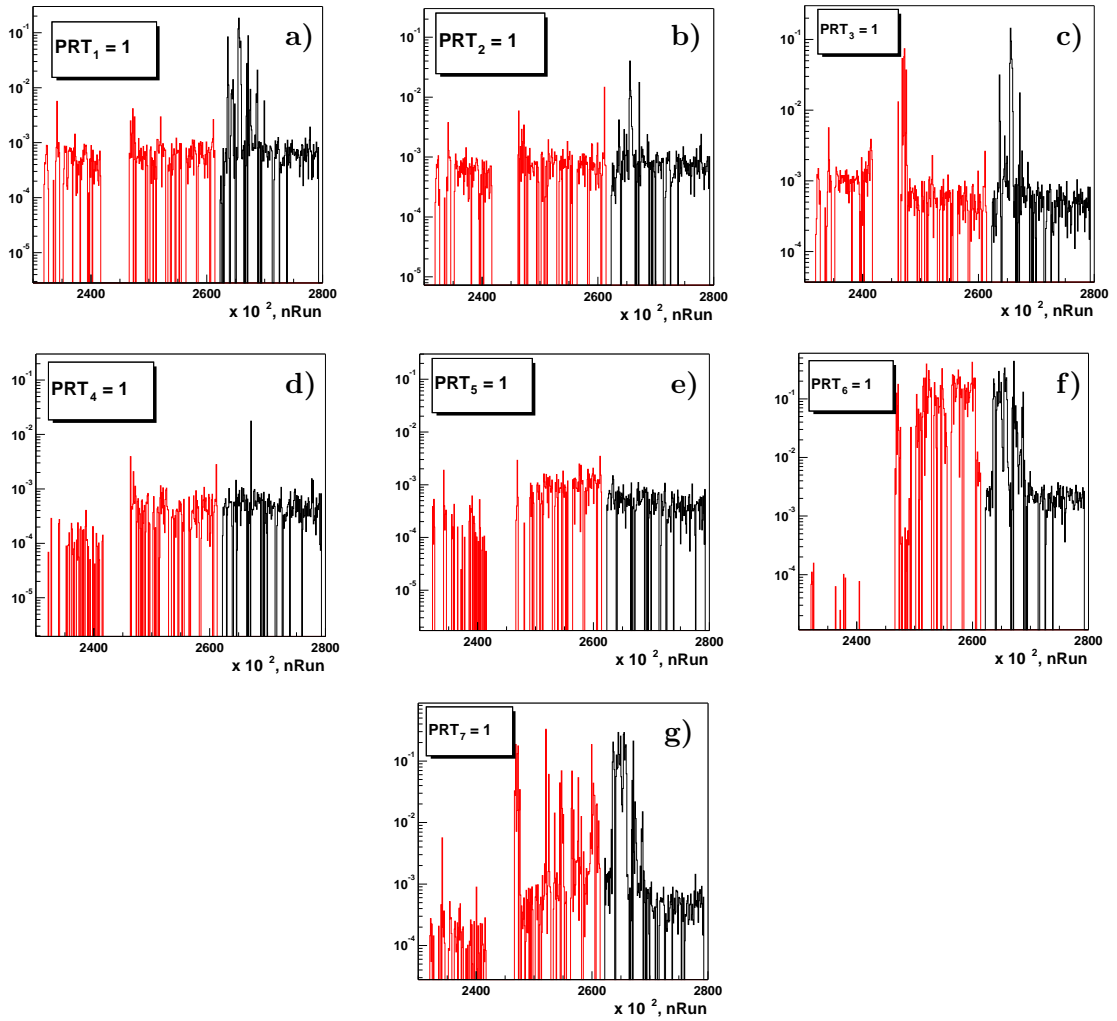


Figure 6.12: Noise from the random trigger files in the PRT 1(a) - 7(g). The fraction of random events with $\eta_{max} < 3.2$, $N_{FMD} < 2$ and $N_{PRT_i} > 0$ as a function of the run number is shown.

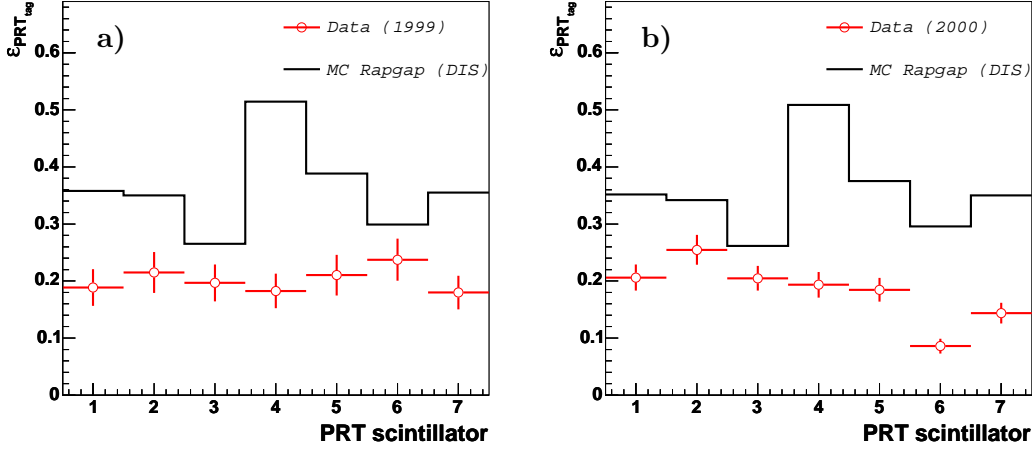


Figure 6.13: The individual efficiencies of the PRT scintillators for data (points) and inclusive Monte Carlo sample (solid line) separately for the 1999 and 2000 periods.

efficiency of each PRT scintillator for the data and simulation samples. The efficiencies for detecting events with activity in LAr and FMD by individual PRT scintillator are estimated as

$$\varepsilon_{PRT,i} = \frac{N_{PRT,i}}{N_{forw}}. \quad (6.9)$$

Anti-diffractive cuts on $\eta_{max} > 3.2$ and $N_{FMD} > 1$ are used to select the sample, the number of events is N_{forw} . The Figure 6.13 shows the efficiencies of the single PRT scintillators, obtained from the data and the inclusive DIS Monte Carlo sample.

These efficiencies contain the effects of the acceptance and of the actual hardware efficiency. It is necessary to take the difference between simulation and data into account in the further analysis.

In Table 6.2 the correction factors for the Monte Carlo simulation of the five scintillators used in this analysis are summarised. If these correction factors are applied to the simulation, the description of the data becomes significantly better. The distributions of the PRT hits before and after applying the correction factors is shown in figure 6.14 for diffractive D^* events.

In earlier H1 analyses of diffractive D^* and dijet production [48, 49] similar correction method of the PRT efficiencies was used. The original procedure of the PRT efficiency reweighting is taken from [48].

6.6 Reconstruction of the Kinematic Variables

The description of the diffractive DIS processes requires the reconstruction of the kinematic variables x_P , β and M_X (see Section 2.6).

The hadronic final-state system X is observed in the main detector components. M_X is calculated from the four-momentum of this system and reconstructed from the clusters

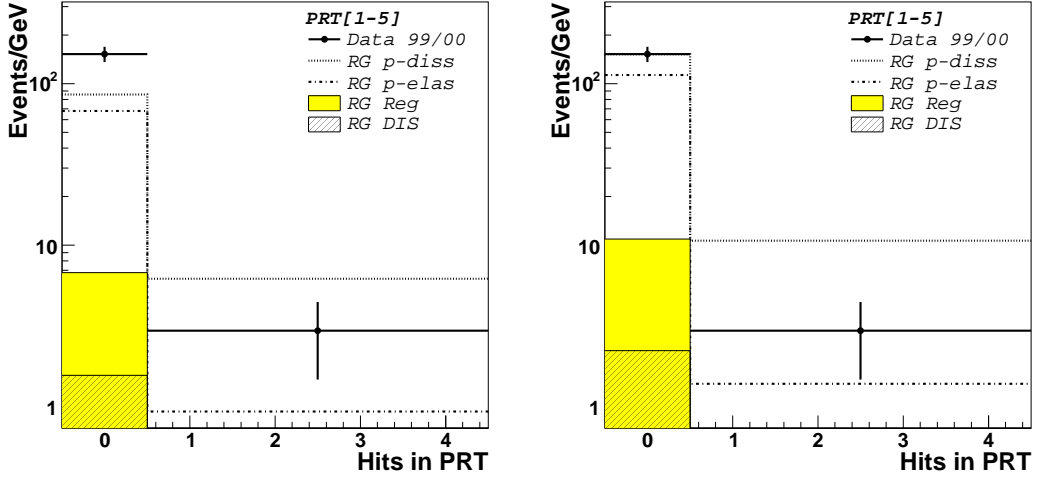


Figure 6.14: The PRT hit distributions after applying cuts on η_{max} , E_{Plug} and N_{FMD} . On the left side without correction factors and on the right side after applying the correction for the PRT in Monte Carlo simulation.

in the LAr and the SpaCal calorimeters as

$$M_X^2 = \left(\sum_i E_i \right)^2 - \left(\sum_i p_{x,i} \right)^2 - \left(\sum_i p_{y,i} \right)^2 - \left(\sum_i p_{z,i} \right)^2. \quad (6.10)$$

It is found, that the reconstructed M_X value underestimates the true M_X . This is shown in Figure 6.15, which presents the ratio of generated and reconstructed M_X -values

$$\delta M_X^{rec} = \frac{M_X^{gen}}{M_X^{rec}} \quad (6.11)$$

fitted by a linear function. For the Monte Carlo simulations and the data a corresponding correction factor is applied in order to improve the reconstruction of the M_X variable.

The variable M_X is used for the reconstruction of x_P and β . Figure 6.16 presents the quality of the reconstruction for these variables. The shaded histograms show the resolutions before the M_X -correction, and the full histograms after the correction for the mass of the system X .

The forward detector cuts restrict the x_P region, however after applying the forward cuts, the events have still x_P values up to 0.15. In order to reject non-diffractive events and ensure that the measured cross-sections are dominated by diffractive exchange, the following cut

$$x_P < 0.04 \quad (6.12)$$

is applied in addition. Figure 6.17 shows the distributions for the x_P , M_X and β variables after applying all forward detector cuts. The cut for x_P is also indicated.

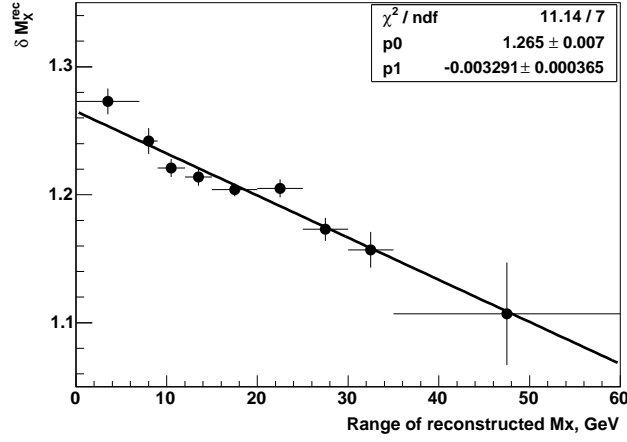


Figure 6.15: The quantity $\delta M_X^{\text{rec}} = M_X^{\text{gen}} / M_X^{\text{rec}}$ as a function of the reconstructed mass of the final-state system X is fitted with a linear function.

6.7 Summary of the Selection of Diffractive D^* Mesons

Table 6.3 summarises the cuts which are applied for the diffractive D^* event selection and Figure 6.18 shows graphically the D^* signal resulting from this selection.

The number of diffractively produced D^* mesons after applying all required cuts is $N(D^*) = 133 \pm 17$ and it is extracted from the fit to the Δm distribution as described in section 5.3.3.

<i>Diffractive cuts</i>
$\eta_{\text{max}} < 3.2$
$E_{\text{Plug}} < 3.5 \text{ GeV}$
$N_{\text{FMD1}} + N_{\text{FMD2}} < 2$
$N_{\text{FMD3}} < 2$
$N_{\text{PRT}} = 0$
$x_{\text{P}} < 0.04$

Table 6.3: Cuts of the diffractive selection are shown in sequence of their discussion.

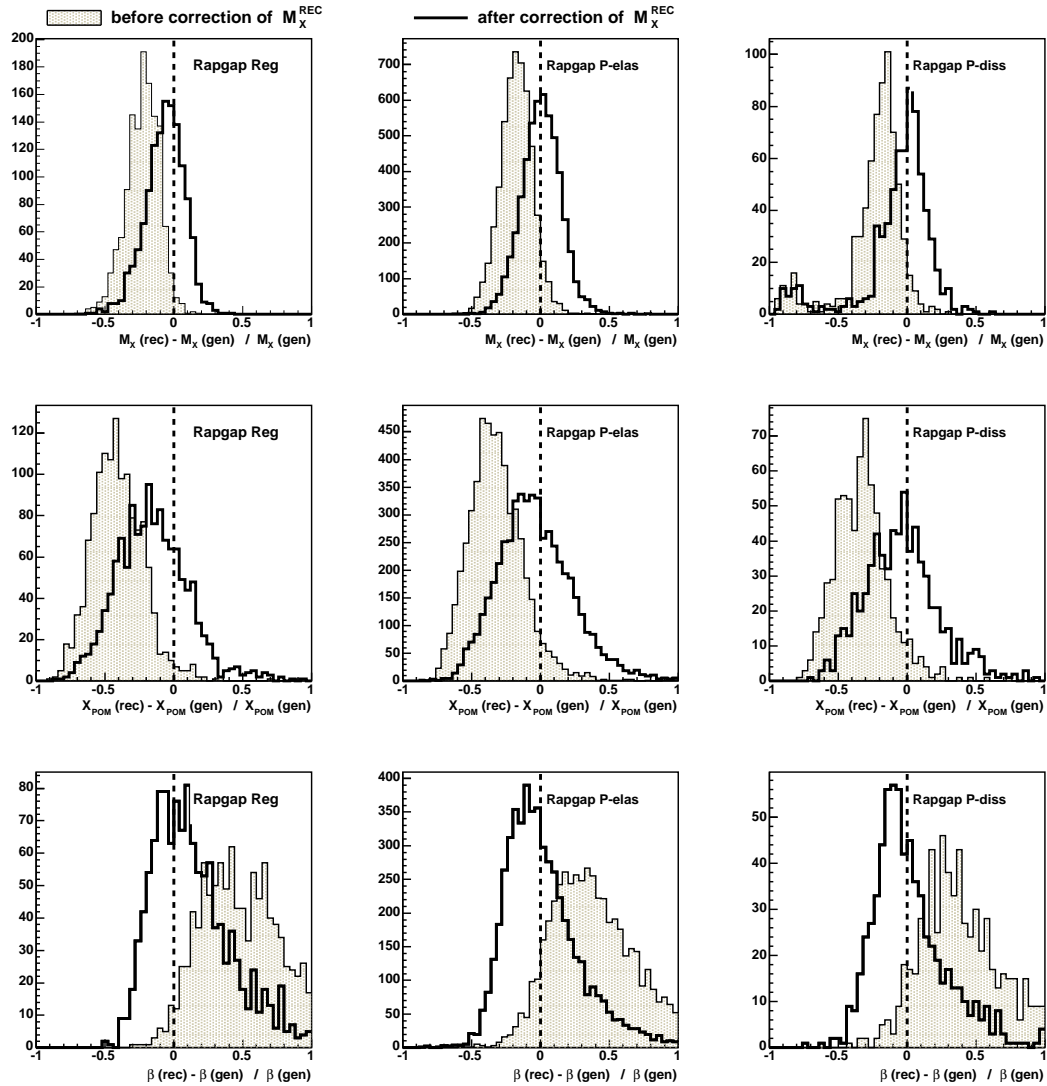


Figure 6.16: Correlations between the generated and the reconstructed variables M_X (top), x_P (middle) and β (bottom), using the RAPGAP Monte Carlo, separately for proton dissociation (right), for proton elastic (center), and reggeon exchange (left). The solid histograms are obtained with the M_X corrections, the shaded histograms without.

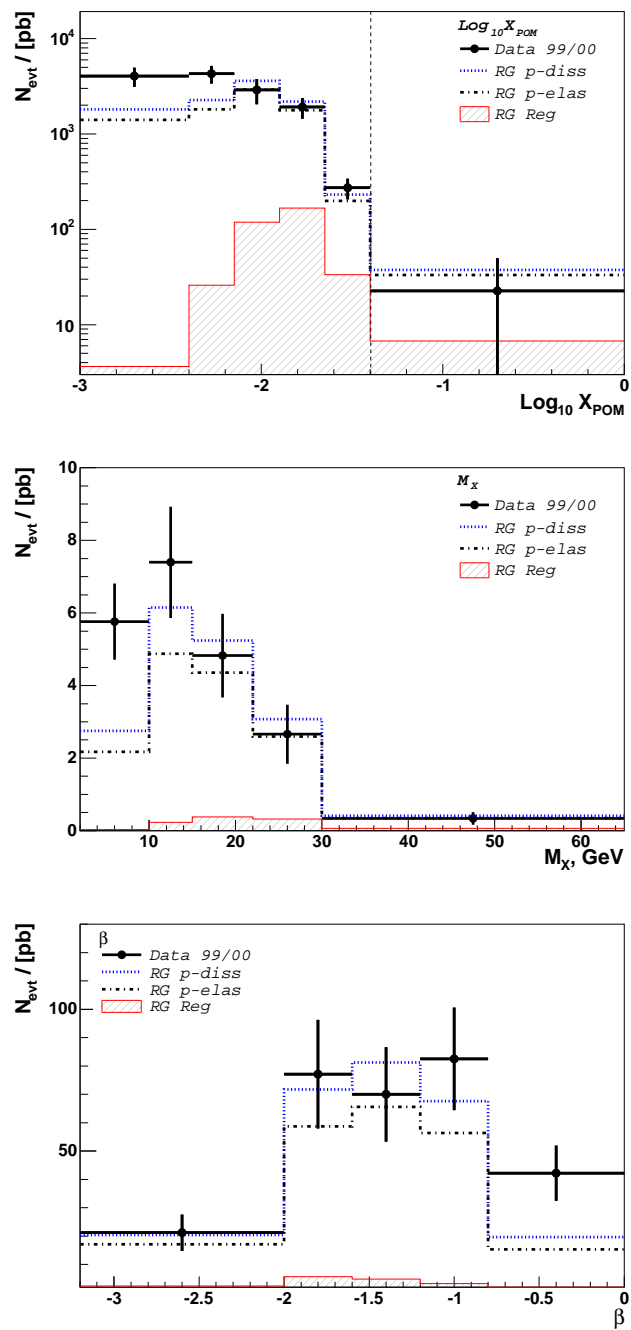


Figure 6.17: Distributions for $\log x_P$, M_X and β after applying all forward detector cuts. The cut value for x_P is shown.

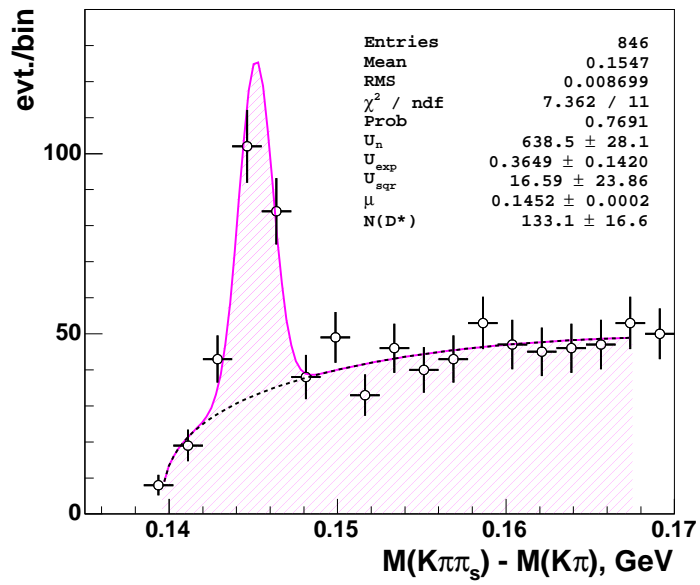


Figure 6.18: The mass difference Δm between the invariant masses of the D^* and D^0 candidates after applying all diffractive cuts.

Chapter 7

Cross Section Measurement

In this section the measurement of the total diffractive cross section $\sigma(ep \rightarrow e'(D^*X)Y)$ is presented. This result is compared with the measured total inclusive cross section. The measurements are presented differentially as a function of kinematic variables.

7.1 Determination of the Cross Section

The visible diffractive cross section of D^* meson production, which is defined in a given kinematical region, can be calculated from

$$\sigma(ep \rightarrow e'(D^*X)Y) = \frac{N(D^*)}{\epsilon \cdot \mathcal{L}_{int} \cdot \mathcal{BR}(D^* \rightarrow K\pi\pi_s)} \cdot C_{diss}. \quad (7.1)$$

here

$N(D^*)$ represents the number of D^* mesons obtained from the fit to the ΔM distribution (see Section 5.3.3). These events pass the DIS and diffractive selection cuts.

$\epsilon = \epsilon_{rec} \cdot \epsilon_{trigger}$ is the product of the efficiencies of the reconstruction, triggering and the acceptance of the detector.

\mathcal{L}_{int} is the integrated luminosity after correction for trigger prescales.

$\mathcal{BR}(D^* \rightarrow K\pi\pi_s)$ is the branching ratio of the analysed D^* decay chain.

C_{diss} is a correction due to smearing of events across the $M_Y = 1.6$ GeV border.

In order to obtain the differential cross sections, the number of diffractive D^* mesons in each bin is obtained from the ΔM distribution formed within the kinematic limits of that bin. The reconstruction and trigger efficiencies are calculated as a function of the differential variable. Finally, the cross section in each bin is divided by the width of the bin.

7.1.1 Trigger Efficiency

The selected events used for the cross section measurement are triggered on the first trigger level L1 by subtrigger S61 . The definition of the subtrigger S61 is presented in Section 5.1

Because the trigger used in this analysis is not 100 % efficient and rejects some good ep events, it is important to define inefficiencies of the used trigger elements. The trigger efficiency ε_{tr} can be obtained in the following ways :

- For **the Monte Carlo simulation**, the total amount of the D^* events before the triggering, D_{all}^* , is well known, in this case the efficiency is determined as the ratio of the reconstructed and triggered D^* to the number of all reconstructed D^* events. The combinatorial background is found negligible in the Monte Carlo simulation, therefore in order to avoid possible fluctuations from the D^* fit procedure, all events with a reconstructed D^* -candidate with mass difference $143 < \Delta m < 148$ MeV are considered.

$$\varepsilon_{tr}|_{MC} = \frac{N(D_{subtrigger}^*)}{N(D_{all}^*)}. \quad (7.2)$$

- The extraction of the trigger efficiency directly **from the data** is more subtle. As introduced in Section 5.1 subtrigger S61 consists of a number of trigger elements (TE). For the trigger efficiency measurements an independent subtrigger of the S61 is required (so called *monitor trigger*). However, there is no subtrigger completely independent of the subtrigger S61. Therefore the trigger efficiency is calculated for each trigger element individually as ratio of the number of D^* mesons triggered by both the trigger element from subtrigger S61 and the independent subtrigger to the number of D^* events with a positive monitor trigger decision only :

$$\varepsilon_{tr}|_{Data} = \frac{N(D_{TE \& \text{monitor}}^*)}{N(D_{monitor}^*)}. \quad (7.3)$$

One of the components in the subtrigger S61 is the inclusive electron trigger (IET). Its trigger elements are sensitive to the electron in the SpaCal calorimeter with energy above 6 GeV. The used analysis cut on the energy of the scattered positron is equal 8 GeV, therefore the efficiency of the IET is expected to be 100 %.

The trigger elements DCRPh_THig, zVtx_sig and the subtrigger S0¹ have not common trigger elements, therefore the subtrigger S0 is used as independent *monitor trigger*. Figure 7.1 shows the efficiencies of the individual conditions DCRPh_THig (a), zVtx_sig (b) and the combination of both as a function of $p_t(D^*)$ for the selected inclusive sample. The simulation gives a good description of the efficiency of the trigger elements, although the Monte Carlo simulation slightly underestimates the DCRPh_THig trigger element.

Table 7.1 summarises the efficiencies of the individual and combined trigger elements of the subtrigger S61 for the data and simulation samples. Since the Monte Carlo sample has much higher statistics its efficiencies are used to correct the data. An uncertainty of the trigger efficiency of 3% is estimated as the maximum difference between the data and simulation.

¹The definition of subtrigger S0 is:

```
(SPCLe_IET>2) && (!VETO_inner_BG && !VETO_Outer_BG && !VLQToF_BG)&&(((FTToF_IA || FIT_IA) ||
(!FTToF_BG && !FIT_BG)) && (PToF_IA ||!PToF_IA))
```

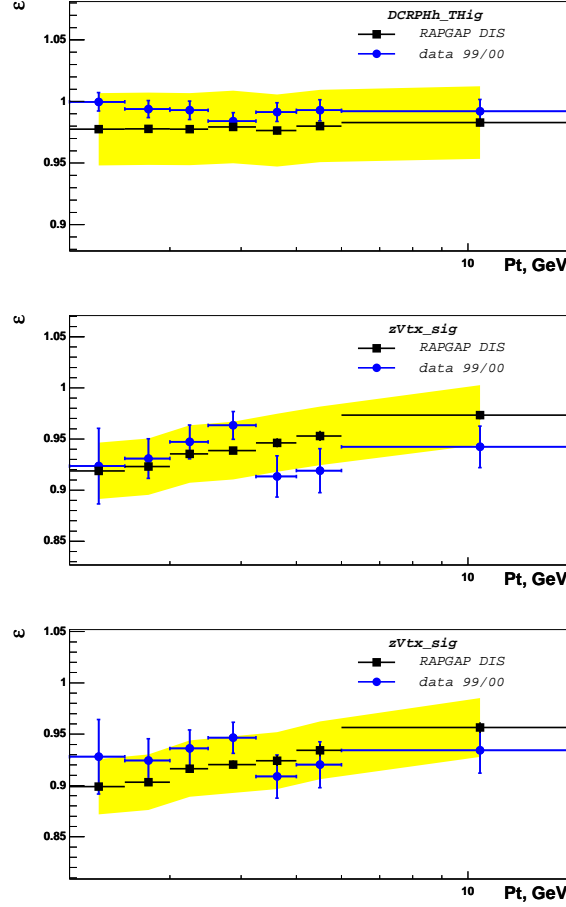


Figure 7.1: Trigger efficiency for the elements of the subtrigger S61 as a function of the D^* -meson transverse momentum. The uncertainty of 3% is shown by the yellow (grey) band.

7.1.2 Geometric Acceptance and Efficiency of Detectors

In a real measurement, which is performed with a real detector, where efficiencies and geometric acceptances unfortunately are not ideal, several effects need to be corrected. For that purpose Monte Carlo information from the generated level, where an event consists of four-vectors is compared with Monte Carlo events from the reconstructed level, which are equivalent to the events in the real measured data and also passed through analysis selection cuts.

However, this only works if the MC simulation describes all detector effects well. If deficiencies are found in the simulation, i.e. a sub-detector is not modelled correctly, the simulation is corrected according to the data in order to obtain a better description. The remaining differences which can still be present between data and Monte Carlo simulation are taken into account by systematic errors.

In this analysis the reconstruction efficiency accounts for event losses due to the inefficiencies of the sub-detectors used in the event selection and detector geometric acceptance.

This correction quantifies the number of events reconstructed in the studied kinematic region compared to the true number of events generated in the same kinematic region and is defined as

$$\varepsilon_{rec} = \frac{N(D_{rec}^*)}{N(D_{gen}^*)}. \quad (7.4)$$

$N(D_{gen}^*)$ corresponds to the number of generated D^* events in a phase space for deep inelastic scattering, (i.e. after hadronisation) which is defined solely by the kinematic variables Q^2 and y (see Section 5.2). No detector related cuts, e.g. on the scattered positron, are made at the hadron level. The phase space for diffractive events is given in terms of the kinematic variables x_P , M_Y and $|t|$.

$N(D_{rec}^*)$ is the number of reconstructed Monte Carlo events with D^* , which are reconstructed in the visible kinematic range after passing through the detector simulation and all selection criteria.

The simulation of the forward detectors reflects critically on the reconstruction efficiency and as a consequence on the diffractive cross section measurements. Non simulated electronic noise effects in the Plug or FMD detectors, which are used in the selection chain of diffractive events, need to be remedied. Noise is studied using random triggered files and added to the simulated events on the event-by-event basis (a full description of this method was given in Section 6.1.1). The noise corrections taken into account in this way affect the reconstruction efficiency.

The efficiency of the PRT in the Monte Carlo simulation is too high compared to that in data. For example, the efficiency of the fourth PRT scintillator with the condition $PRT > 0$ in the simulation is about 50 %, in data this quantity reaches value of 20 % only. To ensure the proper calculation of the acceptance, the poor description of the PRT detector efficiency in the simulation needs to be corrected, the algorithm of this correction was presented in Section 6.5.

For the measurement of the differential cross sections the efficiency is calculated bin-wise.

The efficiency of the inclusive event selection is shown in Figure 7.2 as a function of the different kinematical variables. Figure 7.6 shows the reconstruction efficiency for the kinematic variables of the diffractive cross-section.

7.2 Inclusive D^* Measurements

The inclusive D^* cross section in the kinematic region $2 < Q^2 < 100$ GeV, $0.05 < y < 0.7$, $p_t(D^*) > 2$ and $|\eta(D^*)| < 1.5$ is measured according to Equation 7.1 and found to be

$$\sigma(ep \rightarrow e'D^*X) = (3.76 \pm 0.12) \text{ nb},$$

where the uncertainty has statistical nature. No correction or selection criteria concerning diffractive event selection are applied.

The total predicted inclusive DIS cross section from RAPGAP amounts 3.91 nb. Figure 7.3 shows the cross sections differentially as a function of different variables. The RAPGAP Monte Carlo simulation for the inclusive DIS sample gives a good description of the measured distributions (some exception can be seen for $|\eta(D^*)|$ and $p_t(D^*)$). Therefore we may conclude, that the selection criteria of the DIS events are chosen correctly.

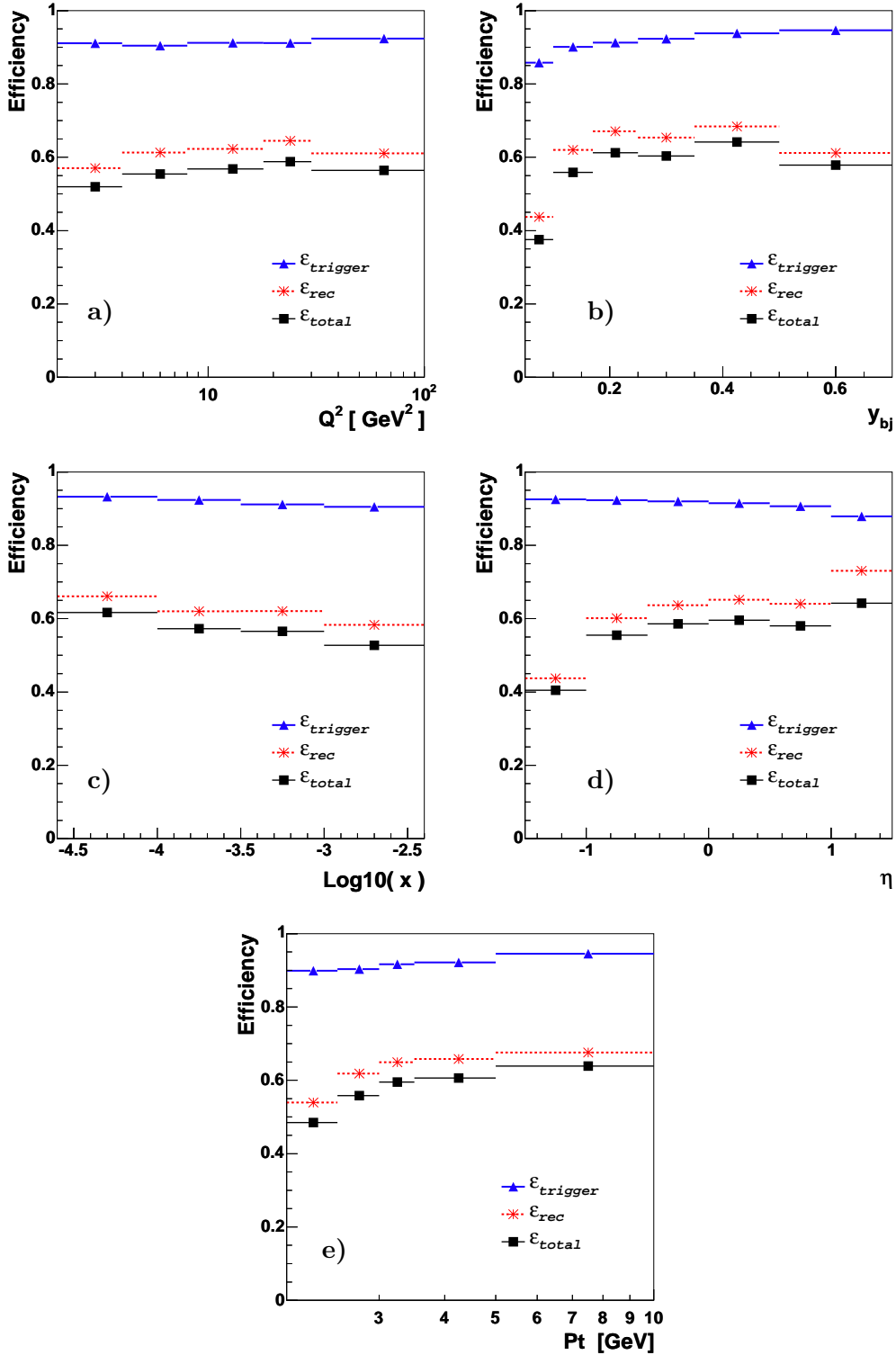


Figure 7.2: Trigger efficiency, reconstruction efficiency and final combined efficiency as a function of (a) Q^2 , (b) y_{bj} , (c) $\log_{10}(x)$, (d) $|\eta(D^*)|$ and (e) $p_t(D^*)$ for the measurement of differential inclusive cross sections. These correction factors are determined using the inclusive RAPGAP Monte Carlo sample.

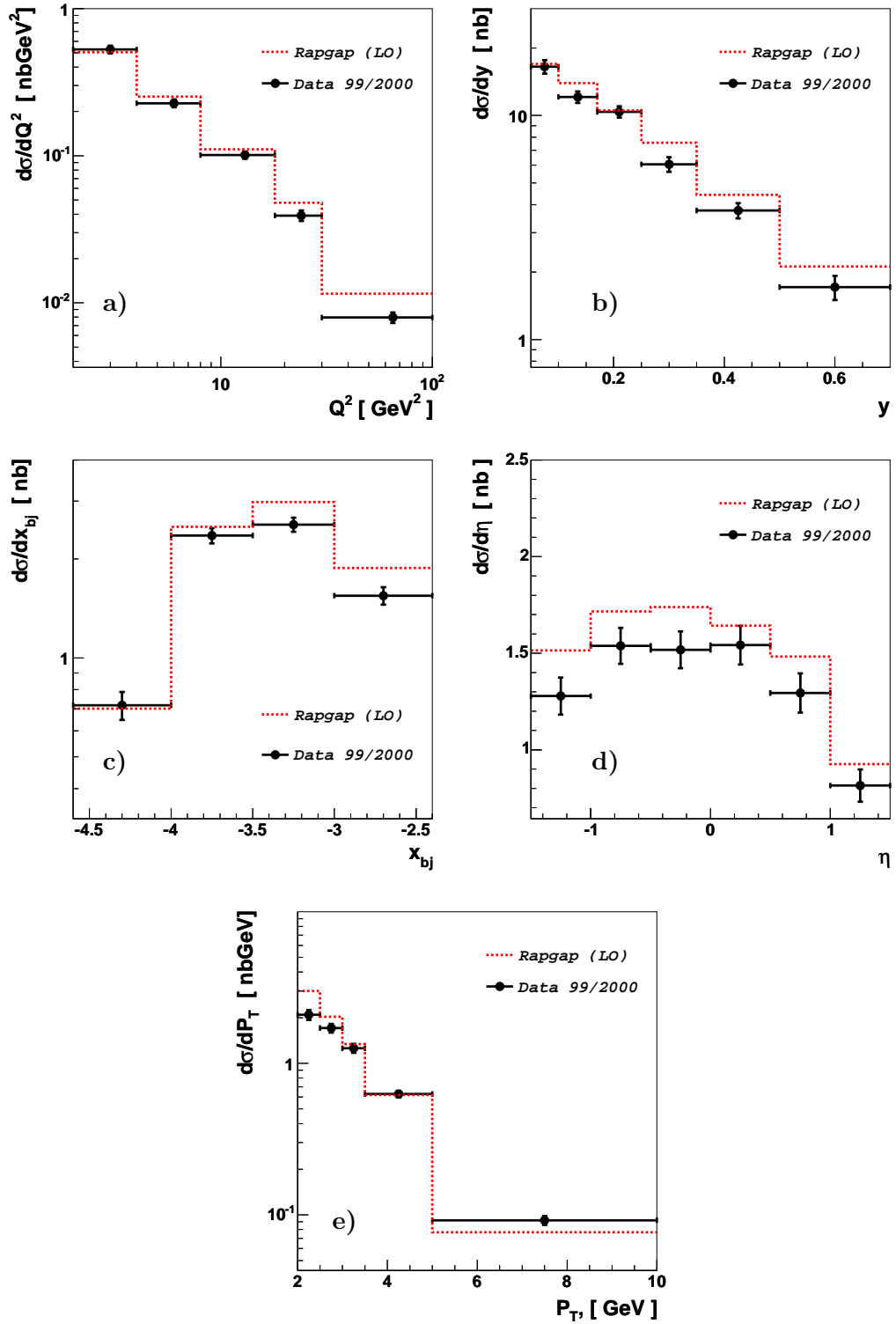


Figure 7.3: The inclusive DIS D^* cross section plotted differentially as a function of (a) Q^2 , (b) y , (c) x_{bj} , (d) $\eta(D^*)$, (e) $P_t(D^*)$. The data are shown as circles with error bars (statistic uncertainty).

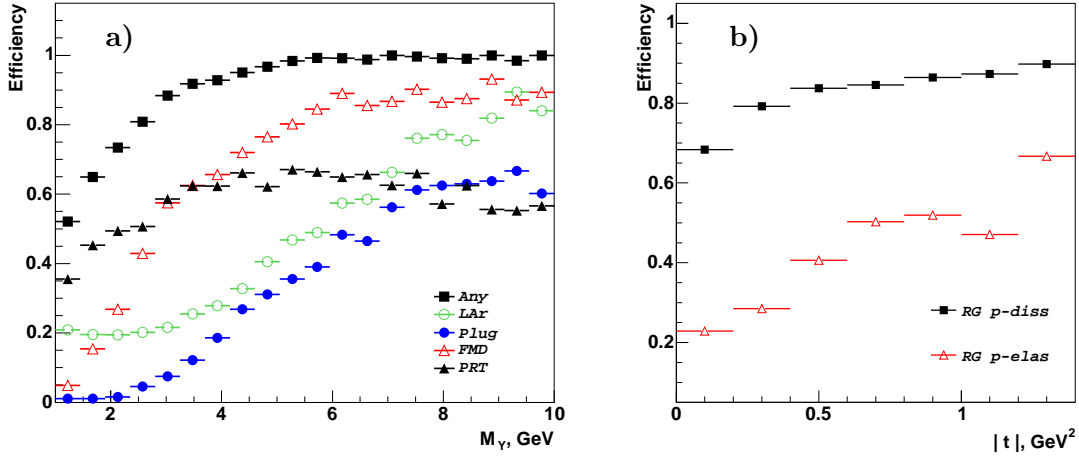


Figure 7.4: (a) Efficiency for tagging dissociated low-mass states, as a function of M_Y obtained from the simulation of D^* events generated with the Monte Carlo generator RAPGAP. The efficiency for any forward detector is indicated by full squares, for the LAR by open circles, the Plug is shown with full circles, the efficiency of the FMD is plotted with open triangles and for the PRT full triangles are used. (b) Comparison of the acceptance of the forward detectors as a function of $|t|$ for dissociative and elastic events.

7.3 Diffractive Measurements

7.3.1 Correction for proton-dissociative events

As was explained in Section 6 diffractive events can be selected in two very different ways. Using the Forward Proton Spectrometer events with elastically scattered protons are selected, or using the *rapidity gap method* where either elastic events or events with dissociated proton are selected. In this analysis diffractive events were selected on the basis of the latter method. The Forward Detectors were used to distinguish elastic and proton-dissociated events.

Figure 7.4 a) presents the performance of the Forward Detectors which are used in the diffractive selection chain, as a function of the mass M_Y of the dissociative system Y . The dissociative events are simulated with the RAPGAP Monte Carlo Generator (see Section 4.3). For example, the points labeled **Any** show the efficiency for tagging a dissociative event by any of the Forward Detectors, if this event passes the appropriate selection cuts. Details of the selection cuts are given in Sections 6.2-6.5. The efficiency of the Proton Remnant Tagger is shown after applying the reweighting procedure (see Section 6.5). Although events with an elastic proton can be efficiently detected by the PRT and proton dissociative events can be verified by the FMD, there is no clear way to distinguish these two groups of events. For large M_Y values ($M_Y > 3$ GeV) the detection efficiency for any of the forward detectors reaches 90 %, however it falls steeply towards the mass of elastically scattered protons. At $M_Y = 1.6$ GeV the acceptance is about 60%.

Figure 7.4 b), where the tagging efficiencies for elastic and dissociative proton are

compared as a function of $|t|$, shows, that the tagging of proton dissociation in the studied region of $|t|$ has an average efficiency of 80 %, and the tagging efficiency for elastic scattering with $M_Y = m_p$ is about 50% at $|t| = 1$ GeV.

Analysing the plots one can come to the conclusion, that there is no clear possibility to distinguish elastic events from the events, where the proton dissociates diffractively.

In order to scale down the influence of the dissociatively scattered proton, the diffractive cross sections are measured for the following diffractive kinematic region:

$$M_Y < 1.6 \text{ GeV} \quad (7.5)$$

$$|t| < 1.0 \text{ GeV}^2 \quad (7.6)$$

Previous measurements of the diffractive D^* -mesons cross section were done by H1 [49] for the same kinematical region of M_Y and $|t|$.

The RAPGAP Monte Carlo sample with implemented proton dissociation in the final state is also used to determine the correction factor C_{pdiss} , to estimate smearing effects in and out of the cut value on M_Y (Equation 7.5). For the computation of the correction it is assumed, that reconstruction efficiencies of the system X for both elastic events and events where the proton dissociates are comparable. The proportion between these two group of events is assumed to be 1 : 1 (according to the studies presented in Section 4.3 and from inclusive measurements [50]). The correction factor is calculated by the formula

$$C_{pdiss} = \frac{N_{gen}^{ELAS} + N_{gen}^{PDISS(M_Y < 1.6 \text{ MeV})}}{N_{gen}^{ELAS} + N_{gen}^{PDISS(non-detected)}}, \quad (7.7)$$

where N_{gen}^{ELAS} (N_{gen}^{PDISS}) gives the number of generated elastic (dissociative) events in the measured kinematical region. $N_{gen}^{PDISS(non-detected)}$ corresponds to the number of generated events with proton dissociation in final state, which after reconstruction and simulation passed through the forward detectors selection cuts. The obtained value for this correction amounts $C_{pdiss} = 1/1.038$, so that slightly more events migrate *into* the studied kinematical region, than *out* of it. The systematic uncertainty for the migration correction across the M_Y boundary is defined by varying M_Y and $|t|$ distributions and the ratio of proton elastic to the proton dissociation events and is presented in following section.

7.3.2 Uncertainty of the Cross Section

The first uncertainty which is given for the cross section measurement is statistical. It results from the corresponding data sample of selected events used in the D^* -fitting procedure, as described in Section 5.3.3. For the complete diffractive sample, the statistical uncertainty amounts approximately to 13 %. For the differential sets of events this value increases, because of the smaller statistics, and lies between 20-30 %.

The second component of the measurement error is systematic. A number of sources that contribute to the systematic error have been considered, some of them have already been mentioned in the previous sections. Below a summary is listed.

- Uncertainties of the trigger efficiencies for the composition of the used subtrigger have been determined as the maximum difference between the uncertainties defined for

the data and Monte Carlo simulation samples. This uncertainty gives a contribution of 3% to the systematic error, see Section 7.1.1.

- The uncertainty for the reconstruction of the tracks in the central tracker is adopted from the inclusive D^* analysis [51]. In the thesis presented here the D^* is reconstructed from its decay particles K , π , π_{slow} , where the latter is not reconstructed very well due to its low momentum. This leads to the large systematic uncertainty of 6 %.
- The so called golden decay channel $D^* \rightarrow D^0 \pi_{slow} \rightarrow K \pi \pi_{slow}$ is used to reconstruct the D^* meson. In the cross section measurement the number of D^* mesons has to be corrected for the corresponding branching ratio. It results in the uncertainty of 2.4 % [45].
- The uncertainty for the possible reflections, where other decay modes than the studied $D^* \rightarrow D^0 \pi_{slow} \rightarrow K \pi \pi_{slow}$ contribute to the Δm peak is determined to be 1.5 % [52]. This reflection is calculated using a Monte Carlo sample containing all possible decay modes of the D^* meson.
- The systematic uncertainty of the signal extraction coming from the D^* fitting procedure, as described in Section 5.3.3 is determined to be 6 %. This value is taken from the inclusive D^* analysis [47].
- A possible miscalibration of the electromagnetic energy scale in the SPACAL leads to an uncertainty of the positron energy estimation. The effect of this is estimated by a recalculation of the acceptance for the different energy scales of the positron candidates. The uncertainty is found to be 0.3 % if the energy of the positron is 27.5 GeV and 2 % at $E'_e = 8.0$ GeV. This results in a average systematic error of 5 % [53].
- An uncertainty for the angle of the scattered positron is determined in the similar way to the energy, as it indicated above. A systematic error of 1 % is obtained from the variation of the scattered positron angle by 1 mrad.
- The uncertainty of the tagging efficiency of the PRT detector was determined by reweighting the diffractive Monte Carlo simulation within the statistical accuracy of the measured efficiency with factors 0.5 and 2. It results in a contribution of 8 % to the total systematic uncertainty.
- The uncertainty of the correction factor for migration effects across the M_Y boundary is estimated from
 - variation the M_Y distribution with dissociative proton events by factors $\left(\frac{1}{M_Y}\right)^{\pm 0.3}$
 - study the $|t|$ -dependence in Monte Carlo sample with proton dissociation by changing the slope parameter with $e^{\pm 1|t|}$.
 - for elastic events the $|t|$ -distribution is varied with $e^{\pm 2|t|}$.
 - variation of the ratio of elastic and proton dissociative events from 1 : 2 to 2 : 1.
 All these variations lead to a total uncertainty of 5 % of the cross section.

- The uncertainty of the physics model for the diffractive D^* production implemented in RAPGAP is found to be 5 %. This contribution is estimated via recalculating the acceptance after varying the shape of the $x_{\mathcal{P}}$ and β distributions in the diffractive Monte Carlo with the weight factors $\left(\frac{1}{x_{\mathcal{P}}}\right)^{\pm 0.05}$ and $(1 \pm 1.5\beta)$ correspondingly. These weighting factors are chosen within the statistical accuracy of the measured sample. Figure 7.5 shows $x_{\mathcal{P}}$ and β distributions varied with several factors, one can see that the variations used for the uncertainty measurement lie mostly within the statistical errors of data. For comparison larger weights are shown, which result in significantly larger fluctuations not compatible with the measured distributions.
- The uncertainty of the determination of the integrated luminosity leads to an overall normalisation error on all data points of 1.5 %.

The largest contribution of 8 % to the total systematic error is presented by the uncertainty of the tagging efficiency of the PRT detector. The uncertainty of the physics model and the uncertainty for the reconstruction of the tracks in the central detector follow according to the size of the contributions to the error. All above listed components of the systematic uncertainty added in quadrature result to 15 % for the complete systematic error on the diffractive cross section measurement. Systematic and statistical errors are calculated individually for each bin and added in quadrature to derive the total error of the measurement.

7.3.3 Diffractive D^* Cross Section

For the selected diffractive sample with the number of D^* -mesons obtained from the ΔM fit $N(D^*) = 133 \pm 16$, the cross section in the visible kinematic region

$$\begin{aligned}
 2 &< Q^2 < 100 \text{ GeV}^2, \\
 0.05 &< y < 0.7, \\
 &p_t(D^*) > 2.0 \text{ GeV}, \\
 &|\eta(D^*)| < 1.5, \\
 &x_{\mathcal{P}} < 0.04, \\
 &M_y < 1.6, \\
 &|t| < 1. \text{ GeV}^2
 \end{aligned}$$

amounts to:

$$\sigma(ep \rightarrow e'(D^* X)Y) = 249 \pm 31(stat.) \pm 30(sys) \text{ pb},$$

The cross section obtained in this analysis is found to be in good agreement with the previous H1 measurement from [54]. The present analysis is performed in the same kinematical region as the previous one, using some additional knowledge in the *rapidity gap* event selection.

Figures 7.8 and 7.9 show the differential diffractive cross sections as a function of the variables Q^2 , y_{bj} , x_{bj} , $|\eta(D^*)|$, $p_t(D^*)$, $p_t^*(D^*)$, $\text{Log}_{10}(\beta)$, $\text{Log}_{10}(x_{\mathcal{P}})$ and $z_{\mathcal{P}}$. In these figures the inner error bars represent the statistical uncertainty, whereas the outer error bars correspond to the quadratic sum of the statistical and systematic uncertainties. The Δm distributions for the bins of the differential distributions are given in Figures C.7-C.15.

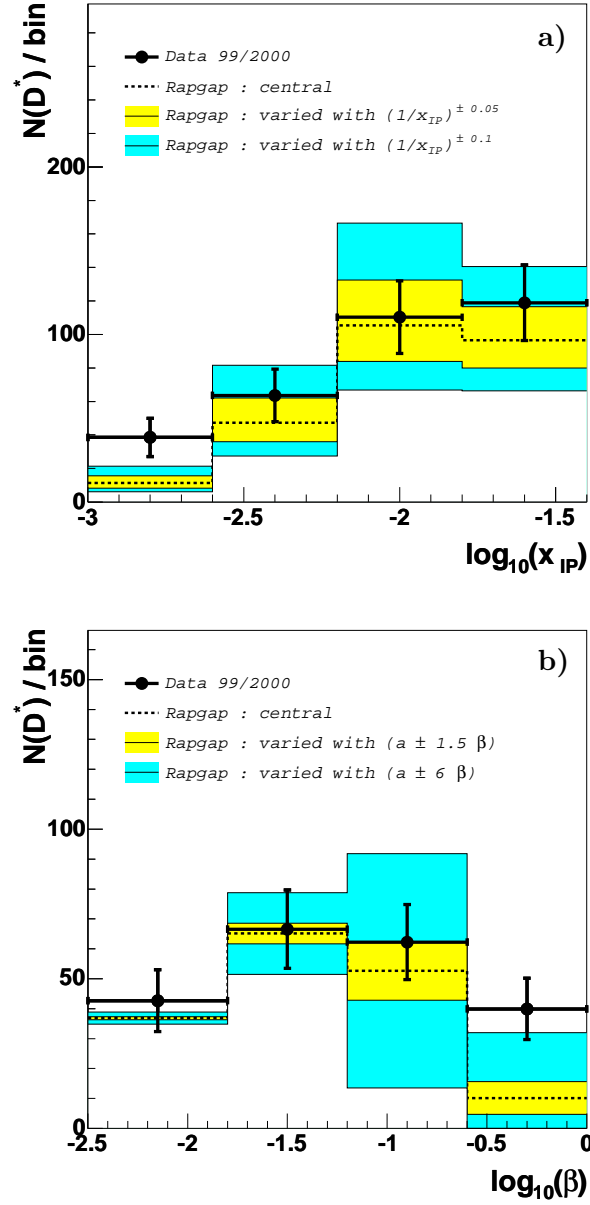


Figure 7.5: Determination of the uncertainties of the model dependence: variations of the shapes for the x_{IP} (a) and β (b) distributions are shown. The yellow (light grey) band presents the variations within the systematic uncertainties of the data, for comparison the blue (dark) one shows larger limits.

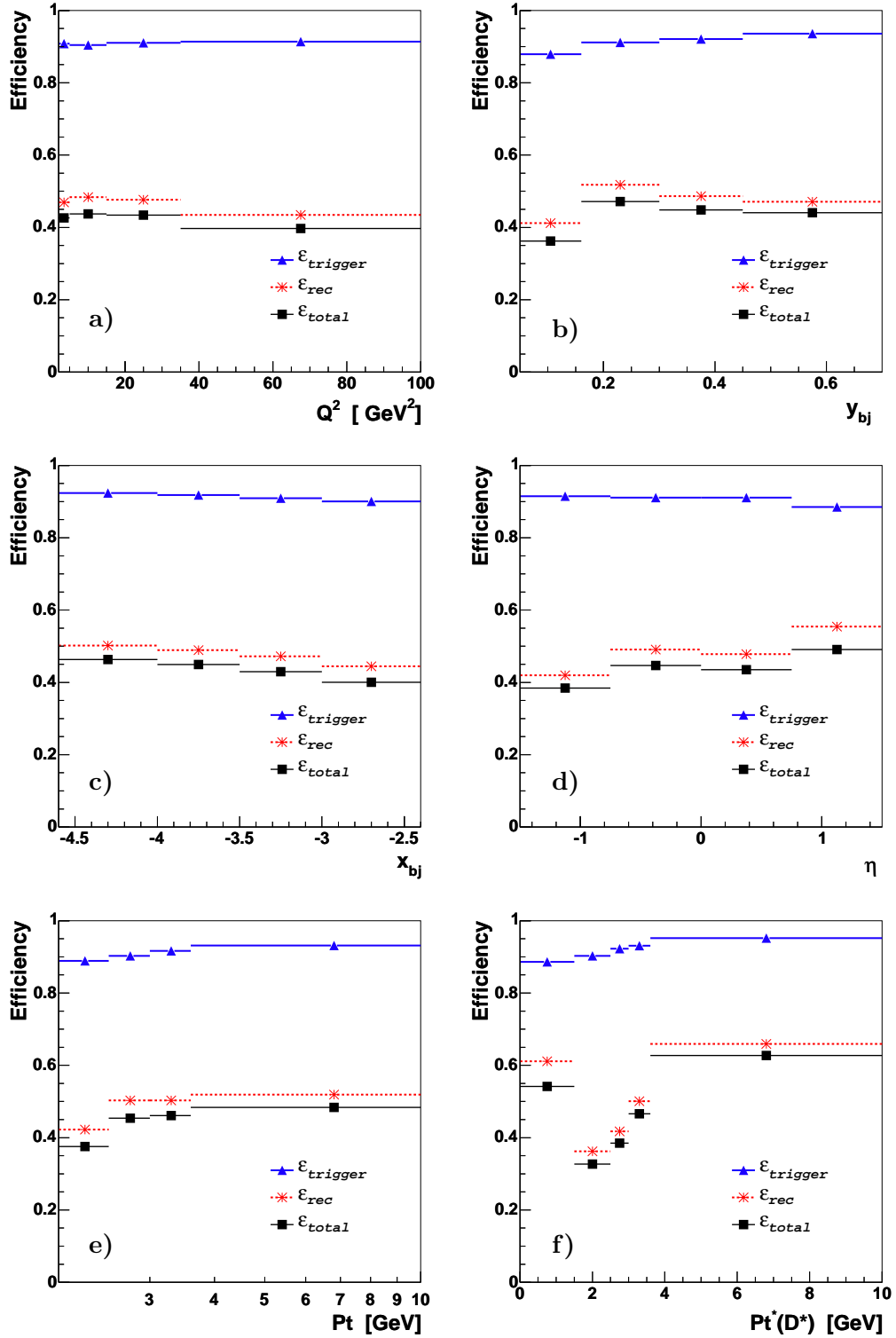


Figure 7.6: Shown are trigger efficiency, reconstruction efficiency and final combined efficiency as a function of (a) Q^2 , (b) y_{bj} , (c) $\log_{10}(\mathbf{x})$, (d) $|\eta(D^*)|$, (e) $p_t(D^*)$ and (e) $p_t^*(D^*)$ for the measurement of the differential diffractive cross sections.

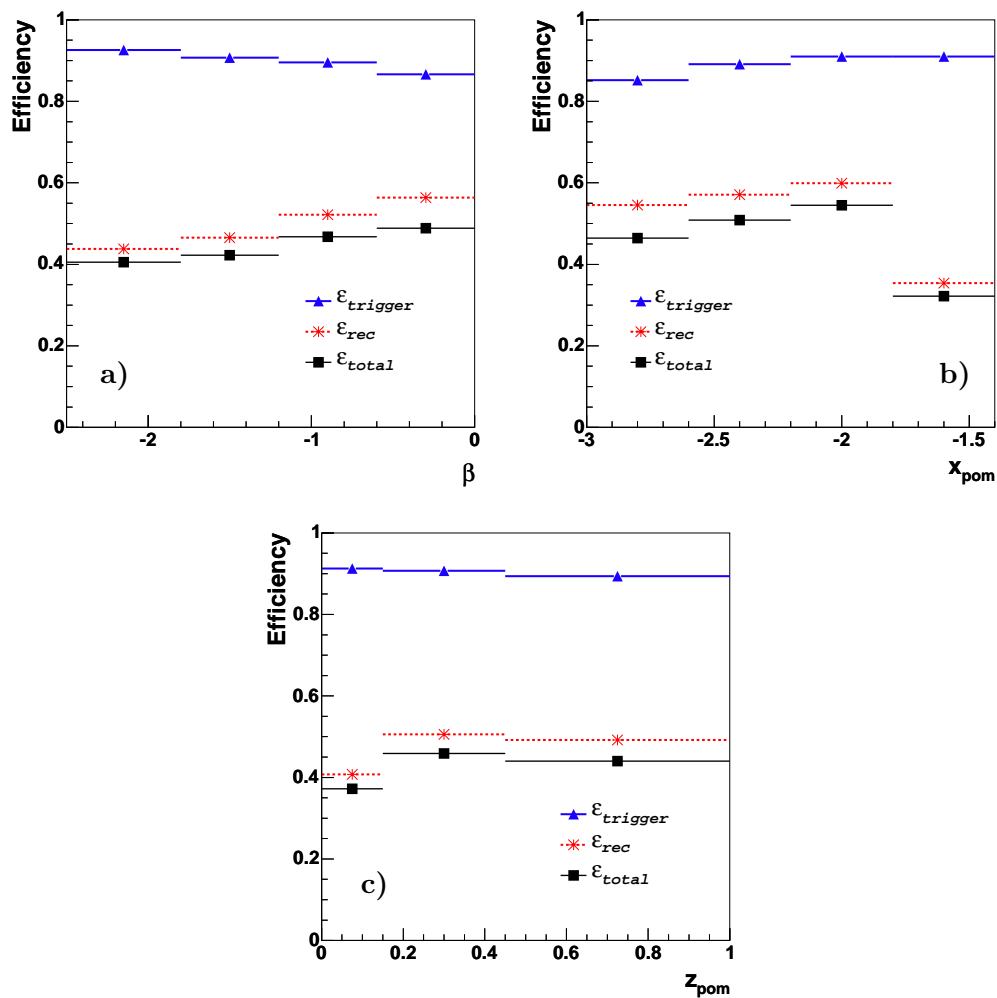


Figure 7.7: Trigger, reconstruction and total efficiencies for the selected diffractive D^* -meson sample as a function of (a) β , (b) $\log_{10}(x_P)$ and (c) z_P .

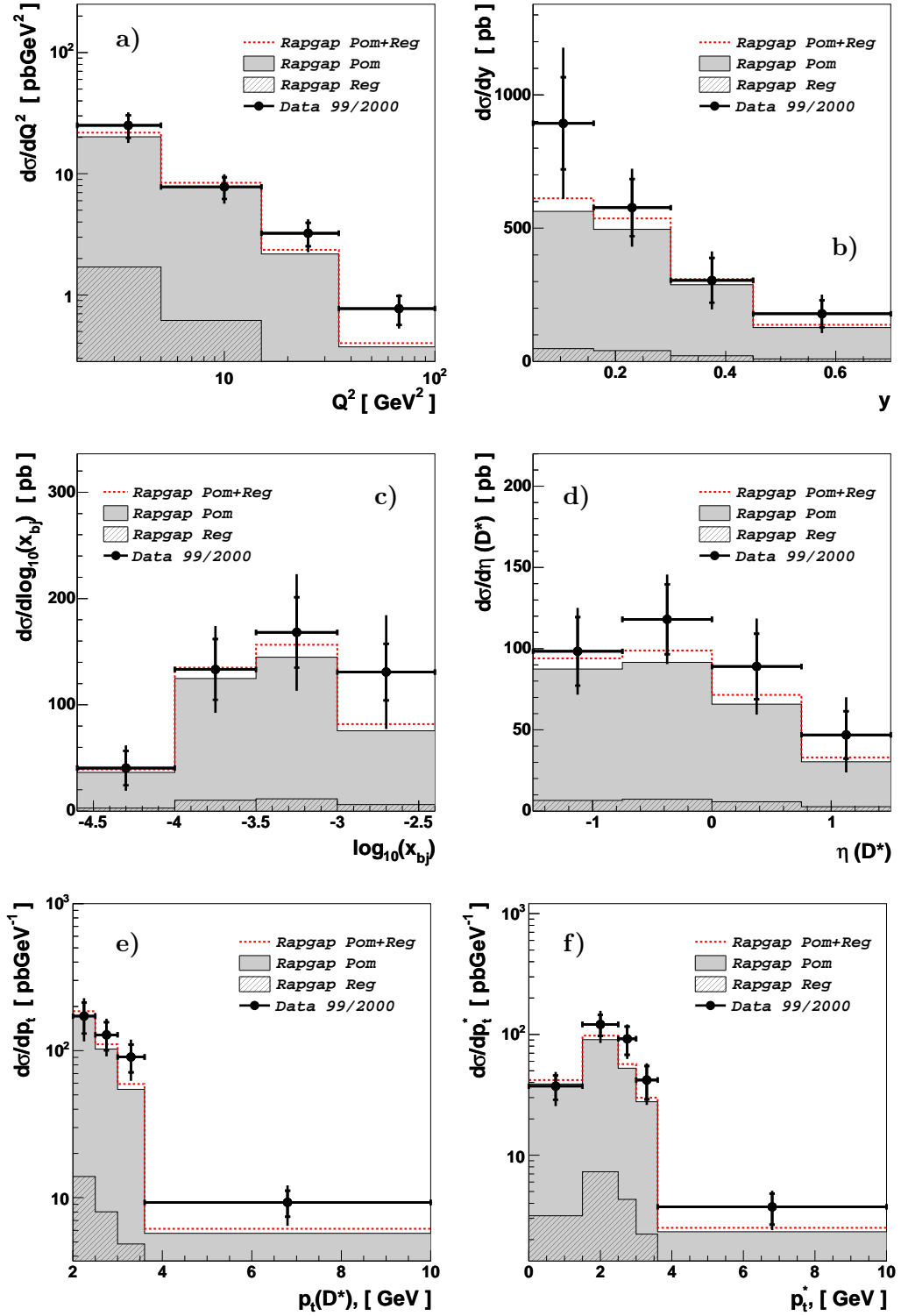


Figure 7.8: The differential diffractive D^* cross sections as a function of (a) Q^2 , (b) y , (c) x_{bj} , (d) $\eta(D^*)$, (e) $P_t(D^*)$. The data are shown as points with error bars, which represent the full error of the measurements calculated as quadratic sum over the statistical and systematic errors.

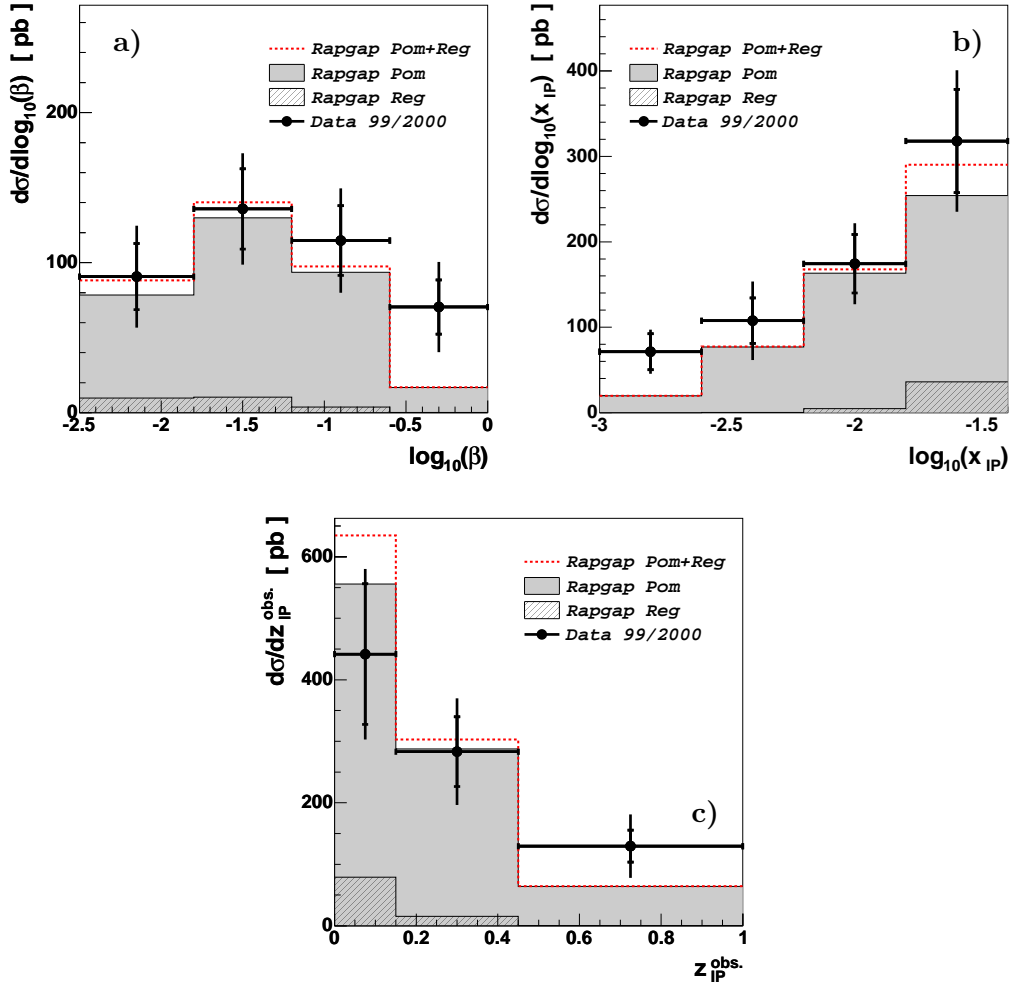


Figure 7.9: The differential diffractive D^* cross sections as a function of (a) Q^2 , (b) y , (c) x_{bj} , (d) $\eta(D^*)$, (e) $P_t(D^*)$. The data are shown as points. The error bars represent the full error of the measurements calculated as quadratic sum over the statistical and systematic errors.

7.4 Data Comparison with Theory

A prediction for the diffractive cross section was obtained using the Monte Carlo RAP-GAP [40]. At first, the measured diffractive cross section is compared to the prediction presented by the collinear factorisation model (see Section 2.9.1), where diffractive events are modelled as the collision of a virtual photon with a partonic pomeron, emitted from the proton. Next, two gluon exchange is presented as an alternative model, which describes the production of charm in diffraction via partonic fluctuations of the photon, using the unintegrated parton distribution functions (discussed in Section 2.9.2). For all calculations the factorisation and normalisation scales were set to $\mu_r^2 = \mu_f^2 = Q^2 + p_t^2 + 4m_c^2$, the charm mass was chosen to be $m_c = 1.5$ GeV, Λ_{QCD} was set to 0.20 GeV and the number of active quark flavours $N_f = 4$. The predictions of these two models are listed in Tables 7.1-7.2.

- **Collinear Factorisation Approach**

$x_{\mathcal{P}} < 0.04$ (**measured cross section** $\sigma(ep \rightarrow e'(D^*X)Y) = 249 \pm 31 \pm 36$ **pb**)

Predictions of the factorisable pomeron model are calculated using parton distributions, which are dominated by gluons (see Figure 2.10), obtained from a QCD analysis of the diffractive structure function $F_2^{D(3)}$ [20]. The leading order of the diffractive parton densities was used. Within the scope of this model, the proton, corresponding to the Regge theory, can couple to a pomeron or a reggeon. In the Figures the reggeon exchange is presented individual.

The expectation of this model is found to be in good agreement with the measured diffractive DIS cross section within the quoted errors. All measured differential distributions, which are given in Figures 7.8 and 7.9, are generally well described by the collinear factorisation approach with the H1 Fit 2002 parton densities parametrisation. The predictions for the collinear factorisation approach using the H1 Fit 2002 and H1 Fit 2002 parton densities parametrisation are presented for the comparison in the Tables 7.1-7.2.

- **2-gluon Model**

$x_{\mathcal{P}} < 0.01$ (**measured cross section** $\sigma(ep \rightarrow e'(D^*X)Y) = 104 \pm 23 \pm 23$ **pb**)

The data are also compared to a prediction from the perturbative 2-gluon approach “BJKLW” [25, 26] using the unintegrated gluon density [55] obtained from the inclusive structure function F_2 evolved by the CCFM evolution equation (see Appendix D). Cross sections predictions are presented in the studied kinematical region with an additional restriction on $x_{\mathcal{P}} < 0.01$. The latter limit is applied because the perturbative 2-gluon model is valid only in the region of small $x_{\mathcal{P}}$, where the proton parton distributions are gluon dominated and there are no contributions from secondary reggeon exchanges. In the BJKLW parametrisation the contribution from $q\bar{q}$ states is significantly smaller in contrast to the contribution from $q\bar{q}g$ states. A cut on the transverse momentum of the gluon in the $q\bar{q}g$ states needs to be applied. The dynamics of the 2-gluon model predictions was studied for two different unintegrated gluon densities sets **J2003 set 1 and 2** (for details see Appendix D) and four different values of the transverse momentum cut of the gluon in the $q\bar{q}g$ states.

The constraint on $x_{\mathcal{P}}$ reduces the diffractive data sample approximately by a factor of 2. Figure C.16 shows the Δm distributions for the diffractive data sample, selected

in the kinematical region as described before, after applying the cut on $x_{\mathcal{P}} < 0.01$. The number of D^* -mesons from the fit is $N(D^*) = 61 \pm 11$ events.

Figure 7.10 shows the data together with the predictions of BJKLW model and factorisable pomeron model. In these differential distributions for the BJKLW model **J2003 set 1** unintegrated gluon densities was used. Using the cut of $P_t(g) > 2.\text{GeV}$ the perturbative 2-gluon model gives also a good description of the analysed data within the estimated uncertainties in the range $x_{\mathcal{P}} < 0.01$. Increasing or decreasing the cut value of the gluon leads to wide fluctuations in the predicted cross section. All predictions of the model are presented in the Table 7.2.

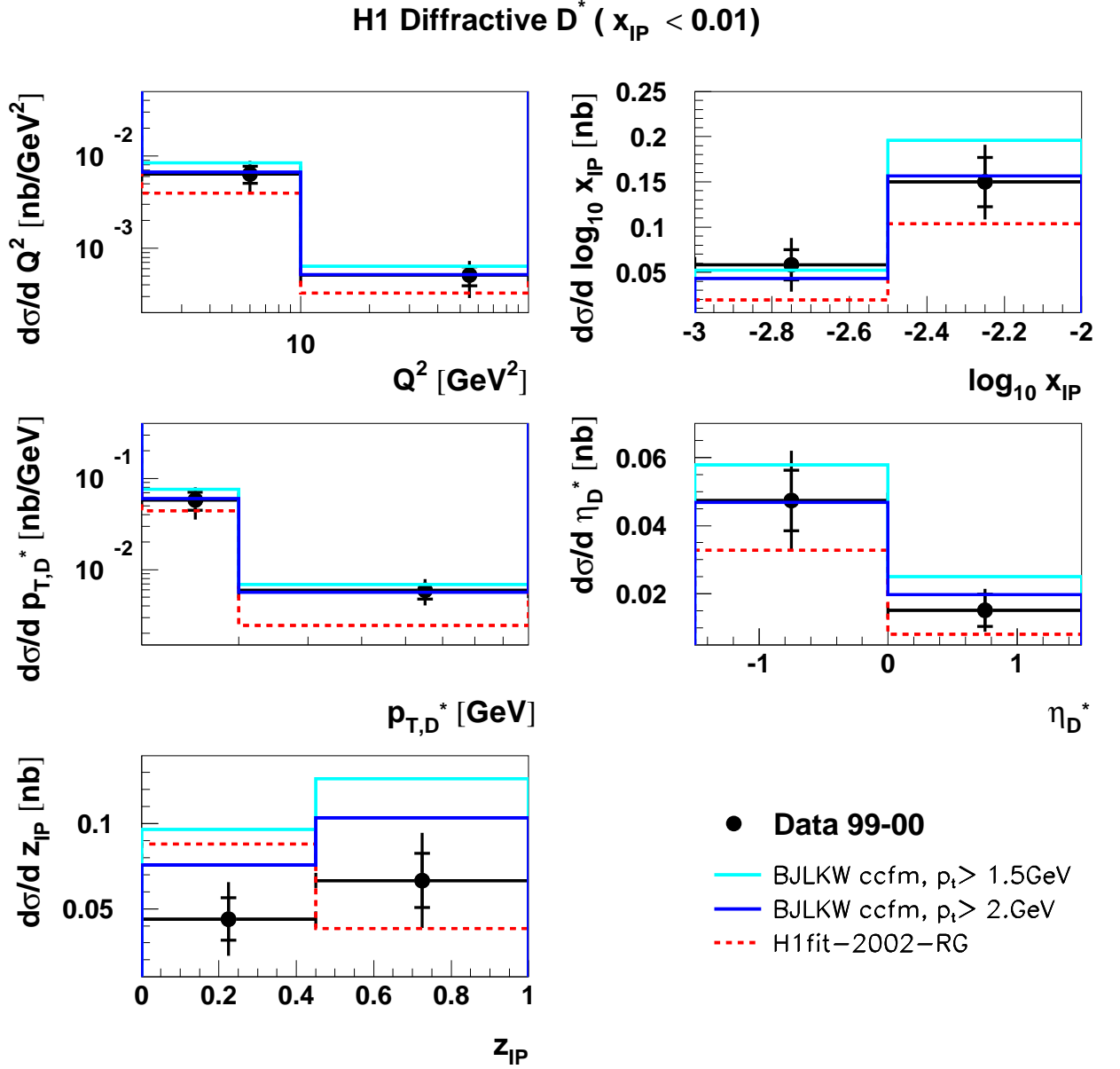


Figure 7.10: Cross sections for diffractive D^* meson production in DIS in the low kinematic region of $x_{\mathcal{P}} < 0.01$ are shown differentially as a function of (a) Q^2 , (b) $x_{\mathcal{P}}$, (c) $P_t(D^*)$, (d) $\eta(D^*)$ and (e) $z_{\mathcal{P}}$. The inner error bars of the data points corresponds to the statistical uncertainties, whereas the outer error bars represent the statistical and systematic uncertainties added in quadrature. The data are compared with a prediction from the perturbative 2-gluon approach of BJKLW using the unintegrated gluon density (J2003 set 2). Predictions for two different p_t cuts of the gluon in the $c\bar{c}g$ process are given. The leading order predictions are presented by the factorisable pomeron approach using $F_2^{D(3)}$ H1 fit 2002.

$x_P < 0.04$			
Data 99/2000	249 ± 31 (stat.) ± 30 (sys) pb		
Collinear Factorisation Approach	$\mu_r^2 = \mu_f^2 = Q^2 + p_t^2 + 4m_c^2$ $m_c = 1.5$ $\Lambda_{QCD} = 0.2$ GeV $N_f = 4$	$F_2^{D(3)}$ H1 fit 2002	254 [pb]
		$F_2^{D(3)}$ H1 fit 2006	213 [pb]

Table 7.1: The predictions for the total diffractive cross section of the collinear factorisation approach are presented for comparison with the measured cross-section. μ_r and μ_f are renormalisation and factorisation scales correspondingly, m_c is mass of the charm quark.

$x_{\mathcal{P}} < 0.01$					
Data 99/2000	104 ± 23 (stat.) ± 23 (sys) [pb]				
Perturbative 2-Gluon Exchange (BJKLW)	$\mu_r^2 = \mu_f^2 = Q^2 + p_t^2 + 4m_c^2$ $m_c = 1.5$ $\Lambda_{QCD} = 0.2$ GeV $N_f = 4$	unintegrated PDF J2003 set 1	$q\bar{q}$	38 [pb]	
			$q\bar{q}g$	$p_t(g) > 0.5$ GeV	302 [pb]
				$p_t(g) > 1.0$ GeV	199 [pb]
		$p_t(g) > 1.5$ GeV		181 [pb]	
		$p_t(g) > 2.0$ GeV		145 [pb]	
		$p_t(g) > 2.5$ GeV		119 [pb]	
unintegrated PDF J2003 set 2	$q\bar{q}$	33 [pb]			
	$q\bar{q}g$	$p_t(g) > 0.5$ GeV	262 [pb]		
		$p_t(g) > 1.0$ GeV	209 [pb]		
		$p_t(g) > 1.5$ GeV	127 [pb]		
		$p_t(g) > 2.0$ GeV	98 [pb]		
		$p_t(g) > 2.5$ GeV	90 [pb]		
Collinear Factorisation Approach	$\mu_r^2 = \mu_f^2 = Q^2 + p_t^2 + 4m_c^2$ $m_c = 1.5$ $\Lambda_{QCD} = 0.2$ GeV $N_f = 4$	$F_2^{D(3)}$ H1 fit 2002		79 [pb]	
		$F_2^{D(3)}$ H1 fit 2006		48 [pb]	

Table 7.2: The predictions for the total diffractive cross section for the low $x_{\mathcal{P}}$ region of the collinear factorisation approach and perturbative 2-gluon model are presented for comparison with the measured cross-section. μ_r and μ_f are renormalisation and factorisation scales correspondingly, m_c is mass of the charm quark.

Chapter 8

Summary and Outlook

Over the last few decades diffractive interactions have received a lot of attention. Initially diffractive reactions were studied intensively in the sixties, in that time the existence of these events was explained phenomenologically. At the present time, after the advent QCD techniques, diffractive events provide an interesting field to use perturbative QCD for understanding the underlying dynamics of diffractive phenomena.

In this thesis the analysis of open charm production in diffractive deep-inelastic scattering was presented. A data sample was used which corresponds to an integrated luminosity of $\mathcal{L}^{int} = 46.8 \text{ pb}^{-1}$, recorded with the H1-Detector in the years 1999 and 2000, when the HERA machine collided 27.6 GeV positrons with 920 GeV protons. In relation to a previous H1 measurement [54], the integrated luminosity was increased by a factor of 2. The measurements is done for the same kinematical region as was used in the previous measurement.

$$\begin{aligned} 2 &< Q^2 < 100 \text{ GeV}^2, \\ 0.05 &< y < 0.7, \\ &p_t(D^*) > 2.0 \text{ GeV}, \\ &|\eta(D^*)| < 1.5, \\ &x_{\mathcal{P}} < 0.04, \\ &M_y < 1.6, \\ &|t| < 1. \text{ GeV}^2 \end{aligned}$$

Diffractive events are selected using *rapidity gap selection* which uses the observation, that events produced diffractively have two distinct systems X and Y in the hadronic final state separated by a region in pseudo-rapidity, where no hadron activity is detected. Open charm events are tagged by reconstruction of D^* -mesons in the “golden” decay channel $D^* \rightarrow D^0 \pi_{slow} \rightarrow K \pi \pi_{slow}$. The diffractive cross section in the visible kinematical region is found to be

$$\sigma(ep \rightarrow e'(D^* X)Y) = 249 \pm 31(stat.) \pm 30(sys) \text{ pb}.$$

The measured cross section was compared to the theory predictions from the factorisable pomeron approach and two gluon exchange.

The collinear factorisation approach with diffractive parton distributions (H1 Fit 2002) extracted from $F_2^{D(3)}$ data [20], which are dominated by gluons at the starting scale, gives

very good description in shape of all differential distributions. The measured cross section agrees very well with the prediction from this model. This fact supports the validity of diffractive hard scattering in DIS.

The perturbative two gluon approach, where photon fluctuates to $q\bar{q}$ or $q\bar{q}g$ states, uses un-integrated gluon densities. This model traditionally was used as an alternative model for diffractive phenomena. The dynamics of the perturbative two gluon exchange prediction is studied for different $p_t(g)$ cut values of the gluon in the $q\bar{q}g$ state, where the gluon is not a soft remnant, but presents a hard parton. The prediction of this model for the $p_t(g) > 2.0$ GeV and using **J2003 set 1** un-integrated gluon densities is able to describe the diffractive data sample, although the data still have large uncertainties.

The study of diffractive charm production presents an attractive and successful tool to test the nature of diffractive interactions and particularly the role of gluons in it. Both of the discussed theory predictions give reasonable description of the diffractive data and give the opportunity to understand the physics assumption of the models in more details, but still have some unclear aspects and need to be refined.

Hopefully, a luminosity, achieved by the HERA II will enable much more precise measurements of diffractive charm production. It will become practicable to measure the cross section in several more bins of $x_{\mathcal{P}}$ or $z_{\mathcal{P}}$, to investigate better the dynamics of diffractive phenomena.

Appendix A

Detailed Run Selection

The data recorded with the H1-Detector in the 1999 and 2000 years were examined in this analysis. The general points regarding the run range selection used in the analysis were already discussed in the Section 5. A summary of the used runs were given in Table 5.1.

Here single rejected runs or small groups of runs are listed. The motivation for sorting out of the runs presented in the Table A.1 was the lack of understanding of the electronic noise level in some channels of the Proton Remnant Tagger, which was higher than the average value (see Figure 6.12).

Further periods, which are listed in the Table A.2, were rejected on the basis of poor performance of the multi-wire proportional chambers (MWPC), of the CIP and the COP. The latter information is inherited from the [51].

The luminosity of the run periods rejected from the analysis amounts to 5.33 pb^{-1} .

<i>1999 positron</i>	<i>2000</i>
<i>246888-246889,</i>	<i>263515-263517, 263606-263612, 263666-263672, 263739-263742,</i>
<i>247190-247195,</i>	<i>265420-265421, 265423-265424, 265429-265430, 265435-265436,</i>
<i>247254-247256,</i>	<i>265484-265488, 265511-265515, 265519-265523, 265525-265526,</i>
<i>247258-247260,</i>	<i>265566-265575, 265635-265636, 265679-265680, 265682-265683,</i>
<i>247262-247263,</i>	<i>265685-265686, 265688-265689, 265694-265695, 265748-265756,</i>
<i>247582-247584,</i>	<i>265823-265825, 265827-265830, 265878-265882, 265994-265996,</i>
<i>261155-261156,</i>	<i>266916-266919, 266964-266966, 267195-267196, 267504-267506,</i>
	<i>268747-268748,</i>
<i>241456, 246891,</i>	<i>264221, 264223, 264396, 264494, 264503, 265418, 265528, 265639,</i>
<i>246893, 246895,</i>	<i>265652, 265654, 265657, 265659, 265692, 265699, 265701, 265703,</i>
<i>255587, 256482,</i>	<i>265705, 265709, 265833, 265884, 266808, 266970, 267465, 268740,</i>
<i>257373, 260272,</i>	<i>274046.</i>
<i>261147.</i>	

Table A.1: *List of the rejected run ranges due to relatively high level of the electronic noise in the Proton Remnant Tagger.*

1999 positron	2000
246159-246170, 246266-246325, 246583-246604, 246638-246640, 247064-247068, 249065-249066, 249264-249280, 249346-249378, 249597-249645, 250822-250833, 251636-251637, 251746-251754, 251908-251910, 252013-252017, 252587-252588, 253319-253322, 253328-253357, 253496-253497, 254170-254185, 254332-254338, 254482-254487, 254780-254789, 256341-256343, 256495-256496, 256753-256758, 257178-257190, 257556-257562, 257641-257648, 257692-257696, 258555-258556, 259114-259115, 259141-259144, 259293-259313, 246569, 246729, 247973, 248111, 248660, 248755, 248761, 248882, 248906, 251001, 251187, 251772, 252046, 252266, 252582, 253565, 254387, 255171, 255549, 257517, 257532, 257754, 258049, 258169, 258552, 258033, 258120, 259095, 259107, 259109, 259147, 259151, 259418.	262714-262721, 263270-263291, 263331-263359, 264321-264330, 264706-264707, 264999-265004, 265270-265277, 265679-265699, 265932-265934, 266105-266107, 266443-266444, 266573-266577, 267320-267323, 267822-267960, 268639-268675, 268954-268965, 269433-269435, 269991-270057, 270141-270142, 270626-270628, 270788-270799, 270877-270883, 271122-271124, 272122-272323, 272447-272449, 273623-273629, 274161-274162, 274164-274166, 274169-274174, 274257-274259, 274261-274268, 277424-277426, 277451-277456, 277475-277476, 277480-277489, 277491-277492, 278687-278978, 262393, 262534, 262840, 263052, 263152, 263219, 263381, 263526, 263529, 263692, 263701, 264296, 264817, 265238, 265241, 265278, 265365, 265519, 265765, 265893, 265997, 266049, 266111, 266320, 266451, 267317, 267565, 268259, 268587, 268637, 269310, 270136, 270800, 270805, 270886, 270893, 270895, 271117, 271902, 272451, 272887, 273098, 273344, 273442, 274836, 274907, 275255, 275717, 276081, 276704, 276710, 276911, 277495, 277957, 279144, 279162.

Table A.2: Excluded run periods because of low performance of the multi-wire proportional chambers (MWPC) of the CIP and the COP.

Appendix B

Algorithm for the "Probability" Method

As was already mentioned in Section 6.1.1, the noise effects present in the Plug and the Forward Muon Detector (FMD) are not contained in the standard Monte Carlo simulations and an additional treatment is needed.

Details of the "probability" method for the determination of the noise value, N_{NOISE} , (See Equation 6.1) are presented below. This method is based on a general Monte Carlo method, called "Hit-or-Miss Method". The main points of this Monte Carlo method are briefly presented in the following.

In order to generate a distribution according to a complicated function $f(x)$:

- choose randomly x from a random number
- choose randomly y from another random number
- keep the pair (x, y) if $y < f(x)$, otherwise reject it
- do that for many times and the distribution of (x, y) pairs follows the function $f(x)$
- the final distribution of the accepted (x, y) pairs has weight = 1

The "Hit-or-Miss Method" has the advantage that $f(x)$ can be any function, which is defined in the (x, y) range.

The basic idea of the used in the analysis "probability" method is illustrated in the figure B.1 for the example of the Forward Muon Detector.

- An array **A** consists of probabilities to find a noise hit in the pre-toroid FMD layers. The content of this array is extracted from the random trigger sample.
- A random number generator `Rndm1()` provides the number of coincident FMD hits, `Hits_rndm`.
- From the array **A** the corresponding value of the hit probability `P(Hits_rndm)` is determined.
- Using another random function, `Rndm2()`, a value `P(rndm)` is received, which is as well a finding hit probability.

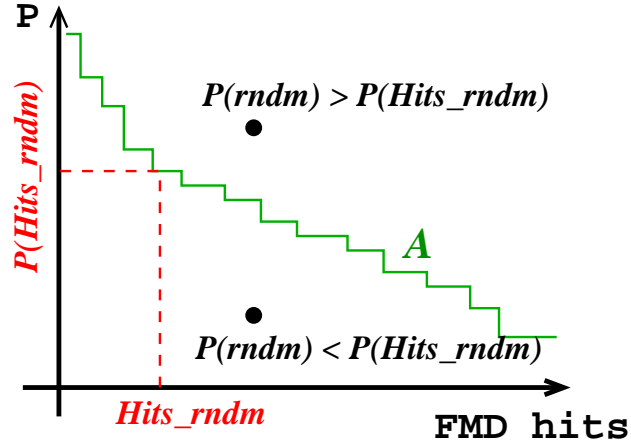


Figure B.1: Probability function $f(p)$.

- If the finding probability, $P(\text{rndm})$, is less than the probability to find the FMD hits, $P(\text{Hits_rndm})$, the value Hits_rndm is accepted and used as N_{NOISE} .
- If the probability given by the second random function is larger than that stored in the probabilities array, the potential noise value, Hits_rndm , will be rejected, the whole algorithm will be repeated until the number of noise hits, N_{NOISE} , is determined.

The big advantage of this method is its easy application. However, applying this noise scheme does not fully describe the real noise, because the correlations between the Plug and the FMD detectors are not included. Also using this method, noise effects in the FMD can be treated only as a sum in the first three layers, but existing correlations between FMD layers cannot be taken into account.

Appendix C

The mass difference signals for the measurement of the differential DIS and DDIS cross sections.

As introduced in Section 5.3.3, the number of selected in the data sample D^* mesons is determined by fitting the Δm distribution, where the Δm signal is built by the difference between the invariant masses of the D^* and D^0 candidates.

In the following, mass difference distributions are given for the each bin of the measured differential inclusive and diffractive cross sections. For the Δm signals with insufficient statistics for a fit of all six parameters, or if such a fit gives unreasonable result, the fitting procedure with fixed μ , σ and u_s is performed. In this case the fixed parameters are taken from the fit to the reference distribution. As the reference distribution, the distribution presented on figure C.1 is assumed.

At first, the fit distribution of the total Δm signal after the whole DIS selection (see Chapter 5) and trigger requirements is shown. Then, the mass difference distributions are presented in the differential binning of Q^2 , y_{bj} , x_{bj} , $\eta(D^*)$ and $p_t(D^*)$ variables.

Then the Δm signals after the diffractive DIS selection (for details of the selection see Chapter 6) are shown. The complete and differential diffractive DIS signals are shown.

Finally, the differential Δm distributions for the low $x_P < 0.01$ kinematical region are presented. This diffractive data sample, with low x_P restriction condition is interesting for the comparison with the 2gluon model of diffraction.

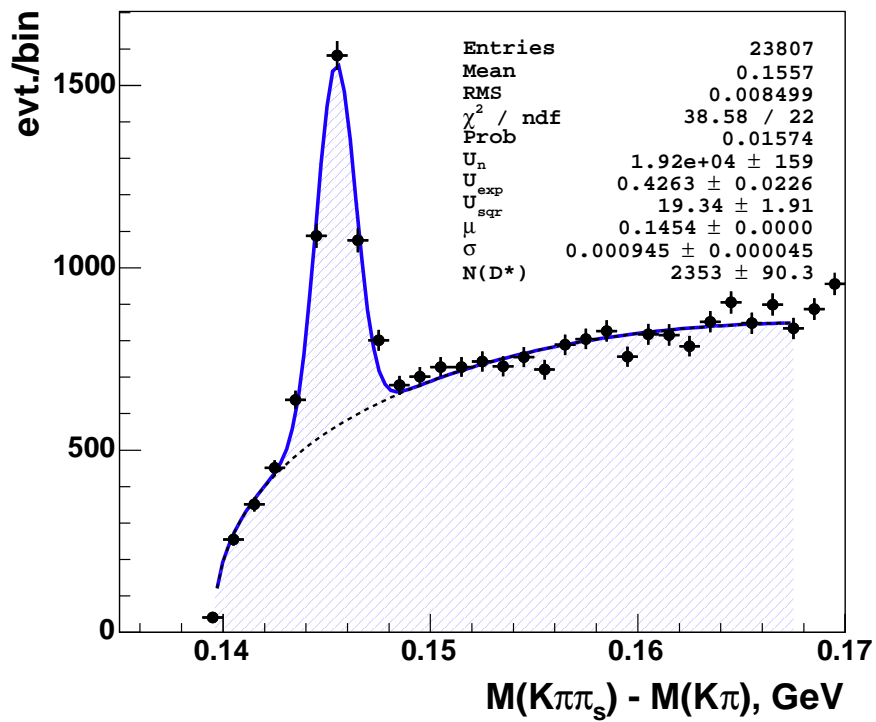


Figure C.1: Distribution of the difference Δm between the invariant mass of the D^* candidate and the D^0 candidate after the DIS selection and trigger requirements for the 1999-2000 data sample.

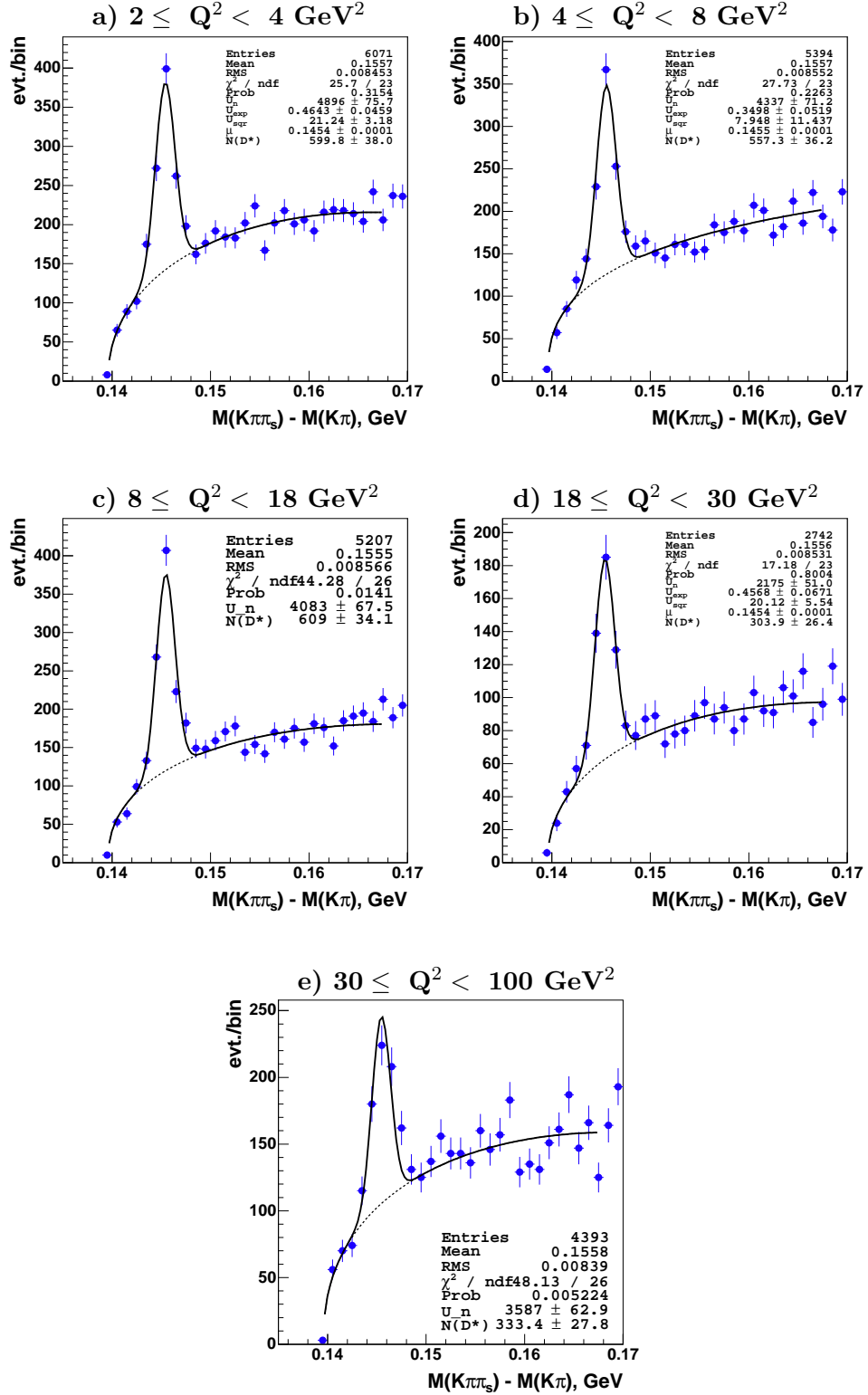


Figure C.2: The individual Δm distributions for the bins in Q^2 . The number of D^* mesons $N(D^*)$ is used for the measurement of the differential cross sections $\sigma(ep \rightarrow e'D^*X)$.

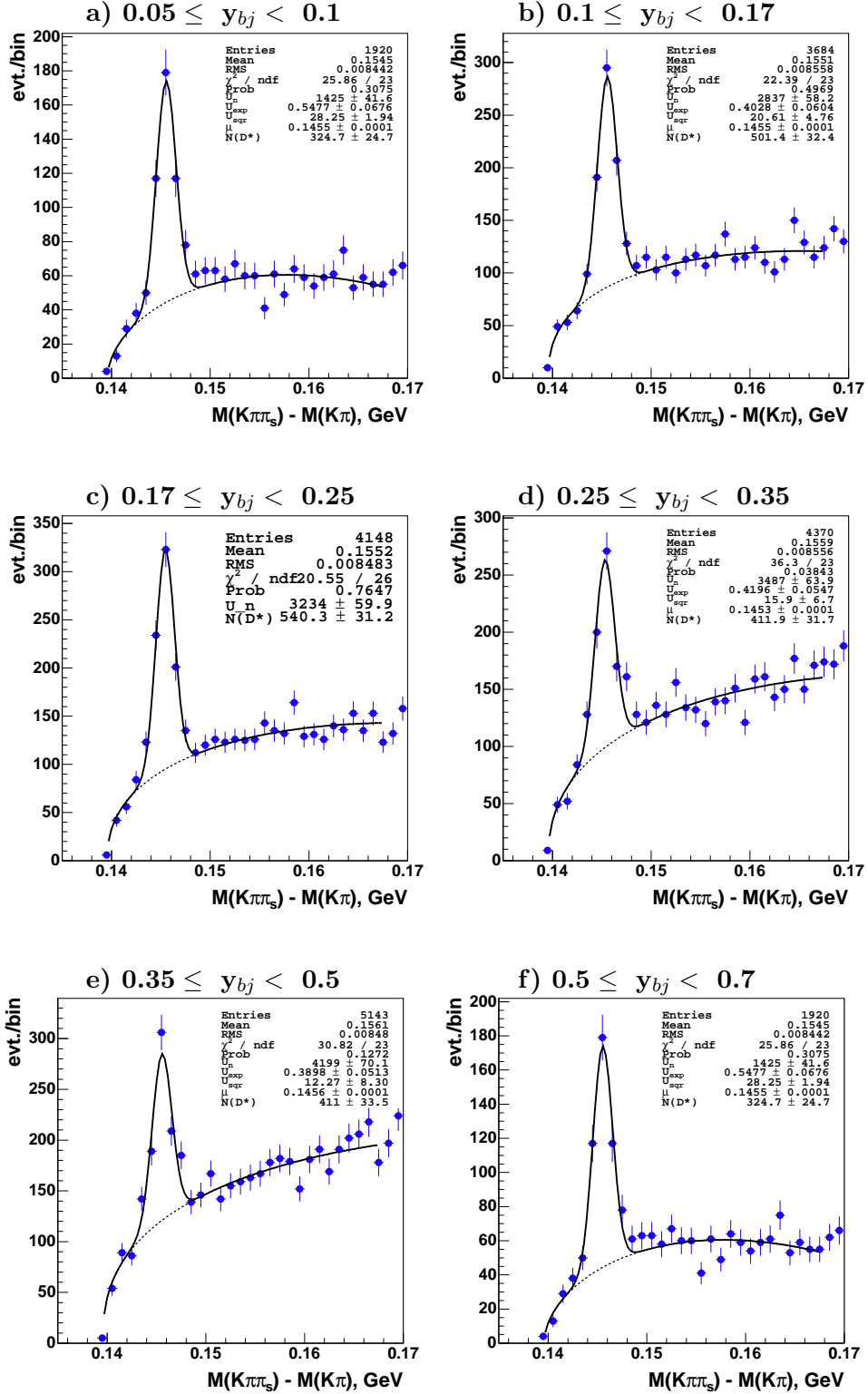


Figure C.3: The individual Δm distributions for the bins in y_{bj} . The number of D^* mesons $N(D^*)$ is used for the measurement of the differential cross sections $\sigma(ep \rightarrow e'D^*X)$.

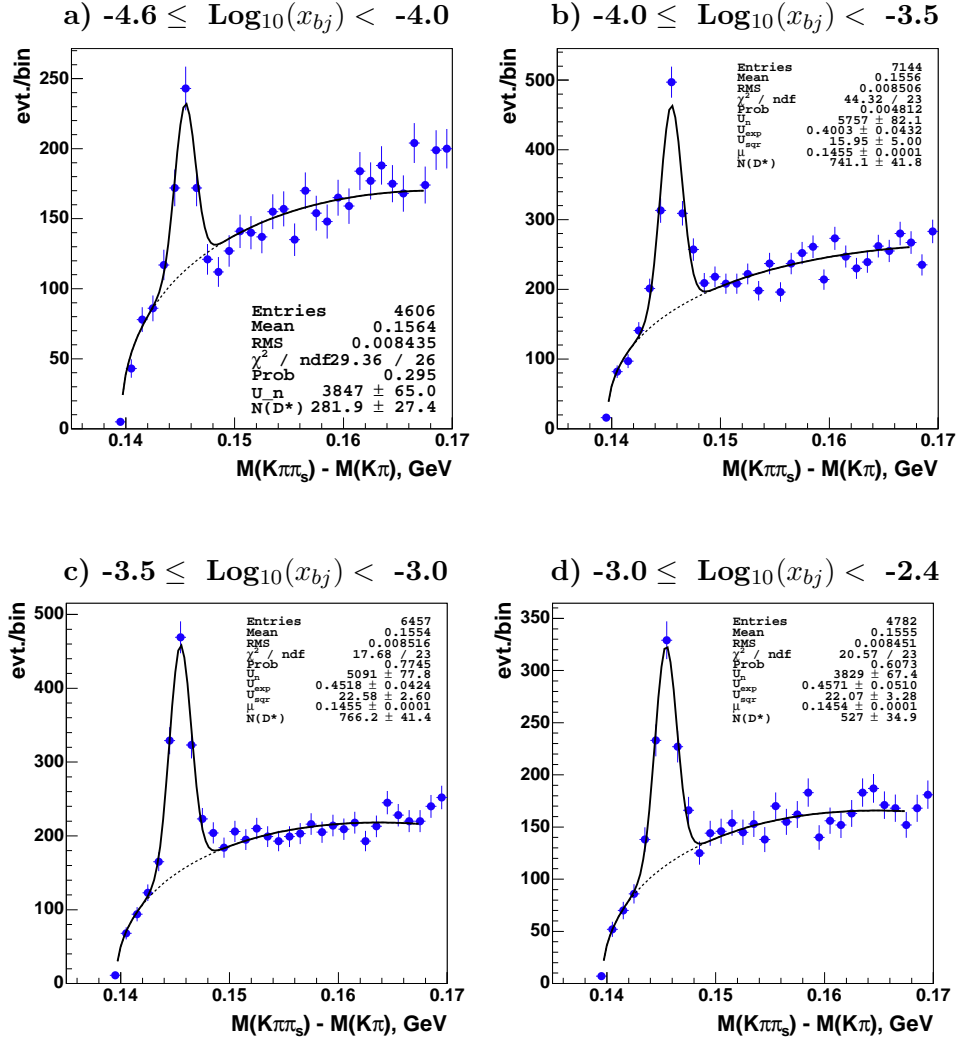


Figure C.4: The individual Δm distributions for the bins in x_{bj} . The number of D^* mesons $N(D^*)$ is used for the measurement of the differential cross sections $\sigma(ep \rightarrow e'D^*X)$.

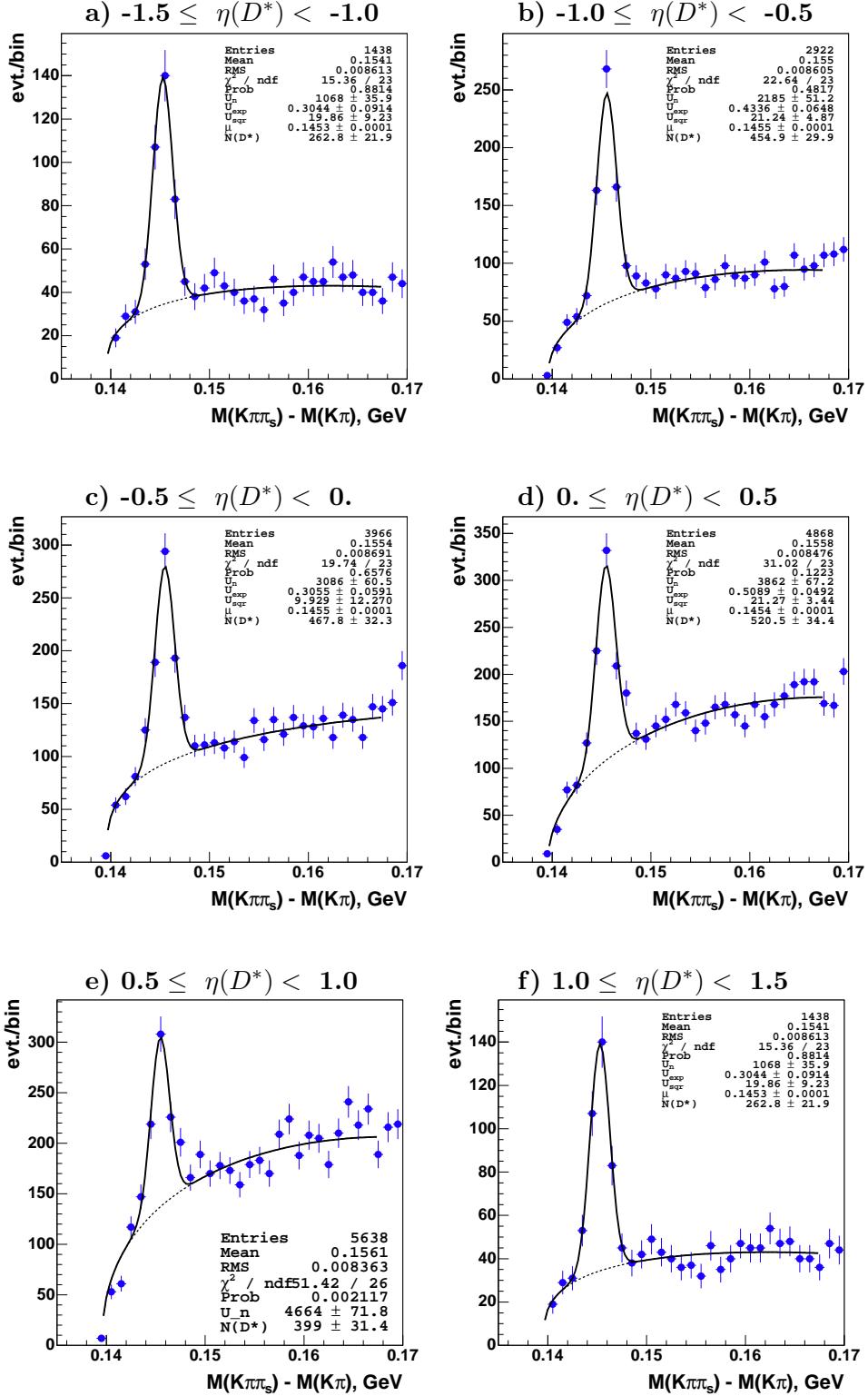


Figure C.5: The individual Δm distributions for the bins in $\eta(D^*)$. The number of D^* mesons $N(D^*)$ is used for the measurement of the differential cross sections $\sigma(ep \rightarrow e'D^*X)$.

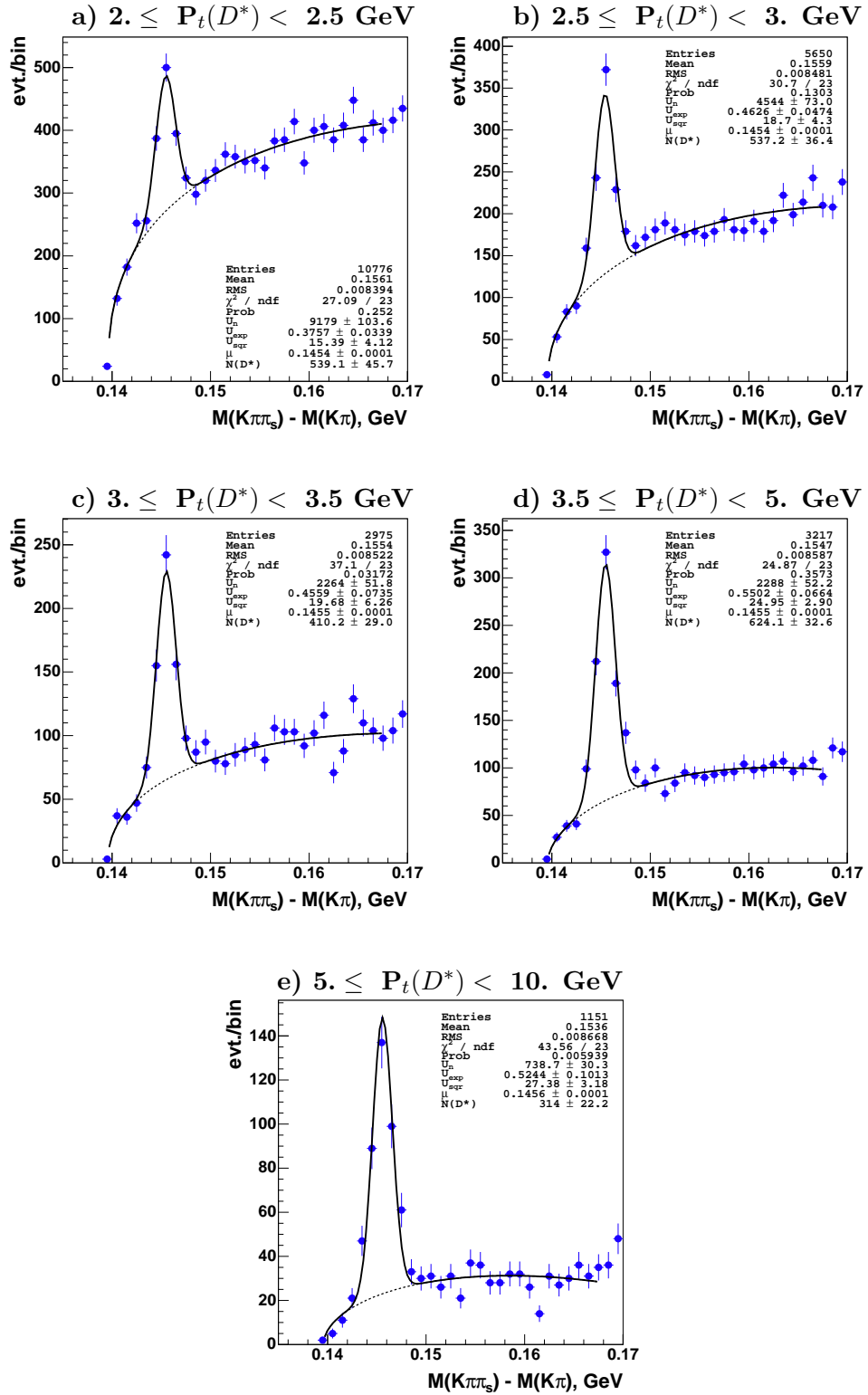


Figure C.6: The individual Δm distributions for the bins in $p_t(D^*)$. The number of D^* mesons $N(D^*)$ is used for the measurement of the differential cross sections $\sigma(ep \rightarrow e'D^*X)$.

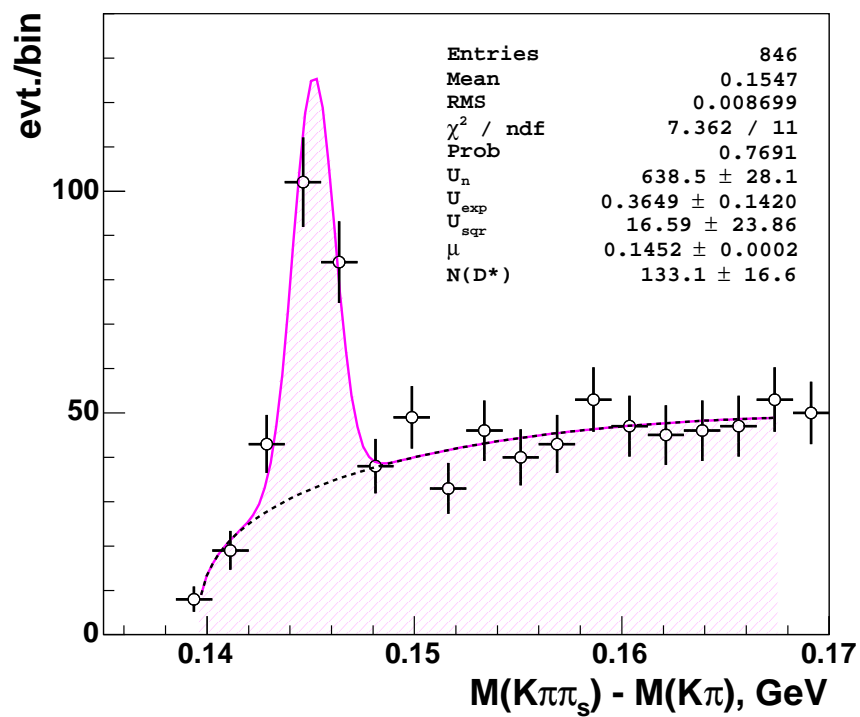


Figure C.7: The total Δm distribution for the 1999-2000 data sample showing the result of the fit for the final diffractive D^* meson selection.

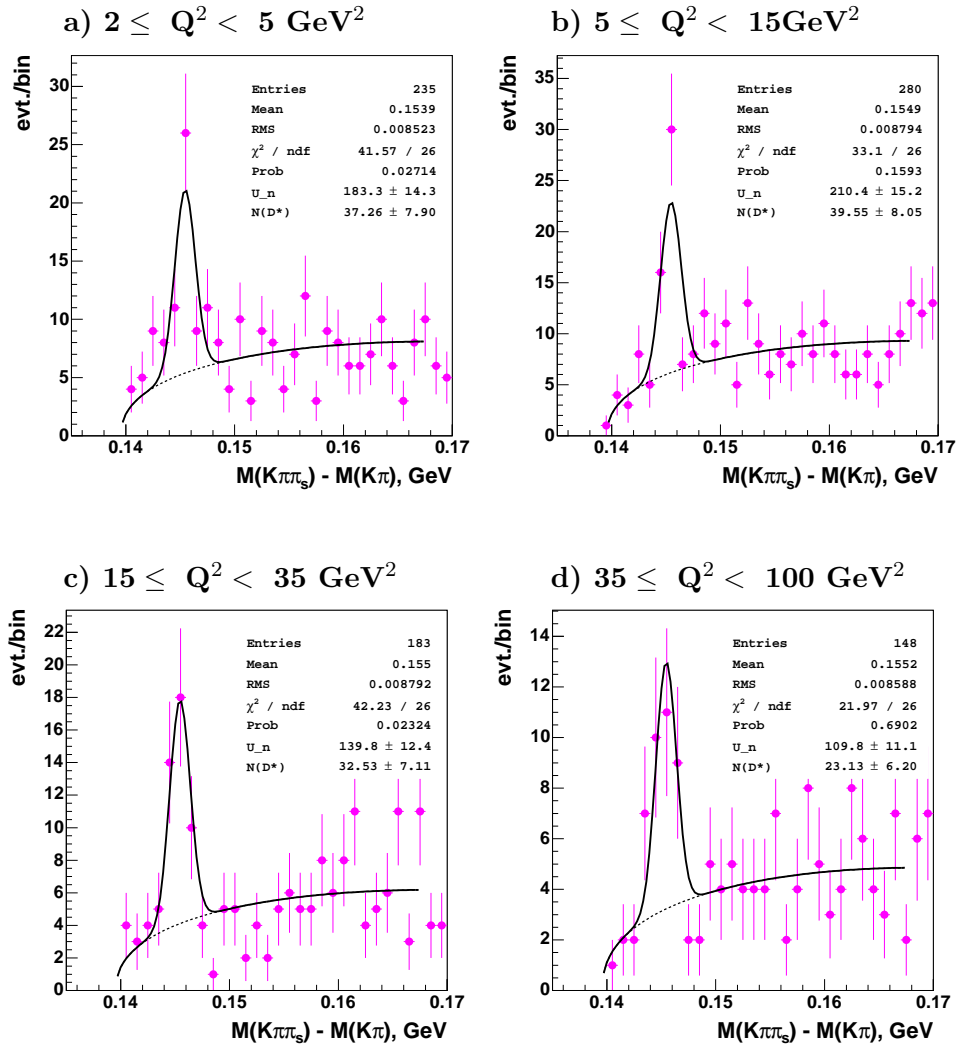


Figure C.8: The individual Δm distributions in the bins of Q^2 . The numbers of D^* mesons are used for the measurement of the differential cross section $\sigma(ep \rightarrow e'(D^*X)Y)$

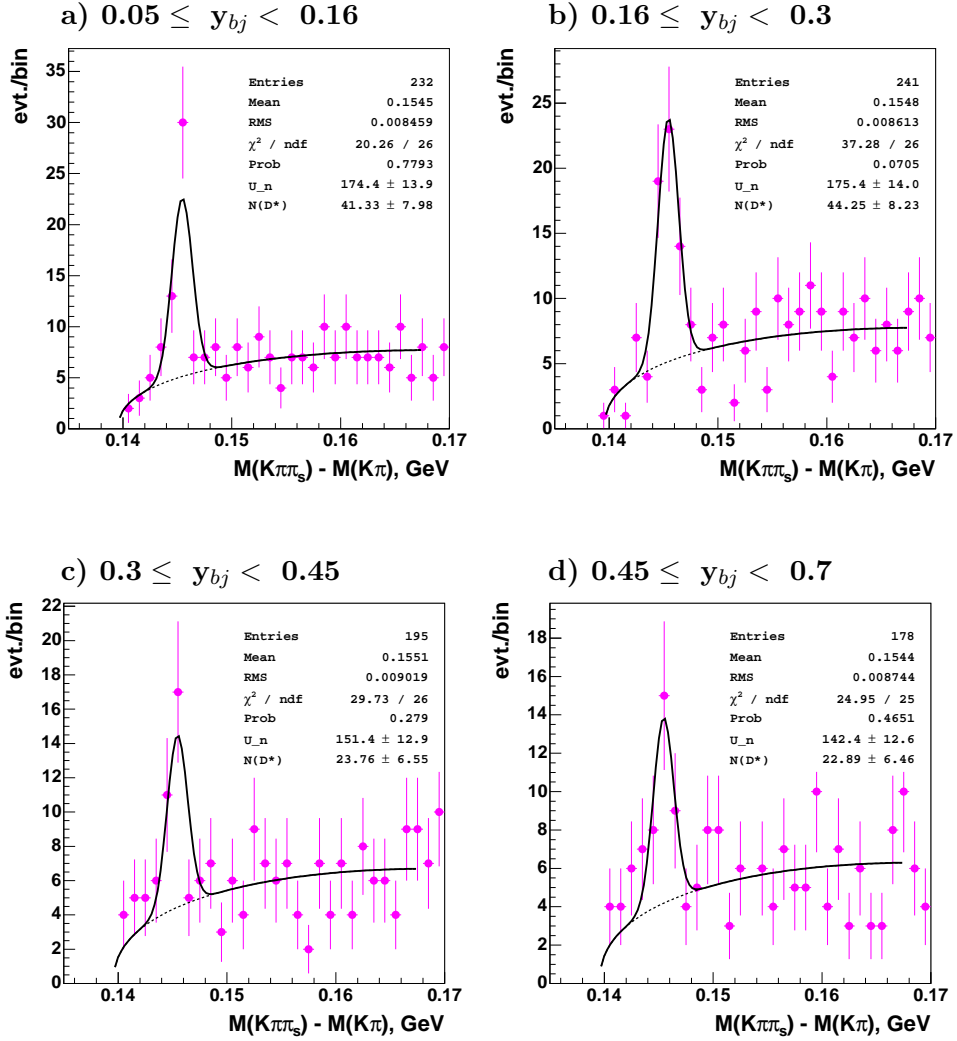


Figure C.9: The individual Δm distributions in the bins of y_{bj} . The numbers of D^* mesons are used for the measurement of the differential cross section $\sigma(ep \rightarrow e'(D^* X)Y)$

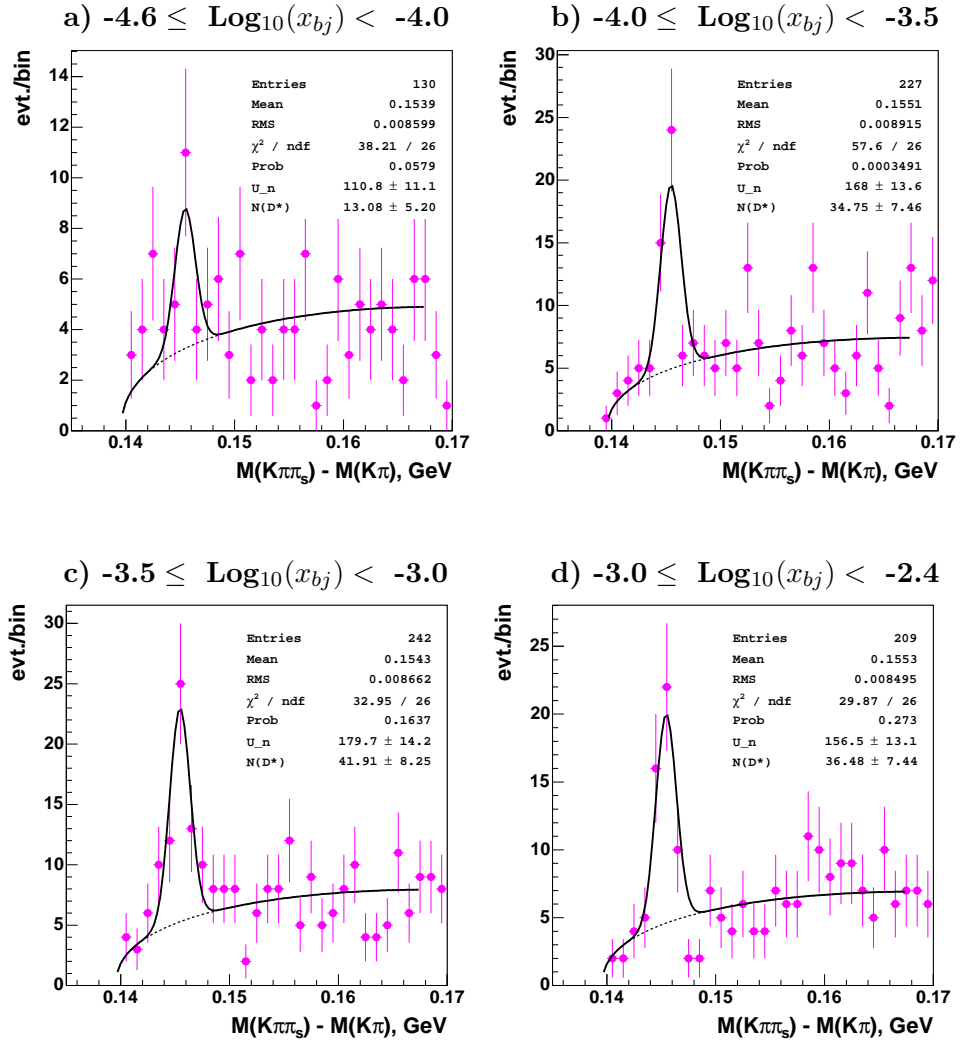


Figure C.10: The individual Δm distributions in the bins of $\text{Log}_{10}(x_{bj})$. The numbers of D^* mesons are used for the measurement of the differential cross section $\sigma(ep \rightarrow e'(D^* X)Y)$

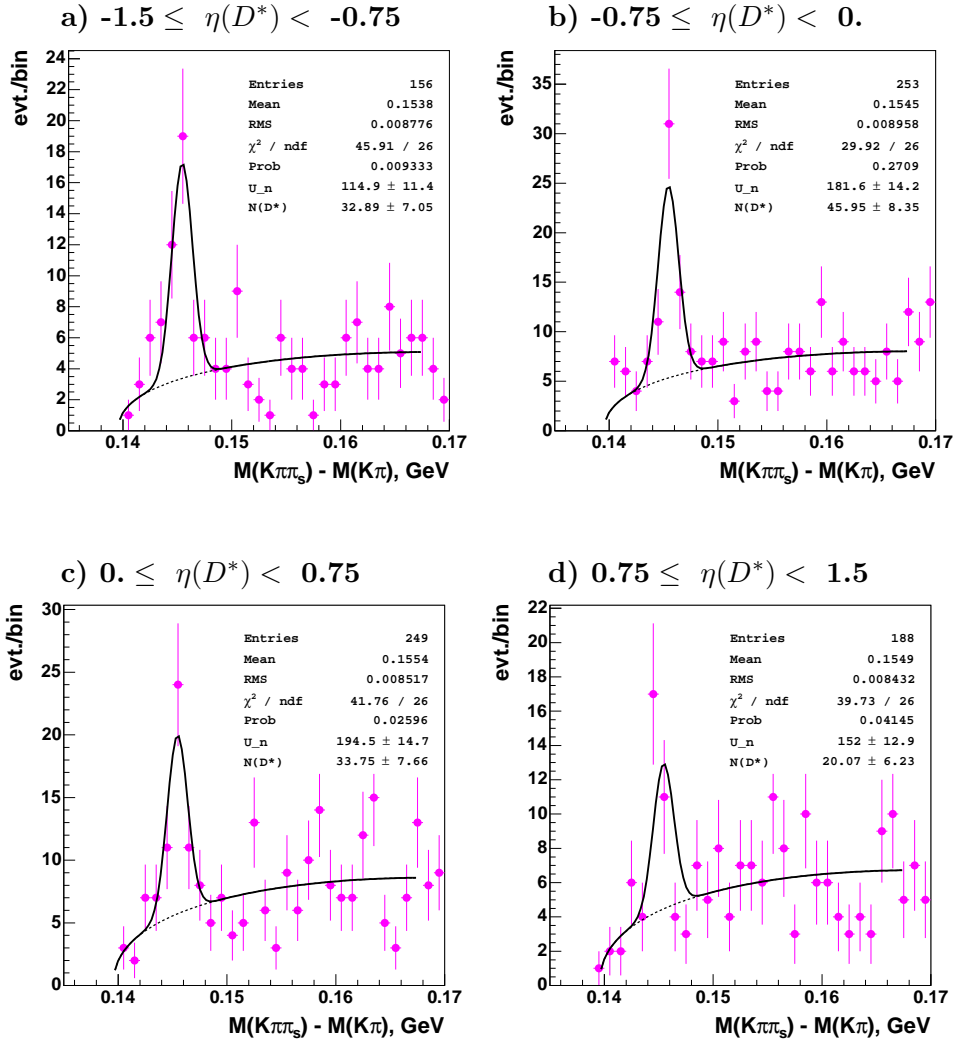


Figure C.11: The individual Δm distributions in the bins of $\eta(D^*)$. The numbers of D^* mesons are used for the measurement of the differential cross section $\sigma(ep \rightarrow e'(D^* X)Y)$

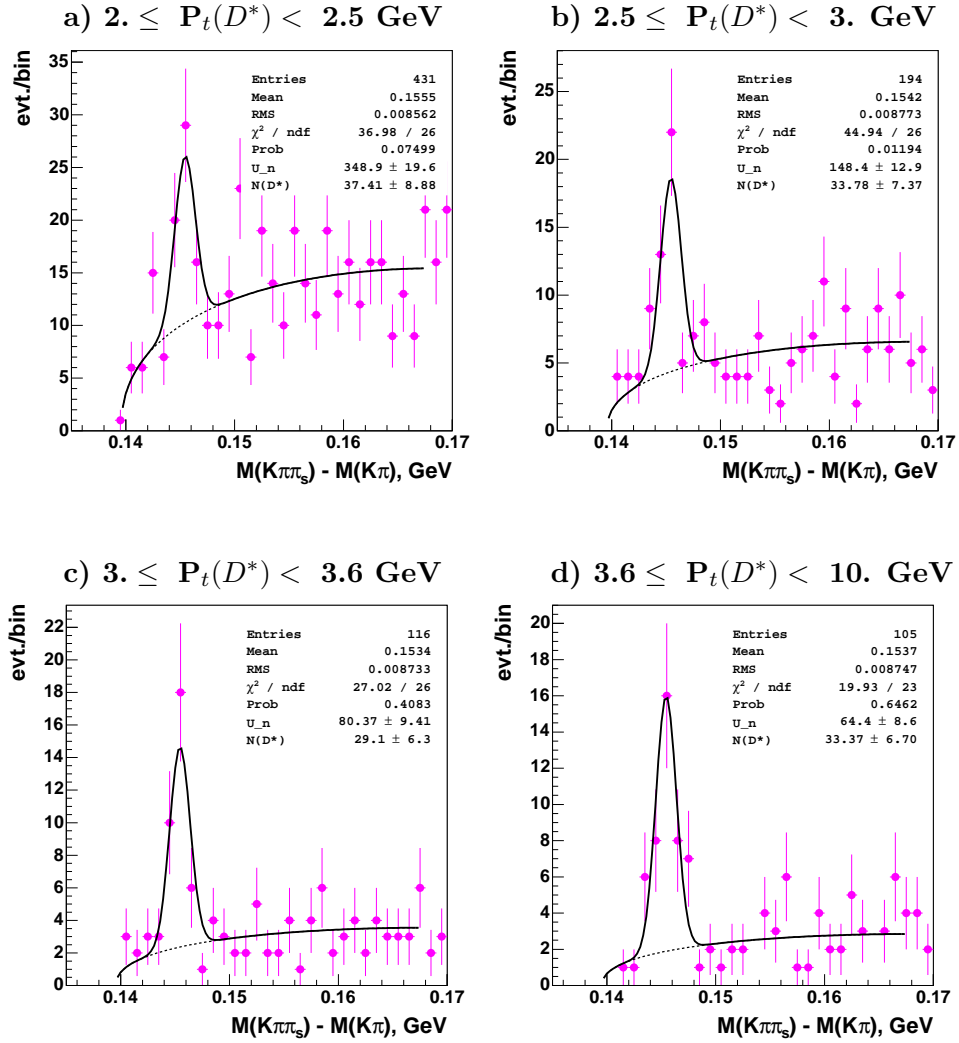


Figure C.12: The individual Δm distributions in the bins of $P_t(D^*)$. The numbers of D^* mesons are used for the measurement of the differential cross section $\sigma(ep \rightarrow e'(D^* X)Y)$

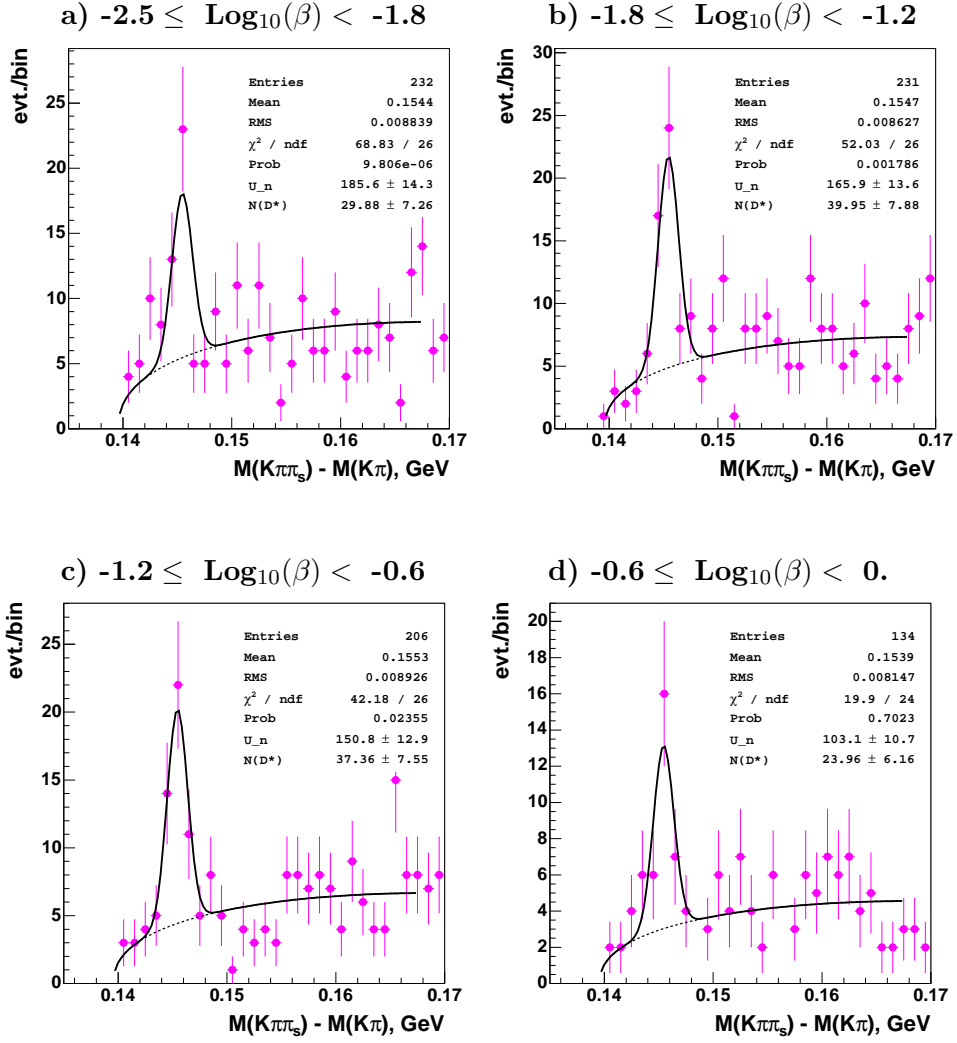


Figure C.13: The individual Δm distributions in the bins of $\text{Log}_{10}(\beta)$. The numbers of D^* mesons are used for the measurement of the differential cross section $\sigma(ep \rightarrow e'(D^* X)Y)$

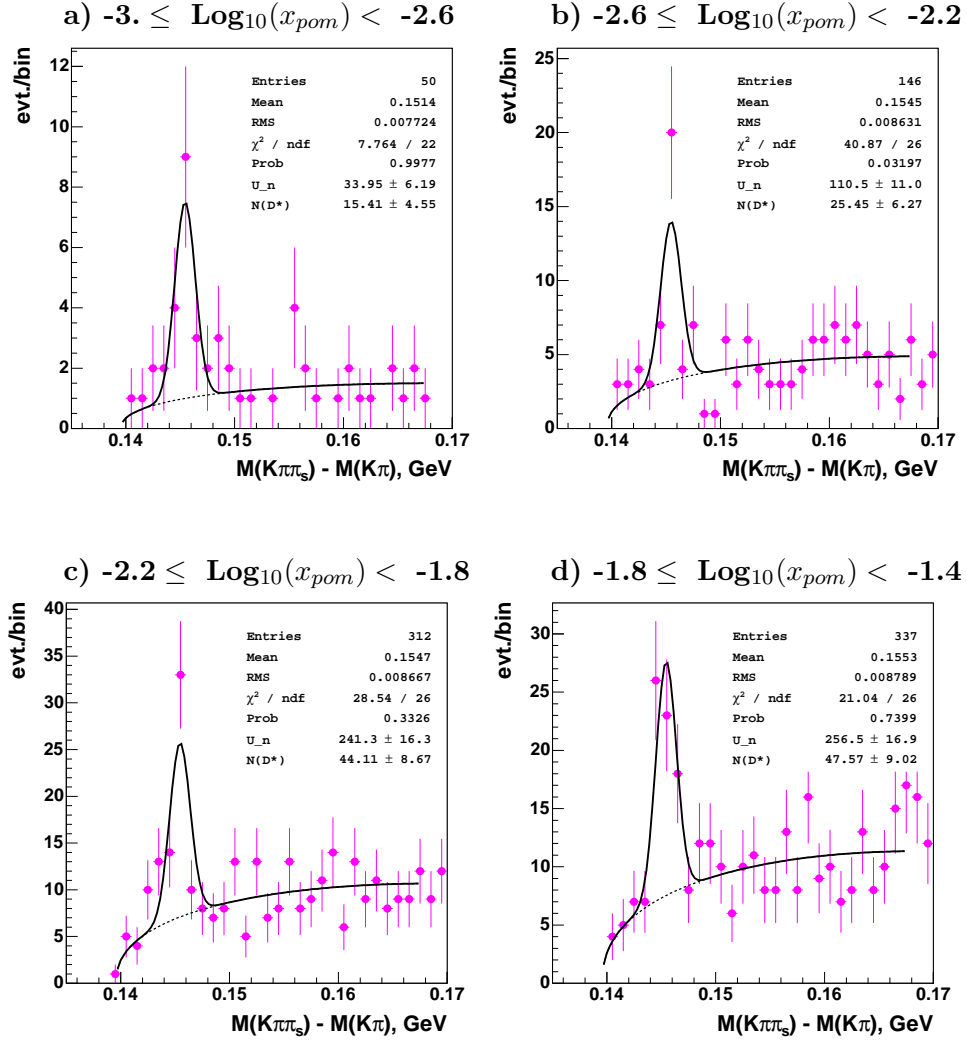


Figure C.14: The individual Δm distributions in the bins of $\text{Log}_{10}(x_{pom})$. The numbers of D^* mesons are used for the measurement of the differential cross section $\sigma(ep \rightarrow e'(D^*X)Y)$

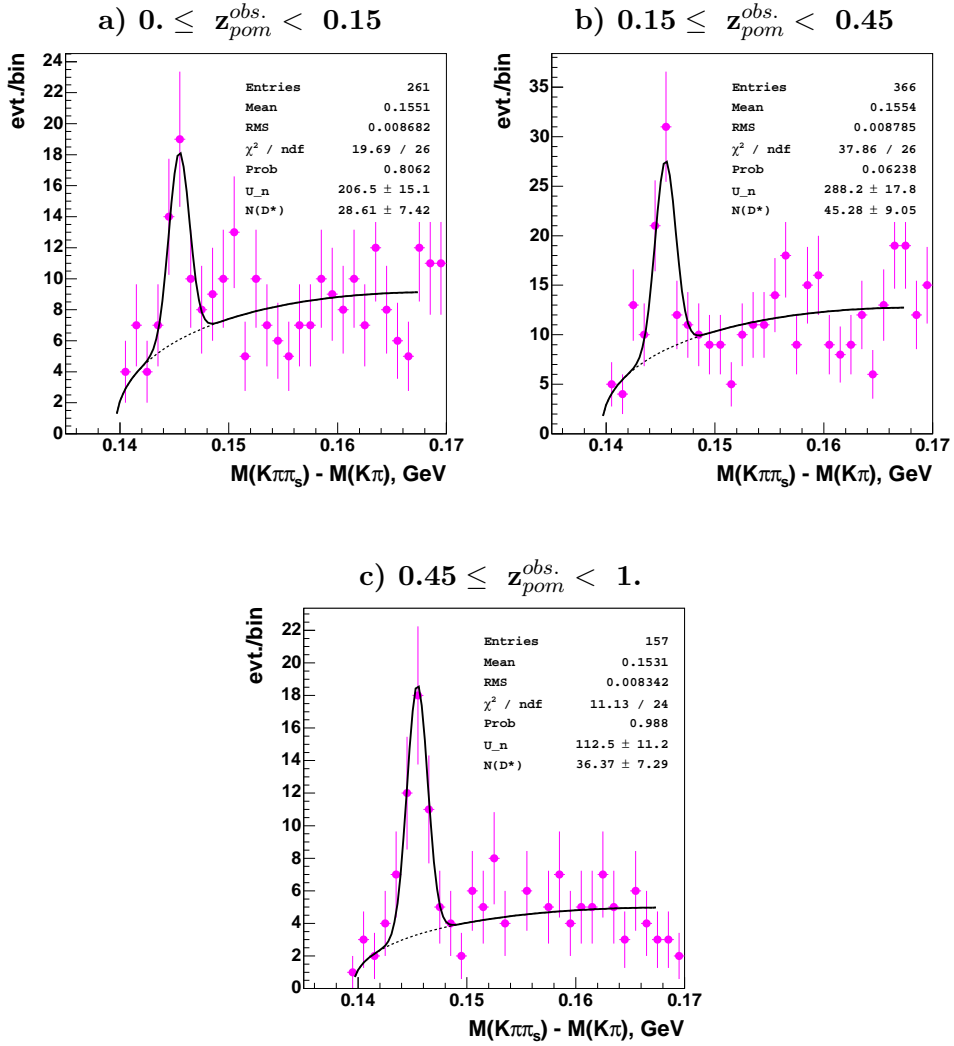


Figure C.15: The individual Δm distributions in the bins of $z_{pom}^{obs.}$. The numbers of D^* mesons are used for the measurement of the differential cross section $\sigma(ep \rightarrow e'(D^*X)Y)$

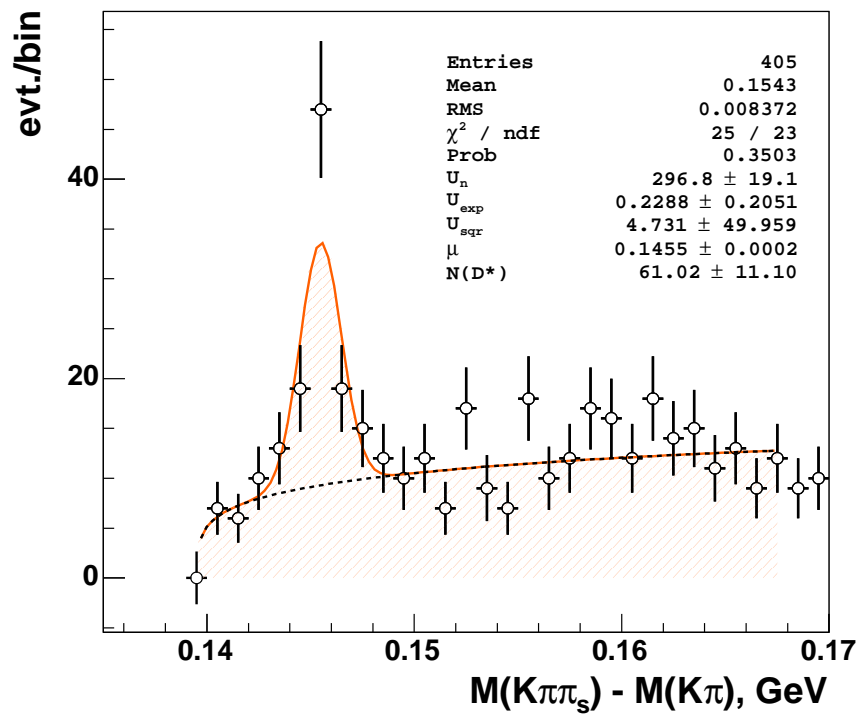


Figure C.16: The complete Δm distribution for the 1999-2000 data sample showing the result of the fit for the final diffractive D^* meson selection in DIS. The low $x_P < 0.01$ cut is additionally applied.

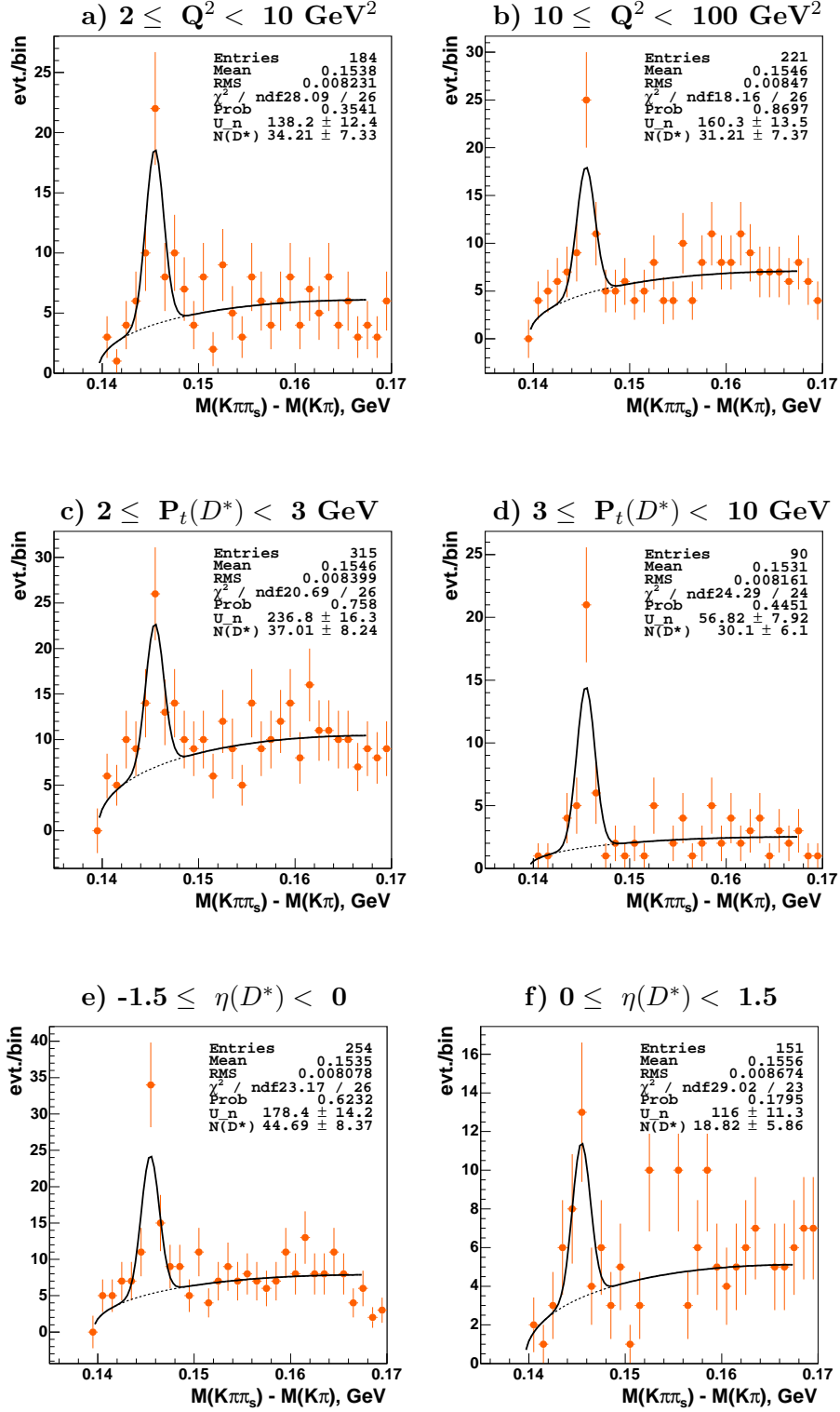


Figure C.17: The mass difference signals in bins of Q^2 (a-b), $P_t(D^*)$ (c-d) and $\eta(D^*)$ (e-f) are shown for the diffractive DIS sample. In addition the cut for the low kinematic region of $x_P < 0.01$ is applied.

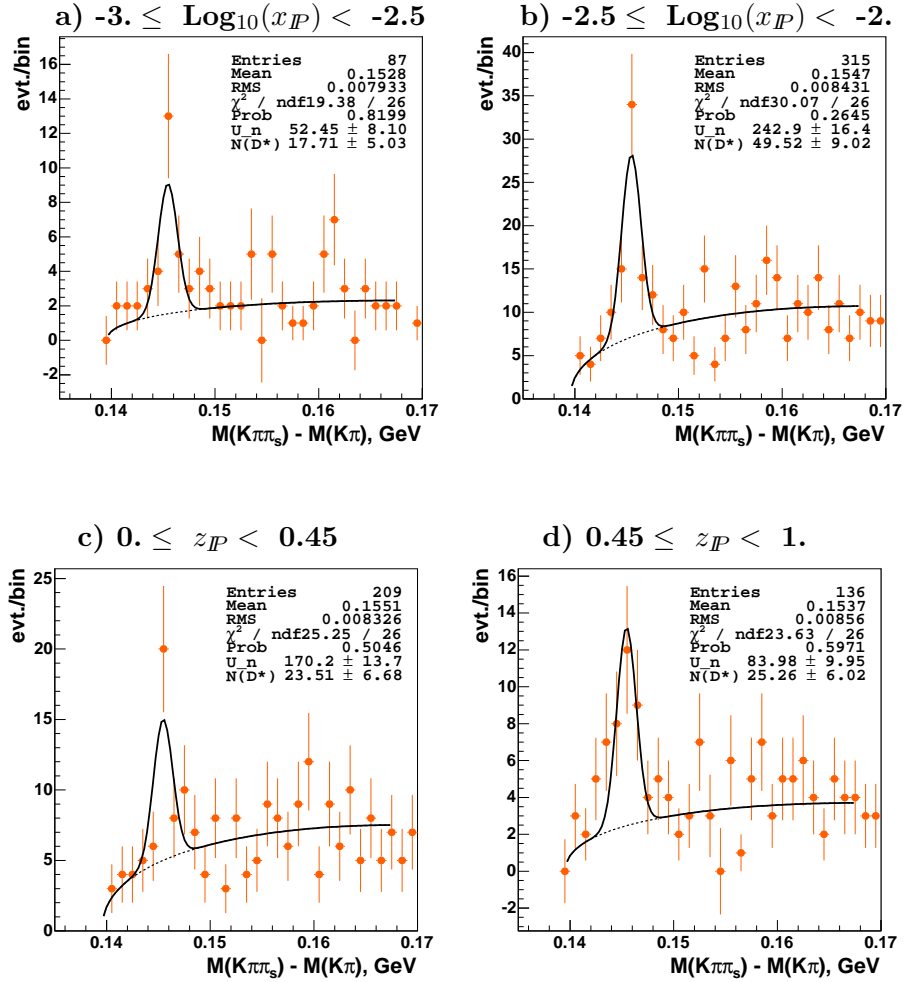


Figure C.18: The mass difference signals in bins of $\text{Log}_{10}(x_P)$ (a-b), and z_P (c-d) are shown for the diffractive DIS sample with the additional cut $x_P < 0.01$.

Appendix D

Unintegrated Gluon Densities

Measured in this thesis diffractive cross sections were compared to the two different theoretical models of diffraction. One of them was two-gluon exchange (see Section 2.9). As introduced in Section 2.9 the two gluon exchange model employs perturbative QCD techniques and provides a direct access to the gluon distribution function [22]. The cross section is proportional to the gluon density squared in the proton. In this analysis two different fits of the unintegrated gluon density obtained from CCFM evolution to HERA $F_2(x, Q^2)$ data are used for the theory comparison. In the following parametrisations of these fits are summarised.

The general form of the integral equation for the parton evolution is [55, 56]

$$x\mathcal{A}(x, k_t, \bar{q}) = x\mathcal{A}_0(x, k_t, \bar{q}) + \int \frac{dz}{z} \int \frac{dq^2}{q^2} \Theta(\text{order}) \Delta_s \tilde{P}(z, q, k_t) x\mathcal{A}\left(\frac{x}{z}, k'_t, q\right) \quad (\text{D.1})$$

where \bar{q} represents the factorisation scale and $\Theta(\text{order})$ is responding for the ordering condition of the evolution. The first component of this equation reflects the contribution of non-resolvable branchings between the starting scale and factorisation scale. The details of the QCD evolution is describing in the second part of Equation D.1 by the splitting function \tilde{P} with parton density and the Sudakov form factor Δ_s .

The starting distribution is parametrised as

$$x\mathcal{A}_0(x, k_t, Q_0) = Nx^{p_0}(1-x)^{p_1} \cdot \exp(-k_t^2/k_0^2) \quad (\text{D.2})$$

where p_0 and p_1 are experimentally determined parameters and N represent a normalisation constant.

The CCFM evolution equations have been solved numerically using a Monte Carlo method [57]. Figure D.1 presents the comparison of the different sets of un-integrated gluon densities obtained from the CCFM evolution.

In this thesis **J2003 set 1** and **J2003 set 2** [55] were investigated. Results are shown in Figures D.2 and D.3, where the cross sections for the BJLKW model of the perturbative two-gluon approach, which are obtained using **J2003 set 1** and **J2003 set 2** un-integrated gluon densities respectively are presented.

The prediction of the BJLKW model for the $q\bar{q}g$ process can be tuned using the lower

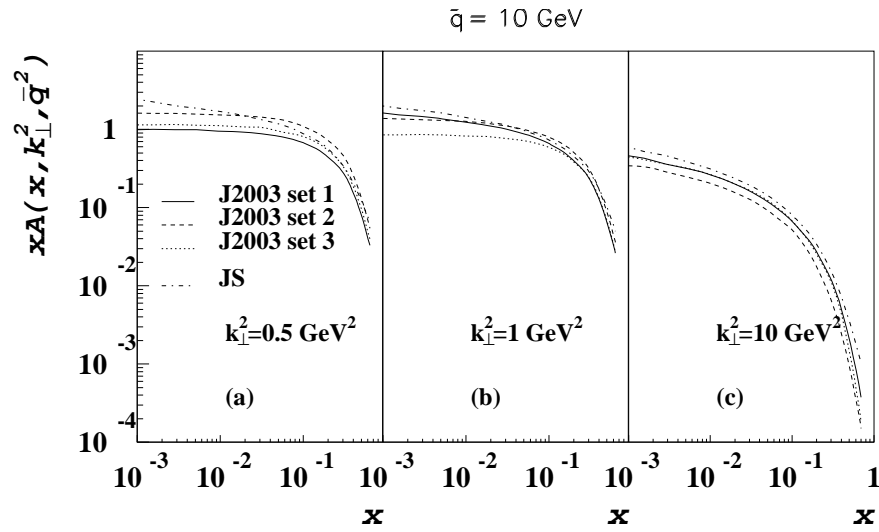


Figure D.1: Comparison of the different sets of unintegrated gluon densities obtained from the CCFM evolution (from [55]) is presented. The unintegrated gluon densities are shown as a function of x .

cut-off on the transverse momentum of the final state gluon. Figures D.2 and D.3 present the results of this *tuning* for the four different cuts on the transverse momentum of the final state gluon. The best description of the diffractive data with $x_P < 0.01$ can be reached using the *J2003 set 2* unintegrated PDFs with the cut-off on the gluon $p_{t,g} > 1.5$ GeV.

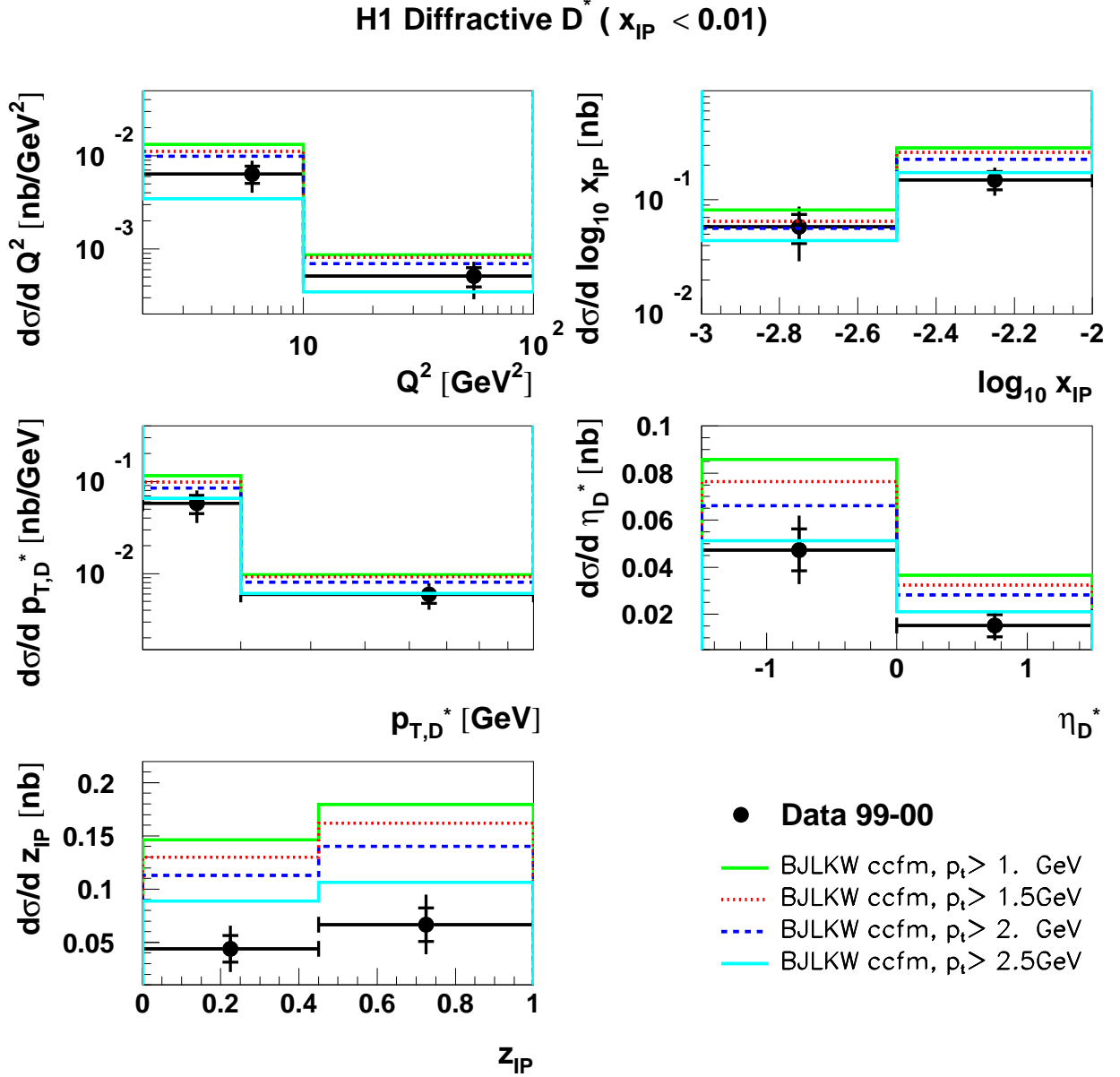


Figure D.2: Cross sections for diffractive D^* meson production in DIS in the low kinematic region of $x_{\mathbb{P}} < 0.01$ are shown differentially as a function of (a) Q^2 , (b) $x_{\mathbb{P}}$, (c) $P_t(D^*)$, (d) $\eta(D^*)$ and (e) $z_{\mathbb{P}}$. The data are shown as points with error bars (inner - statistical, outer - total). Data are compared with a prediction from the perturbative 2-gluon approach of BJKLW using the unintegrated gluon density. **J2003 set 2** of the unintegrated gluon densities is used. Predictions for the four different p_t cuts of the gluon in the $c\bar{c}g$ process are presented for comparison.

H1 Diffractive D^* ($x_{\mathcal{P}} < 0.01$)

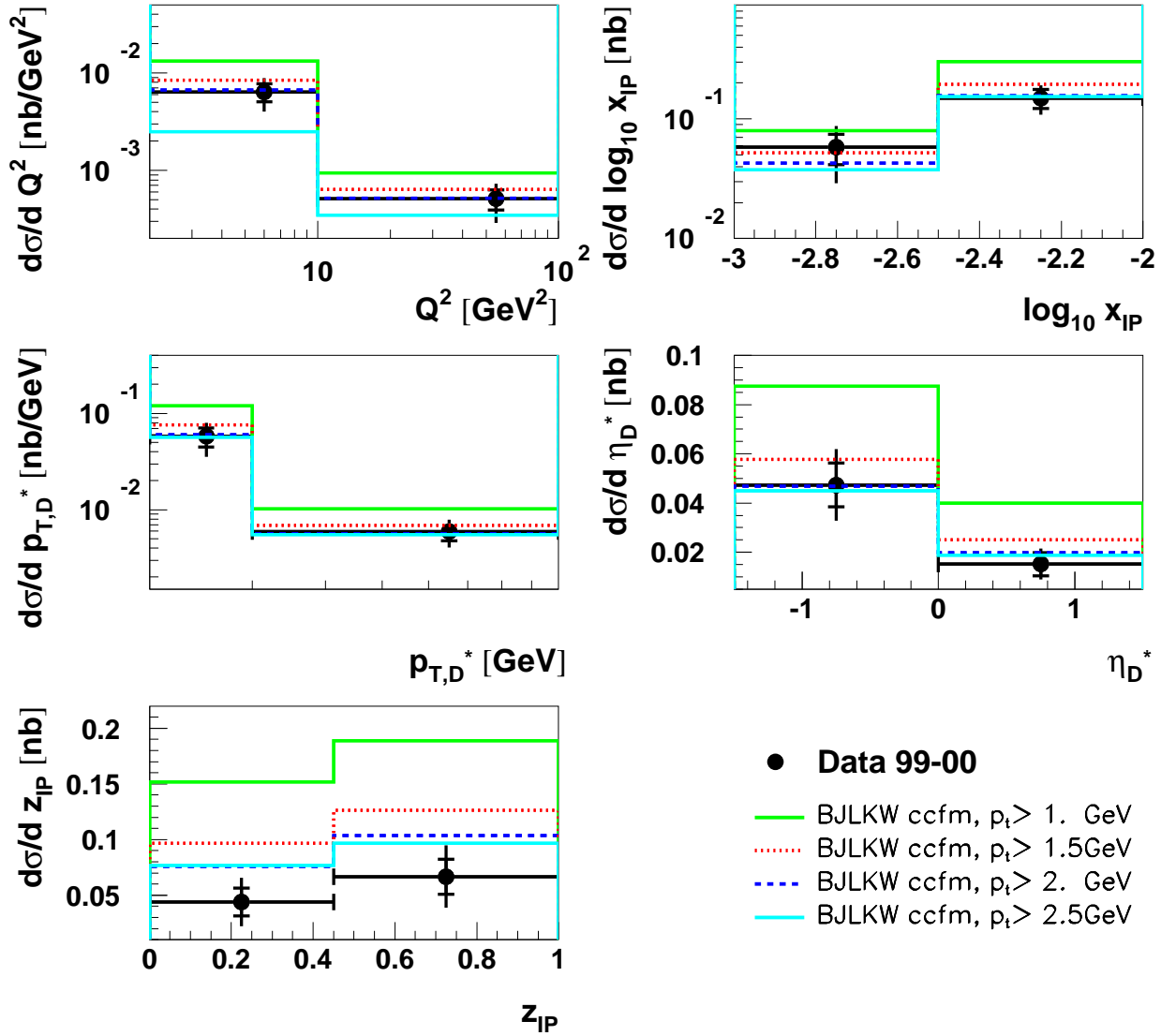


Figure D.3: Cross sections for diffractive D^* meson production in DIS in the low kinematic region of $x_{\mathcal{P}} < 0.01$ are shown differentially as a function of (a) Q^2 , (b) $x_{\mathcal{P}}$, (c) $P_t(D^*)$, (d) $\eta(D^*)$ and (e) $z_{\mathcal{P}}$. The data are shown as points with error bars (inner - statistical, outer - total). Data are compared with a prediction from the perturbative 2-gluon approach of BJKLW using the unintegrated gluon density. J2003 set 1 of the unintegrated gluon densities is used. Predictions for the four different p_t cuts of the gluon in the $c\bar{c}g$ process are compared.

Bibliography

- [1] V. Gribov, L. Lipatov, *Sov. J. Nucl. Phys.* **15** (1972) 438 and 675.
- [2] L. Lipatov, *Sov. J. Nucl. Phys.* **20** (1975) 94.
- [3] G. Altarelli, G. Parisi, *Nucl. Phys.* **B 126** (1977) 298.
- [4] Y. Dokshitzer, *Sov. Phys. JETP* **46** (1977) 641.
- [5] E. Kuraev, L. Lipatov, V. Fadin, *Sov. Phys. JETP* **44** (1976) 443.
- [6] E. Kuraev, L. Lipatov, V. Fadin, *Sov. Phys. JETP* **45** (1977) 199.
- [7] Y. Balitsky, L. Lipatov, *Sov. J. Nucl. Phys.* **28** (1978) 822.
- [8] M. Ciafaloni, *Nucl. Phys.* **B 296** (1988) 49.
- [9] S. Catani, F. Fiorani, G. Marchesini, *Phys. Lett.* **B 234** (1990) 339.
- [10] S. Catani, F. Fiorani, G. Marchesini, *Nucl. Phys.* **B 336** (1990) 18.
- [11] G. Marchesini, *Nucl. Phys.* **B 445** (1995) 49.
- [12] B. Andersson, G. Gustafson, G. Ingelman, T. Sjöstrand, *Phys. Rept.*, 97 (1983) 31.
- [13] C. Peterson, D. Schlatter, I. Schmitt, P. Zerwas, *Phys. Rev.*, D27 (1983) 105.
- [14] T. Regge, *Nuovo Cimento*, 14 (1959) 951.
- [15] T. Regge, *Nuovo Cimento*, 18 (1960) 947.
- [16] P. Collins, *An Introduction to the Regge Theory and High Energy Physics*, Cambridge, 1977.
- [17] H1 Collaboration, Measurement of the Diffractive Deep-Inelastic Scattering Cross Section at low Q^2 , H1 Preliminary, H1prelim-112/2002.
- [18] J. C. Collins, Proof of Factorization for Diffractive Hard Scattering, *Phys. Rev.*, D57:3051-3056, 1998.
- [19] G. Ingelman, P. Schlein, *Phys. Lett.* **B152** (1985) 256.
- [20] C. Adloff *et al.*, Measurement and NLO DGLAP QCD Interpretation of Diffractive Deep-Inelastic Scattering at HERA, H1 internal note, 2002, Amsterdam (ICHEP 2002), Abstract 980.

- [21] A. Aktas *et al.*, Measurement and QCD Analysis of the Diffractive Deep-Inelastic Scattering Cross Section at HERA, H1 internal note, 2006, hep-ex/0606004.
- [22] H.Jung, Monte Carlo Implementations of Diffraction at HERA, DESY 98-131.
- [23] M. Diehl, *Z. Phys.*, C 76, 499(1997), hep-ex/9610430.
- [24] M. Wusthoff, Photon diffractive dissociation in deep inelastic scattering, DESY-1995-166.
- [25] J. Bartels, H. Jung, A. Kyrieleis, *European Physical Journal C* **24** (2002) 555.
- [26] J. Bartels, C. Ewerz, H. Lotter, M. Wuesthof, **386** (1996) 389.
- [27] S. Brodsky, R. Enberg, P. Hoyer, G. Ingelman, hep-ph-0409119.
- [28] J. L. Augneres *et al.*, HERA, A Proposal for a Large Electron-Proton Colliding Beam Facility at DESY, 1981, DESY 81-10.
- [29] I. Abt *et al.*, *Nucl. Instrum. Meth.*, The H1 Detector at HERA, 1997, A386, 310-347.
- [30] I. Abt *et al.*, *Nucl. Instrum. Meth.*, The Tracking, Calorimeter and Muon Detectors of the H1 Experiment at HERA, 1997, A386, 348-396.
- [31] B. Andrieu *et al.* [H1 Calorimeter Group] *Nucl. Instrum. Meth.*, Beam tests and calibration of the H1 liquid argon calorimeter with electrons, **A350** (1994) 57.
- [32] B. Andrieu *et al.* [H1 Calorimeter Group] *Nucl. Instrum. Meth.*, Results from pion calibration runs for the H1 liquid argon calorimeter and comparisons with simulations, **A336** (1993) 499.
- [33] R. D. Appuhn *et al.* [H1 SPACAL Group], *Nucl. Instrum. Meth.*, **A386** (1997) 397.
- [34] R. D. Appuhn *et al.* [H1 SPACAL Group], *Nucl. Instrum. Meth.*, **A374** (1996) 149.
- [35] E. Panaro, Energy measurements in e-p collisions at HERA using the PLUG calorimeter of the H1 Experiment, DESY-THESIS-1998-020.
- [36] H1-Collaboration, Luminosity Measurement in the H1 Experiment at HERA, ICHEP'96, Warsaw, Abstract pal7-026.
- [37] H. Beck, Principles and Operation of the z-Vertex Trigger, H1 internal note, 1996, H1-05/96-479.
- [38] T. Wolff *et al.*, Track Finder for the First Level Trigger of H1, H1 internal note, 1992, H1-02/92-213.
- [39] J. Reidberger, The H1 Trigger with Emphasis on Tracking Triggers, H1 internal note, 1995, H1-01/95-419.
- [40] H. Jung, The RAPGAP Monte Carlo for Deep Inelastic Scattering Version 3.1., 2005, <http://www.desy.de/~jung/rapgap/rapgap31021.ps.gz>.

- [41] B. List, A. Mastroberardino, DIFFVM: A Monte Carlo generator for diffractive processes in e p scattering, Prepared for Workshop on Monte Carlo Generators for HERA Physics, Germany, 27-30 Apr 1998.
- [42] Y. Akimov *et al.*, *Phys. Rev.*, **D14** (1976) 3148.
- [43] K. Goulianos, *Phys. Rep.*, **101-3** (1983) 169.
- [44] U. Bassler, G. Bernardi, Structure Function Measurements and Kinematic Reconstruction at HERA, 1997, DESY-97-137.
- [45] L. Gladilin, Charm hadron production fractions, 1999, hep-ex/9912064.
- [46] S. Eidelman *et al.* (Particle Data Group), *Phys. Lett.*, **B592** (2004) 1.
- [47] G. Flucke, Photoproduction of D* mesons and D* mesons associated with jets at HERA, DESY-THESIS-2005-006.
- [48] F. P. Schilling, Diffractive jet production in deep-inelastic e+ p collisions at HERA, DESY-THESIS-2001-010.
- [49] P. Thompson, Open Charm Production in Inclusive and Diffractive Deep-Inelastic Scattering at HERA, 1999, Univ. Birmingham.
- [50] H1 Collaboration, Diffractive Deep-Inelastic Scattering with a Leading Proton at HERA, 2006, DESY 06-048.
- [51] S. Schmidt, Measurement of charm induced dijet events in deep-inelastic e p scattering with the H1 detector at HERA, (In German), DESY-THESIS-2004-043.
- [52] S. Hengstmann, A Measurement of the Diffractive Charm Production at HERA, DESY-THESIS-2000-215.
- [53] H1 Collaboration, ELAN Working Group, internal communication, 2000.
- [54] P. Thompson, *Nucl. Phys. Proc. Suppl.* **82** (2000) 274.
- [55] M. Hansson, H. Jung, The status of CCFM unintegrated gluon densities, in *DIS 2003, XI International Workshop on Deep Inelastic Scattering, St. Petersburg, Russia* (2003), hep-ph/0309009.
- [56] H. Jung, Un-integrated PDFs in CCFM, in *DIS 2004, XII International Workshop on Deep Inelastic Scattering, Strbske Pleso, Slovakia* (2004), hep-ph/0411287.
- [57] H. Jung, G. Salam, *Eur. Phys. J. C* **19** (2001) 351, hep-ph/0012143.

Bibliography

- [1] V. Gribov, L. Lipatov, *Sov. J. Nucl. Phys.* **15** (1972) 438 and 675.
- [2] L. Lipatov, *Sov. J. Nucl. Phys.* **20** (1975) 94.
- [3] G. Altarelli, G. Parisi, *Nucl. Phys.* **B 126** (1977) 298.
- [4] Y. Dokshitzer, *Sov. Phys. JETP* **46** (1977) 641.
- [5] E. Kuraev, L. Lipatov, V. Fadin, *Sov. Phys. JETP* **44** (1976) 443.
- [6] E. Kuraev, L. Lipatov, V. Fadin, *Sov. Phys. JETP* **45** (1977) 199.
- [7] Y. Balitsky, L. Lipatov, *Sov. J. Nucl. Phys.* **28** (1978) 822.
- [8] M. Ciafaloni, *Nucl. Phys.* **B 296** (1988) 49.
- [9] S. Catani, F. Fiorani, G. Marchesini, *Phys. Lett.* **B 234** (1990) 339.
- [10] S. Catani, F. Fiorani, G. Marchesini, *Nucl. Phys.* **B 336** (1990) 18.
- [11] G. Marchesini, *Nucl. Phys.* **B 445** (1995) 49.
- [12] B. Andersson, G. Gustafson, G. Ingelman, T. Sjöstrand, *Phys. Rept.*, 97 (1983) 31.
- [13] C. Peterson, D. Schlatter, I. Schmitt, P. Zerwas, *Phys. Rev.*, D27 (1983) 105.
- [14] T. Regge, *Nuovo Cimento*, 14 (1959) 951.
- [15] T. Regge, *Nuovo Cimento*, 18 (1960) 947.
- [16] P. Collins, *An Introduction to the Regge Theory and High Energy Physics*, Cambridge, 1977.
- [17] H1 Collaboration, Measurement of the Diffractive Deep-Inelastic Scattering Cross Section at low Q^2 , H1 Preliminary, H1prelim-112/2002.
- [18] J. C. Collins, Proof of Factorization for Diffractive Hard Scattering, *Phys. Rev.*, D57:3051-3056, 1998.
- [19] G. Ingelman, P. Schlein, *Phys. Lett.* **B152** (1985) 256.
- [20] C. Adloff *et al.*, Measurement and NLO DGLAP QCD Interpretation of Diffractive Deep-Inelastic Scattering at HERA, H1 internal note, 2002, Amsterdam (ICHEP 2002), Abstract 980.

- [21] A. Aktas *et al.*, Measurement and QCD Analysis of the Diffractive Deep-Inelastic Scattering Cross Section at HERA, H1 internal note, 2006, hep-ex/0606004.
- [22] H.Jung, Monte Carlo Implementations of Diffraction at HERA, DESY 98-131.
- [23] M. Diehl, *Z. Phys., C* **76**, 499(1997), hep-ex/9610430.
- [24] M. Wusthoff, Photon diffractive dissociation in deep inelastic scattering, DESY-1995-166.
- [25] J. Bartels, H. Jung, A. Kyrieleis, *European Physical Journal C* **24** (2002) 555.
- [26] J. Bartels, C. Ewerz, H. Lotter, M. Wuesthof, **386** (1996) 389.
- [27] S. Brodsky, R. Enberg, P. Hoyer, G. Ingelman, hep-ph-0409119.
- [28] J. L. Augneres *et al.*, HERA, A Proposal for a Large Electron-Proton Colliding Beam Facility at DESY, 1981, DESY 81-10.
- [29] I. Abt *et al.*, *Nucl. Instrum. Meth.*, The H1 Detector at HERA, 1997, A386, 310-347.
- [30] I. Abt *et al.*, *Nucl. Instrum. Meth.*, The Tracking, Calorimeter and Muon Detectors of the H1 Experiment at HERA, 1997, A386, 348-396.
- [31] B. Andrieu *et al.* [H1 Calorimeter Group] *Nucl. Instrum. Meth.*, Beam tests and calibration of the H1 liquid argon calorimeter with electrons, **A350** (1994) 57.
- [32] B. Andrieu *et al.* [H1 Calorimeter Group] *Nucl. Instrum. Meth.*, Results from pion calibration runs for the H1 liquid argon calorimeter and comparisons with simulations, **A336** (1993) 499.
- [33] R. D. Appuhn *et al.* [H1 SPACAL Group], *Nucl. Instrum. Meth.*, **A386** (1997) 397.
- [34] R. D. Appuhn *et al.* [H1 SPACAL Group], *Nucl. Instrum. Meth.*, **A374** (1996) 149.
- [35] E. Panaro, Energy measurements in e-p collisions at HERA using the PLUG calorimeter of the H1 Experiment, DESY-THESIS-1998-020.
- [36] H1-Collaboration, Luminosity Measurement in the H1 Experiment at HERA, ICHEP'96, Warsaw, Abstract pal7-026.
- [37] H. Beck, Principles and Operation of the z-Vertex Trigger, H1 internal note, 1996, H1-05/96-479.
- [38] T. Wolff *et al.*, Track Finder for the First Level Trigger of H1, H1 internal note, 1992, H1-02/92-213.
- [39] J. Reidberger, The H1 Trigger with Emphasis on Tracking Triggers, H1 internal note, 1995, H1-01/95-419.
- [40] H. Jung, The RAPGAP Monte Carlo for Deep Inelastic Scattering Version 3.1., 2005, <http://www.desy.de/~jung/rapgap/rapgap31021.ps.gz>.

- [41] B. List, A. Mastroberardino, DIFFVM: A Monte Carlo generator for diffractive processes in e p scattering, Prepared for Workshop on Monte Carlo Generators for HERA Physics, Germany, 27-30 Apr 1998.
- [42] Y. Akimov *et al.*, *Phys. Rev.*, **D14** (1976) 3148.
- [43] K. Goulianos, *Phys. Rep.*, **101-3** (1983) 169.
- [44] U. Bassler, G. Bernardi, Structure Function Measurements and Kinematic Reconstruction at HERA, 1997, DESY-97-137.
- [45] L. Gladilin, Charm hadron production fractions, 1999, hep-ex/9912064.
- [46] S. Eidelman *et al.* (Particle Data Group), *Phys. Lett.*, **B592** (2004) 1.
- [47] G. Flucke, Photoproduction of D* mesons and D* mesons associated with jets at HERA, DESY-THESIS-2005-006.
- [48] F. P. Schilling, Diffractive jet production in deep-inelastic e+ p collisions at HERA, DESY-THESIS-2001-010.
- [49] P. Thompson, Open Charm Production in Inclusive and Diffractive Deep-Inelastic Scattering at HERA, 1999, Univ. Birmingham.
- [50] H1 Collaboration, Diffractive Deep-Inelastic Scattering with a Leading Proton at HERA, 2006, DESY 06-048.
- [51] S. Schmidt, Measurement of charm induced dijet events in deep-inelastic e p scattering with the H1 detector at HERA, (In German), DESY-THESIS-2004-043.
- [52] S. Hengstmann, A Measurement of the Diffractive Charm Production at HERA, DESY-THESIS-2000-215.
- [53] H1 Collaboration, ELAN Working Group, internal communication, 2000.
- [54] P. Thompson, *Nucl. Phys. Proc. Suppl.* **82** (2000) 274.
- [55] M. Hansson, H. Jung, The status of CCFM unintegrated gluon densities, in *DIS 2003, XI International Workshop on Deep Inelastic Scattering, St. Petersburg, Russia* (2003), hep-ph/0309009.
- [56] H. Jung, Un-integrated PDFs in CCFM, in *DIS 2004, XII International Workshop on Deep Inelastic Scattering, Strbske Pleso, Slovakia* (2004), hep-ph/0411287.
- [57] H. Jung, G. Salam, *Eur. Phys. J. C* **19** (2001) 351, hep-ph/0012143.

@ArticleAktas:2006up, author = "Aktas, A. and others", collaboration = "H1", title = "Diffractive open charm production in deep-inelastic scattering and photoproduction at HERA", year = "2006", eprint = "hep-ex/0610076", SLACcitation = "